Magnetic Order in the Pyrochlore Iridates

Author: Steven Michael Thomas Disseler

Boston College

The Graduate School of Arts and Sciences

Department of Physics

MAGNETIC ORDER IN THE PYROCHLORE IRIDATES

by

STEVEN MICHAEL THOMAS DISSELER

Submitted in partial fulfillment of the requirements

for the degree of

Doctor of Philosophy

May 2013

For My Family

Acknowledgements

Simply put, this work could not have come into existence without the incredible support and hard work of countless others around the world. I first thank my advisor Michael Graf for providing me the opportunity to pursue this work, and especially thank him for his encouragement and patience throughout my career in his lab at Boston College. I next thank Stephen Wilson and those in his group for the provision of many excellent samples, without which none of these measurements could have been made. Many thanks are also owed to those at the μSR facilities who helped to make many of these experiments possible including, Sean Giblin, Alex Amato, and Chris Baines. I would not have made it to this time if it weren't for the comradery of the many friends and colleagues in the department over the years including Kevin Lukas, Ryan Johnson, Tim Kirkpatrick, Tom Hogan to name just a few. I must also thank my parents, Tom and Shirley Disseler, for instilling in me from an early age a sense of curiosity and wonder about the world, and for nurturing my gifts and talents to explore it through all things math and science. Lastly, I thank my wonderful fiancée Alison for all of the love and support she has afforded me during this time, and for continuously inspiring me to be the best physicist, partner, and person possible.

Table of Contents

Abstract: Magnetic Order in the Pyrochlore Iridates

This thesis is concerned with experimentally determining the magnetic and electronic states in a unique class of transition metal oxides known as the pyrochlore iridates, $A_2Ir_2O_7$ (A = Y or Rare earth). The extended nature of the *5d* Ir orbitals in the iridates places these materials in a regime of intermediate electron correlation and large spin-orbit interaction such that this system may host several novel or topological states of matter which may be perturbed by incorporating different A-species. Additionally, the pyrochlore structure is geometrically frustrated and has been long been studied as a potential host of a number of exotic magnetic phenomenon. However, even after years of intense theoretical and experimental interest many fundamental questions still remain about the nature of the magnetic ground sates in this series which are of vital importance in understanding the roles of various interactions and potential of such novel phenomenon. The primary aim of this thesis is therefore to determine how magnetic order develops on the Ir sublattice in this series, particularly how it is perturbed through variation of the crystalline structure, magnetism of the A-site ions, and presence of mobile charges.

This thesis is the first comprehensive experimental study of these effects which has utilized several complementary experimental probes of both bulk and local magnetism in a number of compounds. The techniques presented in this work include magnetotransport, bulk magnetization, elastic neutron scattering, and muon spin relaxation (μSR) measurements. All of the three compounds studied in this work (A = Y,

Yb, and Nd) are shown to definitively exhibit long-range magnetic order on the Ir sublattice, which has previously only been inferred based on studies of other compounds. The compounds $Y_2Ir_2O_7$ and $Yb_2Ir_2O_7$ are correlated insulators at low temperature and are found to have identical configuration of the Ir moments, despite the presence of the large localized Yb^{3+}. Numerical investigations presented here have provided the first conclusive evidence that this order is of the 'all-in/all-out' type, consistent with recent resonant x-ray studies; additionally, we have shown that this order exists for all insulating compounds regardless of structural parameters or properties of the *A*-ion.

On the other hand, $Nd_2Ir_2O_7$ is weakly metallic with Kondo-like behavior at low temperature, with long-range order only on the Ir site, in disagreement with previous results from neutron scattering. Measurements of the field dependent magnetization and Hall effect reveal a large anomalous Hall component, suggesting that the Nd^{3+} may exhibit a spin-ice state with very short correlation length, while the Ir sublattice is likely in the 'all-in/all-out' state. From this, it is determined that $Nd_2Ir_2O_7$ lies at an important cross-over point in the series in which correlation energy and conduction bandwidth yield chiral order with features akin to both the metallic unordered $Pr_2Ir_2O_7$ and those of the magnetically ordered insulators. These results are discussed with regard to recent theoretical models exploring the role of electron correlation, frustration and various exchange interactions in these materials.

Chapter 1: Introduction

Why study condensed matter systems? As described famously in an article by P. W. Anderson [1] solid-state systems are not just an application of fundamental laws, indeed the whole of the field consists of simply the elements and the electromagnetic interaction between them. Rather, the phenomena which make this field so interesting stem from the emergent phenomena which only occur as the result of having so many interacting bodies ("more is different"). The primary motivation behind much of modern condensed matter is the search for new phenomena which are the result of considering these basic interactions in new ways and organizing the constituent bodies in a manner capable of realizing them. As an experimentalist, it is the goal to classify these phenomena and distinguish between them via measurements of their constituent order parameters and symmetries.

This thesis will focus on one specific group of materials known as the pyrochlore iridates; this extraordinary group sits at the intersection of many current themes in condensed matter physics, including strongly-correlated electrons, geometric frustration, and topological order as a result of relativistic coupling in the electron band-structure. In particular, we will be examining the evolution of the low energy electronic and magnetic states due to the coexistence and competition between these interactions, in hopes of answering many of the key questions which remain unanswered about this group of materials. Some of the most important questions are: do these materials exhibit magnetically order, and if so what is the configuration? How and why might this change as we go across the series? What is the effect of having two magnetic species, both with

similar frustrated lattices? How does the magnetic order on the rare earth site compare to that found in other pyrochlore compounds? Lastly, can we provide evidence for any novel states of matter, or clues on how these may develop?

To answer these questions, I have taken an approach of utilizing many different but complimentary techniques to probe the magnetic and electronic structures of these materials. The results contained in this thesis represent our attempts to advance our knowledge of this fascinating system, through the conclusive identity of many previously unknown features such as the magnetic structure, as well as the observation of new phenomena which raise many new questions to be explored by future studies.

Outline of this work

The remainder of this work will be broken up into six additional chapters:

Chapter 2: Background and Previous Studies. This chapter presents an overview of important theoretical concepts and introduces the pyrochlore structure. A summary of previous experimental and theoretical studies of the pyrochlore iridates is also presented.

Chapter 3: Experimental Techniques. The goal of this chapter is to provide detailed explanations of the experimental techniques that have been used to study the pyrochlore iridates in this work. This will include details of the material synthesis, an explanation of muon spin relaxation, magnetization and transport measurements, and a brief overview of the cyrostats and other instruments.

Chapter 4: $Y_2Ir_2O_7$ and $Yb_2Ir_2O_7$. This chapter contains results from the studies of two of the compounds measured, $Y_2Ir_2O_7$ and $Yb_2Ir_2O_7$. Simulations of the possible muon stopping sites and also contained in this chapter and are used along with experimental results to discuss possible magnetic ground state configurations in the insulating phases of the pyrochlore iridates.

Chapter 5: $Nd_2Ir_2O_7$. The results of experimental studies of $Nd_2Ir_2O_7$ and lightly Calcium doped $Nd_{2-x}Ca_xIr_2O_7$ are presented in this chapter. The discussion focuses on the apparent cross-over phenomena observered in Nd-227 in which features of both the metallic Pr-227 and insulating A-227 compounds are observed.

Chapter 6: Discussion. This chapter discusses the major conclusions from the preceding chapters, and what they mean in regard to previous theoretical and experimental work on the pyrochlore system as well as other iridates. Special attention on new trends drawn from this work which were previously unknown or misunderstood.

Chapter 7: Conclusions and Future Work. This chapter summarizes the major conclusions from the above chapters, key questions which remain unanswered or which have been raised by this work, and provides my opinion for how future studies of this series of materials should be directed in order to answer these questions.

[1] P. W. Anderson, Science **177** 393 (1972).

Chapter 2: Theoretical Background and Previous Studies

2.1 Interactions in Transition Metal Oxides

Pyrochlore iridates with chemical composition, $A_2Ir_2O_7$ (A = rare earth lanthanide, Y, Bi) are heavier members of the broad class of systems known collectively as transition metal oxides (TMOs). TMOs have a long and fascinating history due to a plethora of interesting phenomena existing in these systems, and include discoveries like colossal magnetoresistance and high temperature superconductivity, to name just two. One common theme in these systems is that by simple count of electrons, they should be metallic; however because of electron-electron interactions they may become insulating or metallic, depending on the details of the crystal and atomic structures. [1]

The pyrochlore oxide materials studied up to this point have the generic composition $R_2T_2O_7$ with R = rare earth lanthanide and T = *3d* or *4d* transition metal, and have by and large been band-gap insulators or semiconductors whose primary interest has been in the magnetic interactions between well-localized rare earth ions (see Ref. [2] for example). Introducing conduction electrons into these systems will inevitably lead to new types of interactions between localized moments; and as will be shown later, the non-coplanar arrangements of the spins on the pyrochlore lattice may produce novel types of magnetotrasport phenomena which could be useful in spin-based electronic devices. It was originally thought that with their extended *5d* orbitals, oxides made from heavy transition metals such as iridium (Ir) and osmium (Os) would become metallic, with

conduction properties that may be determined by the details of the electron-electron interactions. However, the heavier *5d* ions also have substantially larger spin-orbit interactions than their *3d* or *4d* counterparts and thus this interaction plays an increasingly important role in these materials. Because of the complexity of these interactions, both Ir- and Os oxides have been the focus of an increasing number of studies, and may also hold promise for discovering new states of matter and unexpected phenomenon [3], [4] . In the remainder of this section, I will describe in detail these interactions and how they may give rise to novel phenomena in these materials.

2.1.1 Electron-Electron Interactions and the Mott State

In most metallic materials, interactions between electrons can be largely ignored and the vast majority of effects can be calculated using the formalism of Landau's Fermi liquid theory [5], in which the electrons can be described by a non-interacting gas of Fermions but with renormalized dynamical properties such as the mass or magnetic moment. Many transition metal oxides fall in the regime of *strongly correlated systems* meaning that the interactions between electrons lead to a breakdown of the Fermi Liquid picture. This stems from the fact that conduction occurs primarily through *d*-orbitals that are much more spatially compact than the *s*- or *p*- orbitals in simple metals, which results in a significantly larger Coulomb repulsion between electrons. For *3d* ions this interaction is quite large compared to the energy width of the conduction band, meaning perturbation theory is no longer useful, and a new approach must be taken. The first successful

theoretical description of this process was by John Hubbard [6] who proposed a simplified Hamiltonian to describe the "half-filled" problem:

$$H = H_t + H_U \tag{2.1}$$

$$H_t = -W \sum_{\langle ij \rangle} (c_{i\sigma}^{\dagger} c_{j\sigma} + H.C.) \tag{2.2}$$

$$H_U = U \sum_i (n_{i\uparrow} - \tfrac{1}{2})(n_{i\downarrow} - \tfrac{1}{2}) \tag{2.3}$$

In Eq 2.2 $c_{i\sigma}^{\dagger}$ $\left(c_{j\sigma}\right)$ is the creation (annihilation) of an electron with spin σ at sites 'i' (j), representing an electron 'hopping' from sites *j to i* and is simply the tight-biding model for a single band or orbital. The electron-electron interaction is described by Eq. 2.3 where $n_\sigma = c_{i\sigma}^{\dagger} c_{i\sigma}$ is the number operator for the number of electrons with spin up (down) on site i, and U is the size of the Coulomb repulsion; the ½ is the average occupation of the band in this case. Although this model is not exactly solvable, using the mean-field approach one often can gain significant insight into the conduction and magnetic properties of the system, and can be used to determine the location of phase transitions in parameter space.

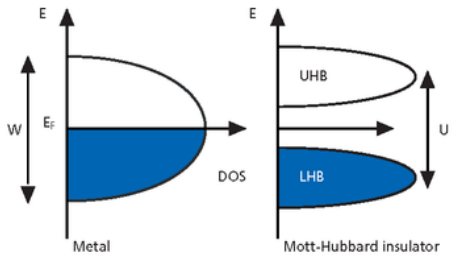

Figure 2.1 Mott transition in a half filled system. We see that a single, half-filled band is split into two due to the Coulomb interaction [7]

The effect of Coulomb repulsion in the single band model is shown schematically if Figure 2.1. In the limiting case of $U = 0$ the system is just the free-electron model, and we find simple metallic band with an effective bandwidth $\sim W$. When $U >> W$ the electrons become localized and the system splits into two subbands with a gap of size ~U. In the case of half-filling, the lower band is completely filled, forming an insulating state, known as a *Mott transition* [8]. Looking at this another way, the system now has a single electron localized to each site such that each site has a magnetic moment; this is why, in light of virtual transitions in second order perturbation theory, this state is often coincident with a magnet transition. In the intermediate regime where U and W are compatible we find a cross-over from metallic to insulating behavior, which may depend sensitively on details of the band structure, filling fraction and other perturbations to the simplified Hubbard Hamiltonian in Eq. 2.2 [6]. In general, this is where the most interesting physical phenomena are found, as these correlations may also have similar energy scales with other interactions such as intra-atomic (Hund's rule) exchange, spin-orbit interaction induced anisotropies, *etc*. such that competition between ground states may occur over many length scales.

2.1.2 Crystal Fields and Transition metals

In any crystalline structure the periodic arrangement of charged ions create electrostatic fields known as crystal electric fields (CEF) and break the rotational invariance of an atom in free space. These fields are calculated at specifc points of interest in the lattice, such as site occupied by the transition or rare earth ion. For a

transition metal or rare earth ion with total spin *J,* the CEF splits the $2J+1$ degenerate levels into a ground state and a series of excited states by the Stark effect; the resultant states may be any linear combinations of the original manifold [9]. In an environment with cubic environment such as the octahedral coordination group, the degeneracy of the *d*-orbitals will be split into two groups: the doubly degenerate e_g, and triply degenerate t_{2g} separated by an energy gap Δ_{cf}. This is formally described by the mathematics of groups and representation theory; however, rather than employing such intensive mathematics here, (which can be found in many excellent texts on the subject e.g. *Ref* [10]) we can form many of the major conclusions by simply examining how charge is distributed in the octahedral environment, shown in Figure 2.2(a). The charge distribution of the e_g states have lobes pointing along the coordinate axis, while the t_{2g} states have lobes pointing along the diagonals (i.e. *[110]* direction). To minimize the Coulomb energy, the electrons will avoid states closest to the negatively charged oxygen anions which are along the coordinate axes, and thus the t_{2g} states should be at a lower energy, shown in Figure 2.2(b). The size of the crystal field splitting Δ_{cf} is determined by the details of the structure, such as cation-anion separation and radial extend of the cation *d*-orbitals. Ir^{4+} has only 5 electrons in its *d*-shell, so for sufficiently large Δ_{cf} only the t_{2g} states will be occupied and we can use only these as the working manifold for further calculations. In real pyrochlore materials the octahedra around each Ir is not perfect as shown in Figure 2.2(a), but is compressed slightly along the *z*-axis. This reduces symmetry of the structure slightly away from the perfect O_h group, and isolated a three-fold or trigonal rotaion C_3 axis indicated in Figure 2.2(a).

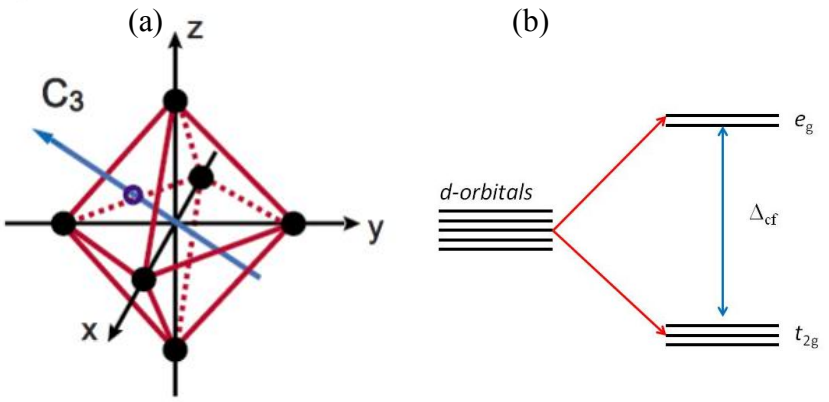

Figure 2.2 (a) Octahedral environment of the Ir^{4+} ion. The Ir^{4+} lies at the center of the octahedron and is surrounded by 6 O^{2-} (black). Trigonal distortions lead to a three-fold rotation about the axis denoted by the blue arrow [12]. (b) Energy splitting of the d-orbitals by the octahedral crystal field.

This type of distortion may have significant impact on the band structure of these materials for several reasons. First, the conduction bandwidth and superexchange mechanisms are largely determined by the Ir-O-Ir bonding angle and Ir-O bond distance [11], and may be sensitive to changes of only a few degrees. Secondly, the t_{2g} states are not eigenstates of the lower C_3 symmetry, and so this distortion may in fact split the t_{2g} manifold or cause mixing between these levels [12]. Furthermore, because of the extended radial size of the *5d* orbitals relative to the *3d or 4d*, these effects are expected to be exacerbated in these *5d* TMO materials.

2.2 Spin-Orbit Interaction in Solids

2.2.1 The spin-orbit interaction

The spin-orbit interaction is a direct result of the effects relativity in an atomic or solid system. Ignoring this effect as is done at the beginning of any introductory quantum mechanics text, we find that the spin of an electron and its orbital motion are decoupled when meaning that both the spin angular momentum (*S)* and orbital angular momentum (*L)* yield good quantum numbers. However, in taking into account the relativistic motion of the electron around the nucleus, we find a spin-orbit term that inevitably entangles these two quantities. The derivation of this term can be found in many introductory quantum mechanics textbooks [13]; therefore I will only quote the result:

$$H_{SO} = -\frac{Ze^2}{m^2c^2r^3} L \cdot S \qquad (2.4)$$

Here, Z is the atomic number, m the mass of the electron, r the orbital radius and c the speed of light. This can be found by either solving the relativistic Dirac Hamiltonian for an electron in an electrostatic field, or by considering the problem semi-classically from the point of view of the electron which observes an orbiting nucleus and a subsequent magnetic field which the couples to the electron magnetic moment. Regardless of the method, both lead to Eq. 2.4.

As this term does not commute with the Coulomb interaction in the Hamiltonian, the projections L_z and S_z are no longer conserved quantities; instead we must use the total angular momentum operator $J = L + S$ which does commute with both the Coulomb interaction and Eq. 2.4, yielding conserved eigenvalues j and j_z. Taking the expectation value of Eq. 2.4 for a simple s-wave state it can be shown that the SOI energy varies as ~

Z^4 (number of protons), and thus increases dramatically with atomic number [13]. In atomic systems the SOI results in the first order perturbative correction of the atomic energy levels known as the atomic fine structure. In crystalline structures the SOI will act to break the spin-degeneracy of the bands formed from these orbitals, in what is known as the Rashba effect [14]. This phenomenon has gained considerable importance in recent years thanks to the discovery of an entirely new quantum state of matter known as topological insulators. Because the search for new topological states has driven much of the theoretical work in the pyrochlore iridates, it is worth-while to introduce the concept of topology in condensed matter systems and how it may relate to transition metal oxides such as the iridates.

2.2.2 SOI and Topology

Topology is the field of mathematics concerned with the qualitative description and classification of different objects. Topological states of matter are those which do not break any fundamental symmetry of the system which normally discriminated different states of matter; however they exhibit some other global quality that prevents the adiabatic deformation from one state to another. The geometrical analogy often used is the difference between a sphere and torus: locally both structures have continuous curvature and will therefore appear quite similar but globally these shapes are quite different as the sphere has no holes passing completely through its surface, while the torus has a single hole. The connection between these global and local properties are described by the Gauss-Bonnet formula [14],

$$\frac{1}{2\pi}\int_S KdA = 2(1-g) \qquad (2.5)$$

where K is the local curvature along the surface S. Integrating this curvature over the entire surface yields an integer genus number g which is actually the number of holes in the surface. We therefore have a well defined way of identifying the difference between such geometric shapes, as there is no continuous way to deform a sphere into a torus (or vice-versa) without introducing a hole.

If instead of a geometric space, we consider the space defined by eigenstates of a Hamiltonian described by two parameters θ and φ i.e. H(θ, φ) and ψ(θ, φ). The curvature of this space is $K = \langle \partial_\theta \psi(\theta,\varphi) | \partial_\varphi \psi(\theta,\varphi) \rangle$ also known as Berry's curvature [15]. Chern showed [16] that the Gauss-Bonnet formula could be extended to include many dimensions and as a result integrating over Berry's curvature will also yield a quantized integer similar to the genus, known as the Chern number. For small (adiabatic) perturbations to the Hamiltonian the Chern number remains constant, like the genus for small deformation of a state. Drastic changes will result in the Chern number increasing by an integer value, as occurs when creating a hole in a sphere to form a torus.

The first such state to be experimentally realized was in the quantum Hall effect (QHE), occurring when a strong magnetic is field applied perpendicular to the surface of two-dimensional semiconductor at low temperatures such that the material is nominally an insulator with no thermally activated carriers. In this state, the Hall conductance changes by integer multiples of e^2/h as either the strength of the magnetic field or carrier density is varied, independent of the details of the material [17]. Laughlin, Hofstadter and others showed that can be described in terms of topology, where each jump in the

conductance can be described by an integer change in the Chern number which occurs when the system fills different Landau levels [18]. Each jump in the conductance can also be through of as the creation of a single state which spans valence and conduction bands but occurs only in magnetic fields.

In materials with strong SOI, the Rahsba effect may be strong enough to induce an inversion between two bands which would normally form the conduction and valence bands of the material. At the boundary with vacuum or a 'normal' insulator these two bands must be smoothly connected meaning that at least one state (now with definite spin because of the SOI) crosses the band gap at the surface. Time reversal symmetry is not broken in these systems, so there will actually be a pair of these states with opposite spin and momentum that will cross to form a node inside the bulk band gap [19]. As such a node must either exist or be absent, there is no way it may be adiabatically removed, *i.e.* it is topologically distinct from a simple band insulator. The effect of this is that the states corresponding to the node form helical conduction channels around their edges or surfaces which have Dirac-like dispersions which are protected from scattering, making them potentially useful in future quantum electronic devices [20]. Experimentally, such states have been observed though measurements of the quantum spin-Hall effect in two-dimensional HgTe/CdTe quantum wells [21] and in momentum space spectroscopies such as STM and ARPES in three-dimensional Bi_2Se_3 and related alloys [19]. To date, most of the topological materials studied thus far are based on elements with *p* and *s* electrons nearest the Fermi level which are generally weakly correlated. However, any heavy atom which has strong SOI may be a candidate to exhibit new topological states. The *5d* series of elements such as Re, Os, and Ir, are particularly interesting because as

transition metals they contain both strong SOI and electron-correlations that are larger than those of *p* and *s* elements and may indeed lead to new ways of creating and studying topologies in condensed matter.

2.2.3 SOI in Transition metals

As stated above, the SOI increases with atomic number as Z^4 such that the heaviest elements have the most pronounced effects. The electron correlation energy, on the other hand, decreases with ascending rows, as the radial expansion of the orbitals allows for the electrons to be further apart while in the same orbital, thereby reducing the Coulomb interaction. The approximate values for the correlation energy and spin-orbit energy as a function of the row number are shown in Table 2.1 below [22]:

Row (Elements)	U	λ
3d (Cu, Co, Fe…)	4-7 eV	0-0.01 eV
4d (Mo, Ru, Rh…)	1-4 eV	.01 -0.1 eV
5d (Os, Re, Ir…)	0.1-2 eV	0.1-1eV

Table 2.1 Comparison of correlation energy (U) and spin orbit coupling (λ) for the transition metal oxides.

Let's now consider the possible effects of these interactions in an *5d* oxide like the iridates, following the arguments put forth by Kim *et al* [23], [27]. Beginning with the manifold of *5d* states of the Ir^{4+}, the octahedral CEF will split these into two groups, the low-lying triplet t_{2g} and higher energy doublet e_g states (plus spin degeneracy); as there

are only 5 electrons in Ir^{4+} and (ideally) the e_g states are empty and well separated, we focus on the t_{2g} states only. If we consider a SOI with energy λ, these degenerate states will split to form the eigenstates of the total angular momentum operator $J = L + S$; now, as eigenvalue of the orbital part is of the angular moment is -l for all of the t_{2g} states, we find two sets of states which are eigenstates of *J:* a low-lying $j = 3/2$ quartet and higher energy $j = 1/2$ doublet, with the quartet being lower in energy by value of λ/2 [3]. Populating these states with the 5 electrons fills the quartet, and leaves a single electron half-filled state with an effective $j = ½$. In one of the first studies on any iridate material, Kim *et al* showed using resonant x-ray absorption that the value of λ was large enough to create such a ground state in Sr_2IrO_4 [23]. The combination of the $j = ½$ effective spin and half-filling greatly simplifies the theoretical assumptions needed to study this system, which is why Ir-systems have been so heavily focused upon as of late.

As mentioned earlier, the iridates were initially expected to be metallic based on the spatial extent of the *5d* orbitals and small correlation energy. However, measurements of many iridate systems including the layered Ruddlesden-Popper series Sr_2IrO_4 and $Sr_3Ir_2O_7$ and as will be shown later, the pyrochlore iridates, have in fact shown many of these systems to be much more strongly insulating than expected [24],[25],[26]. This insulating ground state has been suggested to stem from a Mott-Hubbard correlation driven splitting of the narrow $j = ½$ states which may be split by a much smaller U than if the metallic bands were derived from the full t_{2g} manifold of states [27]. However, because the energy scales these interactions are so close together it is expected that the effects of small distortions of the crystal structure through rotation of the oxygen octahedra, or opening of a gap due to magnetic order known as a Slater transition, can

significantly effect the observed ground state [28] in the iridates. These competing ideas have lead to an active community of theoreticians and experimentalists investigating this complex system; the search for other interesting phenomena in iridate and other *5d* systems is ongoing.

2.3 The Pyrochlore Structure and Geometric Frustration

The previous sections have focused on the various interactions which make all *5d* and iridate system of such great interest. The pyrochlore iridates are unique among these because of the fascinating physics that results from restricting the space of possible magnetic configurations due to the geometrical constraints placed by the crystal structure. This section I will describe the pyrochlore structure, why it has been of interest in the past and how it will play a role in the ground state properties of this iridate series.

2.3.1 The Pyrochlore Strucutre

The pyrochlore oxides have been intensely studied over the past few decades, specifically those with the chemical formula $A_2^{3+}B_2^{4+}O_7^{2-}$ where A is a rare earth or similar trivalent ion and B is a quadravalent transition metal such as Ti, Mo, Sn, or Ir. The pyrochlore actually series actually gets its name from the first mineral discovered with this structure $NaCaNb_2O_6F$ which produced a green flame when burned (in Greek: *pyro* = fire, *chlore* = green) [29]. The pyrochlore oxides exist as a slight variation of this original structure, and are classified with the cubic space group $Fd\bar{3}m$ (No. 227). As there are two distinct oxygen locations, it is common to rewrite the structure as $A_2B_2O_6O'$ when describing the system crystallographically; the conventional description of the

strucutre using Wycoff notation is to assign the *A* site as the *16d*, the *B* to be *16c*, and O to be *48f* and O' as *8b*, as shown in Table 2.2 [30].

Wyckoff Position	Point Symmetry	Coordinate
16d	$\bar{3}$m (D_{3d})	1/2, 1/2, 1/2
16c	$\bar{3}$m (D_{3d})	0, 0, 0
48f	mm (C_{2v})	x, 1/8, 1/8
8b	43m (T_d)	3/8, 3/8, 3/8

Table 2.2: Crystallographic positions of the atoms in the pyrochlore oxides using the convention from International Tables of Crystallography [30] with the origin taken to be the *16c* site.

In the pyrochlore structure, we find octohedral coordination of the O^{2-} around the *B* ion as shown in Figure 2.2(a), while a nearly cubic environment exists about the *A* ion. The distortion of the two polyhedra is controlled by the '*x*' parameter of the *48f* O^{2-} listed in Table 2.2: for $x = 0.3125$ we find a perfect octohedra about the *B* site and for $x = 0.375$ a perfect cube about the *A* site, with most materials existing in the intermediate range of $x = 0.320 - 0.345$.

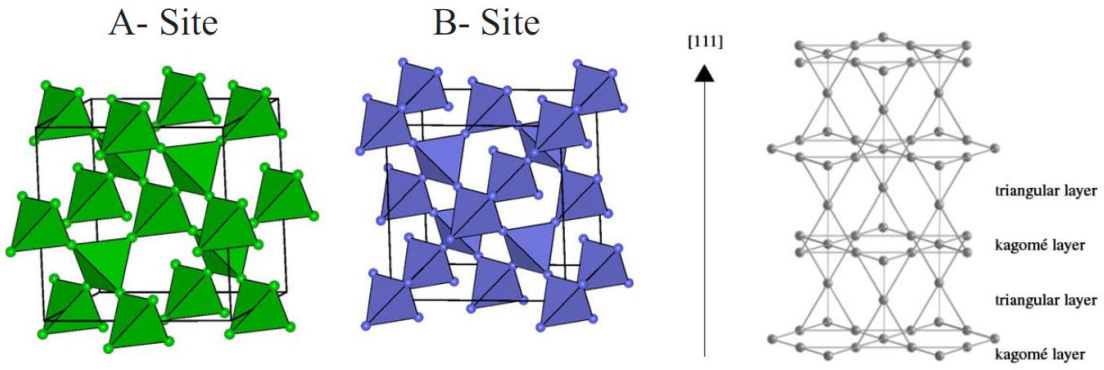

Figure 2.3: (a) The network of corner shared tetrahedra fromed by the *A* and *B* sites. The outline of the unit cell is also shown for comparison of the atomic locations. (b) A view of one of the networks along the [111] direction [2]

Shown in Figure 2.3, both *A* and *B* cations form individual networks of corner-shared tetrahedral units which are offset from one another along the *[111]* direction by half a lattice constant. As it turns out, one of the oxygen anions lies at the center of each the tetrahedra, creating an anisotropic crystal field environment that leads to a strong Ising axis pointing from the center of the tetrahedral through the corners, or along the local *[111]* directions. This is particularly important because in a cubic environment there cannot be a global Ising axis, as this would artificially break the cubic symmetry, therefore the only way to achieve a system with Ising behavior is to define a local set of such directions that are related by transformations allowed by the symmetry. This limitation greatly reduces the phase space of possible magnetic configurations, thus creating a geometry that can support magnetic frustration.

2.3.2 Magnetic Frustration

One of the most interesting features of pyrochlore structure is its propensity to exhibit frustration effects for a wide range of interactions. Generically, a frustrated system can be defined as one, which cannot reach its ideal low energy state by satisfying every pair-wise interaction. This arises because either multiple interactions are present which do not favor the same ground state, or some symmetry constrains the ability of the individual degrees of freedom to explore their entire possible configurational space in order to find the lowest energy state. In magnetic systems, this most often occurs as a result of disorder or geometrical limitations imposed by the crystal structure.

Disorder in magnetic systems may occur as either site-disorder or bond-disorder: the first refers to the random substitution of magnetic moments in a non-magnetic host (or vice-versa), while the latter refers to the random sign and size of bonds occurring between two spins. Interactions in disordered systems cannot be characterized by a single well defined energy which yields characteristic length and time scales of the spin-spin correlations; rather, these correlations are found to be distributed over a wide range which drastically impacts the resultant physical properties. The archetypal examples of this behavior are spin-glass in which below the freezing temperature the majority of spins no longer fluctuate as in the paramagnetic state, but do not have any preferred orientation as occurs when a system enters a ferromagnetic or antiferromagnetic state.

In geometrically frustrated systems, the interaction between spins is of constant sign and magnitude; the simplest case is a three-spin Ising model in which each spin sits on the vertex of a triangle and interacts antiferromagnetically shown in Figure 2.4(b) [31]. Unlike the square plaquette shown in Figure 2.4(a), in which all four spins can all lie anti-parallel to their neighbors, only two of the three spins in the triangle can satisfy such a requirement. When many triangles are placed together to form a corner or edge shared matrix many such spins exist which cannot satisfy their local bonds, yielding a massive degeneracy and finite entropy even at zero temperature. Note that the same system with ferromagnetic interactions is not frustrated and will undergo a transition to a long-range ordered state at some finite temperature. When quantum fluctuations are included, this macroscopic degeneracy can also be thought of as a ‘spin-liquid’ which supports fractionalized excitations which act as mobile neutral particles with a finite spin [32] and may not order even at very low temperatures. Despite decades of theoretical

work, only a few examples of true spin liquids have been found experimentally, with the majority of highly frustrated compounds eventually forming other exotic and pseudo-ordered states due to long range interactions and disorder.

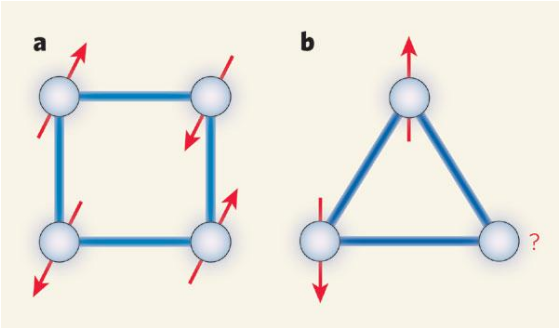

Figure 2.4(a) Four spins on a square lattice coupled antiferromagnetically. (b) Three spins on a triangle coupled similarly: the third spin cannot 'decide' to be up or down. [31]

The corner-shared tetrahedral network in the pyrochlore structure is a three-dimensional analog of the corner-shared triangle scheme so therefore we expect this structure to be frustrated as well. The connection is even more evident when we examine the structure along the *[111]* direction, as shown in Figure 2.3 (b). Here we see clearly planes of corner-shared triangles which are connected by a triangular layer made up of two pyramids stacked point to point. The planes are known as the Kagome lattice which has been a long studied frustrated structure problem and is known to exhibit a rich variety of unusual phase transitions [33].

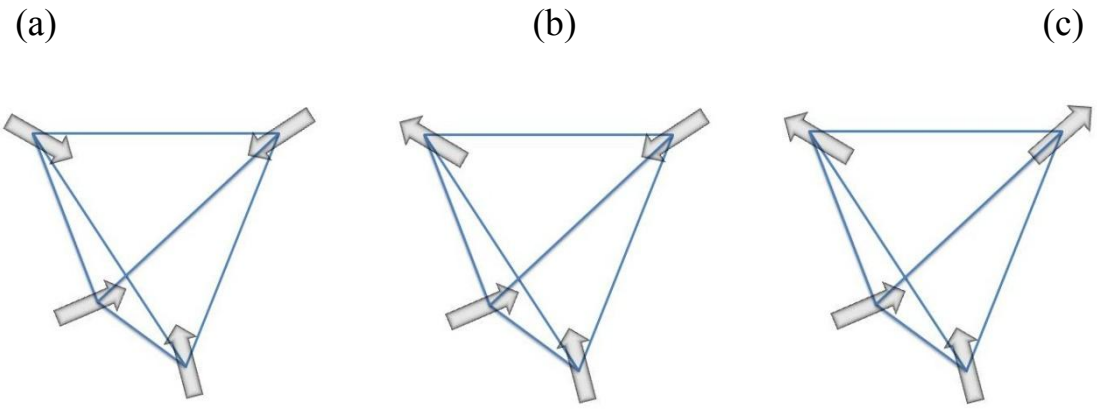

Figure 2.5 Arrangement of spins on a single tetrahedra unit. (a) All-in/All-out (AIAO) (b) Three-in/1-out (3I3O), (c) Two-in/Two-Out (2I2O)

If the ground state of the magnetic ions lying on the corners of the tetrahedra can be described by the perfect Ising state described above, the magnetic moment may only point either directly towards or away from the center of the tetrahedra through the corner. This leads to three distinct local states as shown in Figure 2.5: (a) the "all-in/all-out" (AIAO), (b) "three-in/1-out" (3I1O), and (c) "two-in/two-out" (2I2O) states. In an analogy to simpler coplanar systems, we may think of the AIAO as an equivalent of AFM order as there is no net moment resulting from this system and the configuration may be repeated throughout the system, while the 3I1O may be thought of as a FM state as there will be a net moment along the *[111]* direction order; both can be repeated throughout the lattice forming in a long-range ordered state. On the other hand, there are six ways of forming the 2I2O configuration, therefore locally even if every tetrahedra has a 2I2O configuration, globally the tetrahedra need not have the same spin configuration, meaning

there is no long range order. Neutron scattering experiments on the known 2I2O compounds $Dy_2Ti_2O_7$ and $Ho_2Ti_2O_7$ confirm that the magnetic correlation length is less than the unit cell size [34] indicating the disorder inherent in the structure even though locally order exists. Because of this there is a huge degeneracy in the ground state which allows for many unique physical phenomena.

2.3.3 Spin Ice

The first frustrated system discovered was actually simple water ice. As famously described by Pauling, water molecules obey so-called "ice rules" in which each oxygen is surrounded by four hydrogen atoms forming a tetrahedra; two are much closer to the oxygen as a result of molecular bonding while two are farther due to weaker hydrogen-type bonding [35]. However, there is no reason why any particular two should lie any closer, thus there is considerable residual entropy in this system even at low temperatures stemming from this configurational degeneracy. It was not until 1997 when Harris and others noted that this model could be exactly mapped onto the pyrochlore lattice by replacing the displacement vectors of the hydrogen atoms in water ice with the spin vectors on the magnetic lattice, such that two spins point into the center of each tetrahedra, and two point away (2I2O in Figure 2.5(c)) [36]. The term "spin-ice" was coined to describe a magnetic system which obeys such constraints to emphasize its similarity with water ice. Since it is much easier to perturb and study magnetic interactions than molecular ones in the solid state, the pyrochlore oxides have been used to study the novel behaviors of this type of frustration.

The insulating pyrochlore $Ho_2Ti_2O_7$ was the first material to experimentally exhibit spin ice behavior; Ho^{3+} ion has a large localized moment of ~10 μ_B, while Ti^{4+} is non-magnetic, so only one magnetic network exists in the system. The crystal field energies are such that below ~200 K the system can be described by nearly perfect Ising symmetry [37]. No long-range order has been observed by either neutron scattering or μSR to 50 mK, consistent with the degeneracy expected in the spin-ice. Interestingly, calculations by Bramwell and others [38] revealed that a pyrochlore structure with AFM nearest neighbor interactions should undergo long-range order into the AIAO configuration, while FM interactions should lead to the frustrated 2I2O configuration. This is counterintuitive to the 2D case where FM interactions drive long-range order while AFM interactions drive frustration.

2.3.4 Magnetic monopoles in spin-ice

Since each spin is shared between two tetrahedra, flipping a single spin in a spin-ice state will take the adjoining tetrahedra from 2I2O to a pair of connected 3I1O and 1I3O; this process is depicted in Figure 2.6. The 3I1O has a net magnetic flux into of the tetrahedral unit, while the 1I3O has flux out. We can describe this as a dipole of magnetic charge with each end having charge $2\mu/d$ where μ is the moment size and d is the distance between the centers of the tetrahedra. The ends of this dipole can be separated with no energy cost by flipping a second spin in one of these tetrahedra which will return it to a 2I2O state and its neighbor into a 3I1O (or 1I3O) state. The "sources and sinks" of magnetic flux are thus free to move through the crystal. These excitations act therefore as

a condensed matter analogue of the long-sought after magnetic monopoles [39] and may be an interesting system to explore fundamental symmetries between magnetism and electricity. Experimental evidence for these monopoles was first suggested in μSR measurements of $Dy_2Ti_2O_7$ based on Debye's model for charge particle diffusion [37],[40] however thermal transport and heat capacity measurements appear to confirm their existence in a more concrete manner [41].

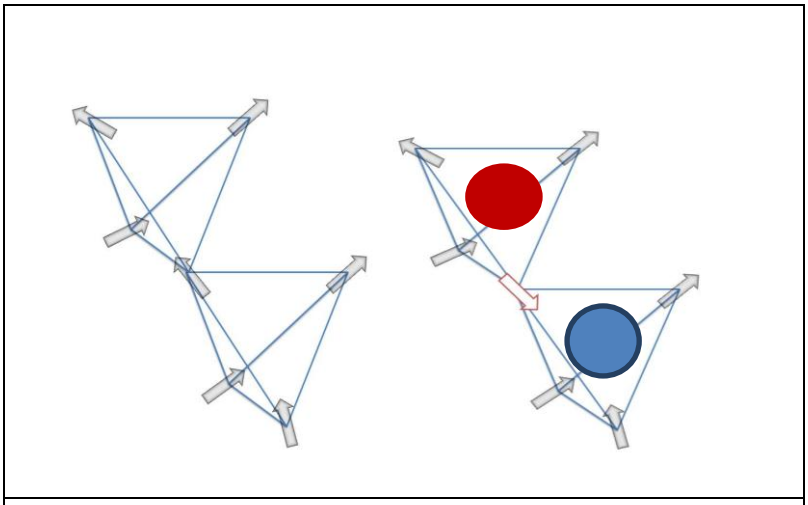

Figure 2.6(a) Neighboring tetrahedra in the spin-ice configuration. (b) The same two tetrahedra after a spin-flip (red arrow) showing the two tetrahedra a sources (red) and sinks (blue) of magnetic flux.

These excitations are exciting as they are a rare example of fractionalization in high-dimensional systems and may be useful as a means of testing the properties of topological computing, for example [42]. Furthermore, such localized sources of magnetic flux will likely have dramatic effects on the electronic conduction properties, and may be a novel way of coupling spin and charge degrees of freedom.

2.4 Previous Studies of Pyrochlore Iridates

The combination of frustration, spin-orbit interaction, and electronic correlations in the pyrochlore iridates put the series at the intersection of many of the most important developments in condensed matter physics over the last half-century. Competition between these interactions in these materials means we can expect an incredibly rich number of interesting or novel states which may be tuned by any one of these effects. This section will give an overview of the experimental and theoretical results which have played a key role in developing current understanding of these materials as well as highlighting the necessity of the work undertaken as a part of this thesis.

2.4.1 Previous Experiments

The first reported synthesis of the any of the iridate pyrochlores was in 1971 by Bouchard [43] who characterized the crystal structure of Gd-227 and Eu-227 as a part of a larger study of the pyrochlore structure. The low temperature transport and magnetic properties of these compounds were not studied until much later however, when Yanagishima and Maeno performed systematic measurements on newly synthesized polycrystalline samples of nearly the entire rare-earth A-227 series [44]. It was shown that the conductivity increases with increasing A-radius where A = Pr is metallic and A = Yb an insulator. Detailed x-ray diffraction measurements of these materials indicate the lattice constant a and oxygen parameter x increase with the radius of the A-site [44], which lead to variation of the Ir-O-Ir bond angle and Ir-O bond length [45]. Early calculations of the electronic structure by Koo *et al* using the local density approximation plus an *ad-hoc* Hubbard term U (*LDA*+U) found that the width of the conduction band

and resultant metal-insulator transition in the pyrochlore ruthenate and iridates are greatly affected by small changes to these parameters [11]. Magnetization measurements taken by Taira [45] revealed that all insulating samples undergo a magnetic transition to an unknown, but presumed antiferromagnetic or spin glass state between 130 - 150 K based on the appearance of a sharp bifurcation between the zero-field cooled and field-cooled magnetic susceptibilities. As this feature appeared to be relatively independent of whether or not the A-site contained a magnetic moment or not, it was presumed that this feature was due to some type or order occurring on the Ir-lattice along. Recent measurements of the resistivity and magnetization by Matsuhira *et al.* [26] on a series of these compounds are shown in Figure 2.7; these were used to construct a phase diagram for the conductive properties as a function of A-site radius and is shown in Figure 2.8. This indicates that the conduction bandwidth is strongly dependent on structural parameters such as the Ir-O-Ir bond angle and distance which are increased as the A-radius increases.

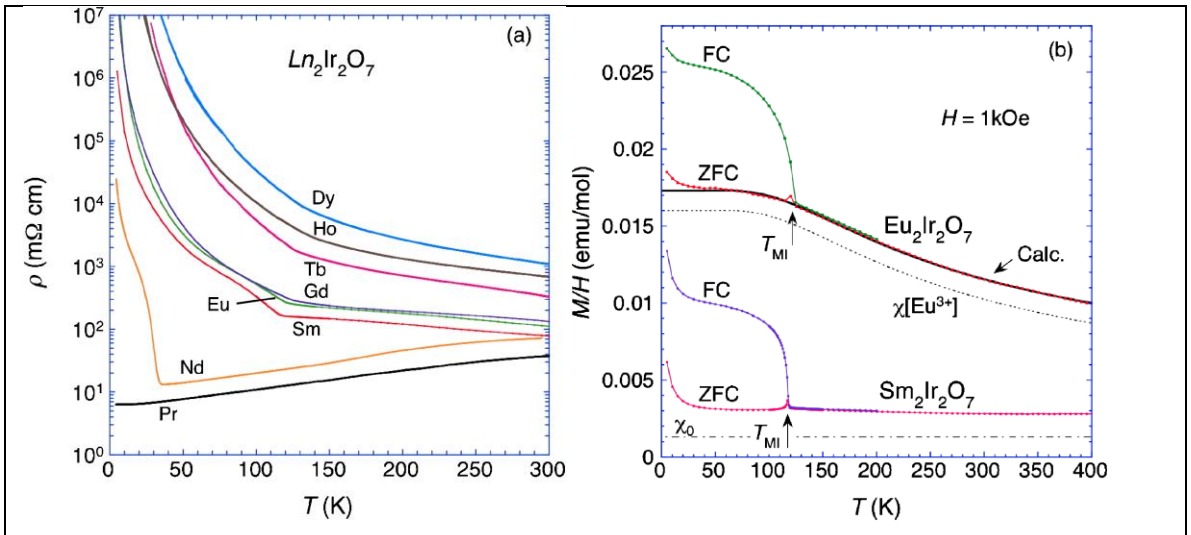

Figure 2.7 (a) the temperature dependent resistivity of several species of $A_2Ir_2O_7$ as measured by Matsuhira et al. in Ref. [26] (b) dc-susceptibility taken from the same work highlighting the magnetic transition at T_M for Eu-227 and Sm-227.

Zero field muon spin relaxation measurements by Zhao, *et. al* on polycrystalline Eu-227 revealed the onset of spontaneous muon precession with a well defined frequency below T_M, indicating long-range order [46]. As Eu^{3+} is non-magnetic, the magnetism in this sample must occur as a result of order on the magnetic Ir^{4+} sublattice. The only other study utilizing muon spin-measurements prior to this work was on Pr-227 in which the compound was found not to undergo any magnetic ordering to below 20 mK [47]. Until the work presented in this thesis, it was unknown if the remainder of the series undergoes a magnetic transition to long-range order at T_M, particularly for compounds whose A-site radius lies between Eu and Pr. The ground state configuration of these systems (*e.g.* AIAO, 3I1O, *etc.*) also remains area of active investigation as it is currently only inferred based on magnetization studies.

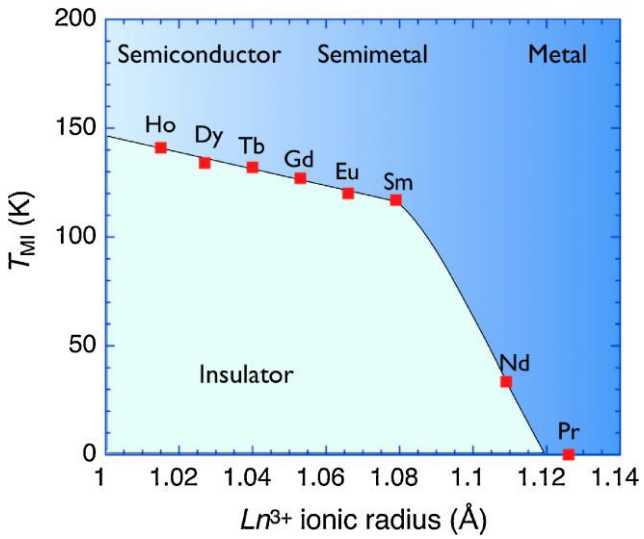

Figure 2.8: Phase diagram of the pyrochlore iridates taken from Ref. [26]

The metallic Pr-227 has gathered exceptional interest in recent years due to the discovery of a finite Hall conductance in the absence of either an applied magnetic field or long range order [48][49], which suggest the existence of a new type of chiral spin-liquid. Recent work utilizing both numerical [50] and analytical approaches [51] have suggested that the effect stems from the non-coplanar arrangement of the Pr^{3+} spins which create a finite chirality around each face of the tetrahedra; this chirality then couples to the conduction electrons through a variety of mechanisms which leads to this unusual behavior. As Pr-227 has been the only metallic sample measured prior to this work it is unknown how or why this state develops from the remainder of the series which appear to be insulating and magnetically ordered, and how the local spin configuration changes as this transition occurs.

The pyrochlore iridates have been gathering theoretical interest since 2010, when the system was first explored by Pesin and Balents for possible topological states stemming from the large SOI found in Ir. In this work, mean-field theory and a slave-rotor approach were used to determine a theoretical ground-state phase diagram over the space of correlations and SOI energies. They were able to show that the system is potentially capable of supporting a strong TI state, as well as magnetically ordered insulating and metallic states [3]. A year later, Wan *et. al* utilizing density functional calculations in the local spin density approximation together with finite correlations and *SOI* (*LSDA + U + SOI*) corroborated that insulating and metallic states are found for large and small values of *U* respectively [52]. However they also showed that for a new topological phase known as the Weyl semimetal state is possible for intermediate values of *U*. Work by Witczak-Krempa *et al.*, and others using a more minimalist tight-binding

model also indicated the presence of this state lying between metallic and magnetic insulating phases [53]. As an example, the phase diagram calculated by Witczak-Krempa *et al*. is shown in Figure 2.9 in which the various electronic and magnetic states are shown as a function of the correlation energy U and the indirect electron hopping strength, t_σ [53]. In this state, a linear dispersion is found at a finite number of band-touching points in the Brillouin zone which act as a three-dimensional analogue of graphene [52]. These points should in theory be topologically protected from gapping, however due to the symmetry of the system the most apparent effects, such as a large QHE, would be evident only if the cubic symmetry is broken via applied strain, for example [54]. Measurements by STM or ARPES of the unique series of arcs which make up the Fermi surface of this state are thus necessary to establish its existence, although recent optical conductivity measurements claim to have observed signatures of this state [55]. One important aspect of this state is that it may only exist for a select group of magnetically-ordered configurations which satisfy the inversion symmetry of the crystal such as the AIAO type. It is important then to understand how the magnetic ground state evolves in order to predict where this state should be observed.

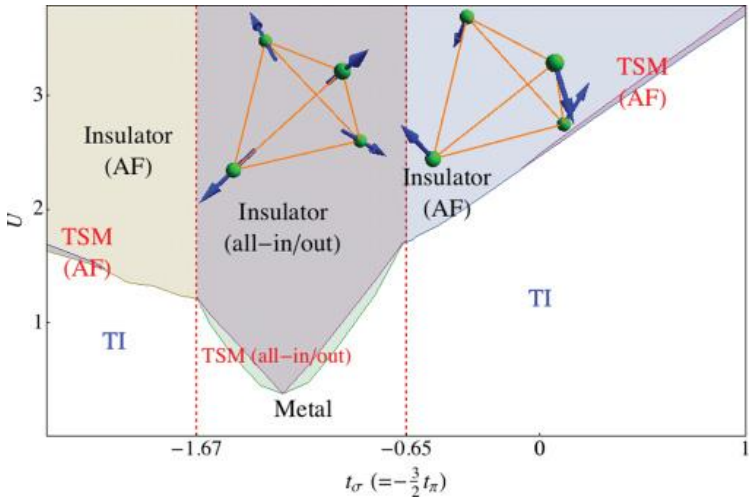

Figure 2.9 Phase diagram for the pyrochlore iridates calculated from the tight-binding model as a function of the correlation energy and indirect hopping strength [54].

Currently, theoretical studies focusing on the properties of these exotic states and the resultant possible phase diagrams vastly outpaces current experimental efforts to determine the actual ground states of these materials. The goal of this thesis is thus three-fold: first is to measure experimentally properties which describe in detail the low-energy states across this series; second, to use these measurements to understand the roles of the various interactions in the system in determining the ground state; and lastly to look for evidence for any of the theoretically predicted exotic states.

Chapter 2 References

[1] P. A. Cox, *Transition Metal Oxides: An Introduction to Their Electronic Structure and Properties*, (Oxford University Press, USA 2010).

[2] J. S. Gardner, M J. P Gingras J. E. Greedan, Rev. Mod. Phys 82, 52 (2010).

[3] D. Pesin and L. Balents, Nature Physics 6, 376 (2010).

[4] W. J. Padilla, D. Mandrus, and D. N. Basov, Phys. Rev. B **66** 035120 (2002). D. Mandrus, J. R. Thompson, R. Gaal, L. Forro, J. C. Bryan, B. C. Chakoumakos, L. M. Woods, B. C. Sales, R. S. Fishman, and V. Keppens, Phys. Rev. B **63**, 195104 (2001).

[5] A. A. Abrikosov and I. M. Khalatnikov, Rep. Prog. Phys. **22** 329 (1959).

[6] J. Hubbard, Proc. Royal Soc. London **276** 239 (1963).

[7] *www.**psi.ch**/*

[8] N. F. Mott, Proc. Phys. Soc A **62** 416 (1949)

[9] K. W. H. Stevens Proc Royal Soc. London A **65** 387 (1952)

[10] J. F. Cornwell, *Group Theory in Physics*. (Academic Press, San Diego 1997)

[11] H. J. Koo, M. H Whango, B. J. Kennedy, J. Solid State Chem. **136** 269 (1998).

[12] B.J. Yang and Y. B. Kim. Phys. Rev. B **82**, 085111 (2012).

[13] R. Shankar. *Principles of Quantum Mechanics, 2nd Ed.* (Plenum Press, New York 1994). E. Merzbacher *Quantum Mechanics* (John Wiley, New York 1998).

[14] R. Winkler, *Spin-Orbit Coupling Effects in Two-Dimensional Electron and Hole Systems*. (Springer-Verlag Berlin 2003).

[15] A. A. Kosinksi, *Differential Manifolds* (Dover Pub. New York 1993).

[16] S. Chern, Annals of Mathematics **46**, 674 (1945).

[17] K. von Klitzing, G. Dorda, M. Pepper, Phys Rev. Lett **45** 494 (1980)

[18] R. Laughlin, Phys. Rev. B **23** 5632 (1981)

[19] M. Z. Hasan and C. L. Kane, Rev. Mod. Phys. **82** 3045 (2010)

[20] X.-L. Qi, S.-C. Zhang, Rev. Mod. Phys **83** 1057 (2011)

[21] M. Konig, S. Wiedmann, C. Brune, A. Roth, H. Buhmann, L. Molenkamp, X.-L. Qi, S.-C. Zhang Science **318** (2007)

[22] P. Fazekas, *Lecture Notes on Electron Correlations and Magnetism*, (World Scientific Pub Co Inc, New York 1999)

[23] B. J. Kim1, H. Ohsumi, T. Komesu, S. Sakai, T. Morita, H. Takagi, T. Arima, Science **323** 1329 (2009).

[24] Chetan Dhital, Tom Hogan, Z. Yamani, Clarina de la Cruz, Xiang Chen, Sovit Khadka, Zhensong Ren, and Stephen D. Wilson, Phys. Rev. B **87**, 144405 (2013).

[25] Chetan Dhital, Sovit Khadka, Z. Yamani, Clarina de la Cruz, T. C. Hogan, S. M. Disseler, Mani Pokharel, K. C. Lukas, Wei Tian, C. P. Opeil, Ziqiang Wang, and Stephen D. Wilson. Phys. Rev. B **86**, 100401 (2012).

[26] K. Matsuhira, M. Wakeshima, Y. Hinatsu, and S. Takagi, J. Phys. Soc. Jpn. **80** 094701 (2011).

[27] B. J. Kim, Hosub Jin, S. J. Moo2, J.-Y. Kim, B.-G. Park, C. S. Leem, Jaejun Yu, T. W. Noh, C. Kim, S.-J. Oh1, J.-H. ParkV. Durairaj, G. Cao, and E. Rotenberg, Phys. Rev. Lett. **101**, 076402 (2008).

[28] W. Witczak-Krempa, A. Go, and Y. B. Kim, Phys. Rev. B **87**, 155101 (2013).

[29] H. R. Gaertner Neues Jahrb. Mineral., Monatsh., **61**, 30 (1930)

[30] *International Tables for Crystallography, Volume A* (2005).

[31] M. Harris, *Nature* **456** 886 (2008).

[32] L. Balents, Nature **464** 7286 (2010).

[33] Sachdev, S. Kagome, Phys. Rev. B **45**, 12377 (1992)

[34] S.T. Bramwell, M. J. Harris. Science **294** 1495 (2001)

[35] W. Pauling, J. Am Chem Soc (1935).

[36] Harris, M.J. et al. Phys. Rev. Lett, **79** 2554 (1997).

[37] S. Bramwell, M. Harris, Phys. Rev. Lett. **87** 047205 (2001).

[38] S. T. Bramwell, M. J. Harris, J. Phys. Condens. Matter **10**, L215 (1998)

[39] C. Castelnovo, R. Moessner, S. L. Sondhi, *Nature* **451** 42 (2008)

[40] S. T. Bramwell, S. R. Giblin, S. Calder, R. Aldus, D. Prabhakaran and T. Fennell, Nature **461**, 956 (2009)

[41] G. Kolland, O. Breunig, M. Valldor, M. Hiertz, J. Frielingsdorf, and T. Lorenz. Phys. Rev. B **86**, 060402 (2012).

[42] A. Kitaev, Annals of Physics, **303** 1 (2003).

[43] R. J. Bouchard and J. L. Gillson, Mat. Research Bulletin **6** 669 (1971).

[44] D. Yanagishima and Y. Maeno, J. Phys. Soc. Jpn. 70, 2880 (2001).

[45] N. Taira, M. Wakeshima, and Y. Hinatsu, J. Phys.: Condens. Matter 13, 5527 (2001).

[46] S. Zhao, J. M. Mackie, D. E. MacLaughlin, O. O. Bernal, J. J. Ishikawa, Y. Ohta, and S. Nakatsuji, Phys. Rev. B 83, 180402(R) (2011).

[47] D. E. MacLaughlin, Y. Ohta, Y. Machida, S. Nakatsuji, G. M. Luke, K. Ishida, R. H. Heffner, Lei Shu, and O. O. Bernal, Physica B 404, 667 (2008).

[48] Y. Machida, S. Nakatsuji, S. Onoda, T. Tayama, T. Sakakibara, Nature **463** 210 (2010).

[49] L. Balicas, S. Nakatsuji, Y. Machida, and S. Onoda, Phys. Rev. Lett. 106, 217204 (2011).

[50] R. Flint and T. Senthil, Phys. Rev. B **87**, 125147 (2013).

[51] M. Udagawa, R. Moessner, arXiv:1212.0293 (2012)

[52] X. Wan, A. M. Turner, A. Vishwanath, and S. Y. Savrasov, Phys. Rev. B 83, 205101 (2011).

[53] W. Krempa and Y. B. Kim, Phys. Rev. B 85 045124 (2012).

[54] Kai-Yu Yang, Yuan-Ming Lu, and Ying Ran, Phys. Rev. B **84**, 075129 (2011).

[55] K. Ueda, J. Fujioka, Y. Takahashi, T. Suzuki, S. Ishiwata, Y. Taguchi, Y. Tokura, Phys. Rev. Letters **109** 136402 (2012).

Chapter 3: Experimental Techniques

3.1 Introduction

Now that the system and motivation have been introduced, I turn to the materials and experiments which will make up the remainder of this work. Because this thesis represents this first comprehensive study electrical transport, bulk and local magnetism of these materials, many different experimental techniques must be introduced in this chapter. As such, this chapter will be broken up into several sections to focus on the specific techniques. In the first section I will give an overview of the sample fabrication process, and briefly discuss the characterization procedures used to ensure the quality of the materials. In the second section I will introduce the idea of bulk magnetization and how it is measured. The third section will discuss the muon spin relaxation (μSR) technique and describe how it is used to study local magnetism in various materials. In the final section I will briefly describe electrical transport measurements and the cryogenic systems used to perform these measurements.

3.2 Materials Synthesis

3.2.1 Solid State Synthesis

As introduced in Chapter 2, the pyrochlore iridates are oxides, which by nature are ceramic materials like the cuprates, titanates, *etc*. Because of the high melting points of most oxide starting materials, they cannot be simply melted or deposited like intermetallic compounds. Rather, these compounds must be formed by reacting starting

materials together at high temperatures for many days on end in a process known more generically as sintering [1]. Sintering is well known process that has been used in traditional ceramics manufacturing for centuries, and involves the diffusion of elements between surfaces of various grains or powders at high temperatures and pressures. In the case of single phase material like alumina, this diffusion will cause grains to fuse together and reduce the empty volume between them, in a process known as densification. This has been used for many years as an effective way to improve the properties of many ceramic materials. If instead the two surfaces are different materials (such as oxides of different species) chemical reactions between diffusing elements may create a new phase which will begin to nucleate and grow at this interface. Therefore, to have sufficient growth we want to 1) maximize the surface area by reducing the diameter the starting particles and 2) react at high temperatures to increase the overall diffusion rate and enhance reactions [2].

For the pyrochlore iridates the starting materials are high purity iridium oxide IrO_2 (Alpha Aesar, 99.99% purity) and rare earth oxides R_2O_3 (Alpha Aesar 99.99% purity) which are mixed in approximate molar ratio of 2:1 to yield the required ratio of Ir:R of 1:1. These starting powders are first dried to remove any residual atmospheric moisture, then thoroughly ground and mixed together. To increase the contact between powder grains and improve diffusion, the powder mixture is placed in a hydraulic pressure vessel and pressurized to greater than 300 MPa to form a solid pellet [3],[4].

The mixture is then sealed in a quartz or platinum tube, or simply placed in an alumina crucible, and baked in specialty high temperature furnaces for a period of days. The temperature cycles are found through a process of trial and error, but typically reach

maximum temperatures on the order of ~1100-1200 C. After 1-2 days the samples are removed, reground, and checked for phase purity with x-ray diffraction. If unreacted starting material or other impurity phases are detected, the ground powder is then repressed, and placed back in the oven for another 1-2 days; this process is then repeated until the sample becomes single phase within the limit of the x-ray diffraction (a few percent) or energy dispersive x-ray spectroscopy (EDXS or EDS), also a few percent.

3.2.2 Characterization

After many days of reaction, detailed x-ray diffraction measurements are performed on a sample of the final powder. Reitvald refinement is then performed on the resulting spectra using FullProf [5] or similar software and the lattice constant and other structural parameters are extracted. As discussed in Chapter 2, the structure is analyzed using the Fd3m space group which has only two free parameters, the overall lattice constant and the '*x*' displacement parameter of the 48f oxygen sites; these parameters can be found in Table 3.1 taken from Ref. [3][4] for the compounds of interest in this work. After phase purity has been assured at this level, EDS is used to verify the elemental ratio of the rare earth and Ir components. Oxygen is generally too light to be observed by this technique, moreover as EDS is a surface measurement adsorption of either water vapor or other resides on the surfaces greatly obscures these values. This technique generally gives an error in the final concentration of roughly 2 % for heavier elements that can be resolved with this technique.

Compound	*a* (Å)	x/a
$Yb_2Ir_2O_7$	10.1015(5)	0.3505
$Y_2Ir_2O_7$	10.1699(4)	0.3527
$Nd_2Ir_2O_7$	10.3647(9)	0.3525

Table 2.1: Lattice parameters and oxygen displacement parameter for the three compounds which will be the focus of the remainder of this work.

3.3 Magnetization

When we speak of magnetization, we are referring to simply the average magnetic dipole moment per unit volume of a material which results from the action of either an externally applied magnetic field or the unbalanced spin or orbital angular momentum of the electrons and nuclei. While Maxwell's equations are perfectly suited to study the macroscopic properties of magnetic materials, they cannot predict or explain the origin of such phenomena on the microscopic scale; this requires a full use of quantum mechanics in the solid-state [6]. As a result, the measurement of the magnetic properties of a material is often of fundamental importance in understanding the microscopic interactions of a system. The remainder of this section will briefly discuss the relevant information we can gain, as well as how the measurements of magnetization are performed.

3.3.1 Magnetism in Condensed Matter

Macroscopically, the magnetization per unit volume is defined by the relationship $\boldsymbol{B} = \mu_0\boldsymbol{H} + \boldsymbol{M}$ where $\boldsymbol{B}$ is the magnetic inductance, $\boldsymbol{H}$ is the magnetic field and the magnetization $\boldsymbol{M}$ may be a function of the magnetic field, or $\boldsymbol{M} = \boldsymbol{M(H)}$. Because this is related to the microscopic arrangements of the magnetic moments in the material, the magnetization is also related to the free energy $F(\boldsymbol{M},\boldsymbol{H})$ [7] of the system given by Eq. 3.1:

$$\boldsymbol{M} = -\frac{1}{V}\frac{\partial F}{\partial \boldsymbol{H}} \qquad (3.1)$$

In a paramagnetic or diamagnetic material the system does not have a net magnetization unless an external field is applied as the free energy of the system is minimized through thermal fluctuations of the local moments which will reduce the average magnetization zero. Applying an external field to the paramagnet results in an enhancement of the magnetic field meaning that the susceptibility defined as $\chi = \frac{\partial M}{\partial H}$ is positive while diamagnet acts to reduce the applied field or $\chi < 0$. At small fields or high temperatures ($\mu H << k_B T$), χ is given by the Curie-Weiss law for a set of ions with total spin J, shown in Eq. 3.2. This can be derived from an expansion of the free energy for a canonical ensemble of interacting spins. Here, N and V are the number of moments and volume of the system respectively, g is the average gyromagnetic ratio, J is the total angular momentum, and θ_{CW} is the Curie-Weiss temperature.

$$\chi = \frac{N}{V}\frac{(g\mu_B)^2}{3}\frac{J(J+1)}{k_B(T-\theta_{CW})} \qquad (3.2)$$

The parameter g provides information about the size and anisotropies of the local moment which, in ideal cases, can be used to extract information about the various crystal

field energy levels determined by the interaction with the local environment. The Curie-Weiss temperature on the other hand is a measurement of the average interaction between nearest neighbor magnetic moments which drive the system toward long range order at low temperature. The sign of θ_{CW} gives the type of interaction: $\theta_{CW} > 0$ represents ferromagnetic (FM) interactions and $\theta_{CW} < 0$ anitferromagnetic (AFM); while the magnitude of θ_{CW} gives the approximate strength of the interaction in units of temperature [8].

For systems with interactions between moments, at low enough temperature it may become energetically favorable for the moments to form a periodic arrangement such that the directions of the magnetic moments are correlated with each other over the entire lattice. The ordered state is thus said to have a spontaneously broken rotational or time-reversal symmetry in that we can no longer perform arbitrary rotations on the sample and bring it back to its original state. This is distinguished from the paramagnetic state, which over time will look the same with all rotations as the individual moments fluctuate due to thermal disorder. Each such symmetry has associated with it an *order parameter* which takes a non-zero value below some critical temperature, and distinguished it from other possible states [7]. For example, FM systems the order parameter is the spontaneous magnetization of the sample which results from the alignment of the local moments in the absence of any applied field, while for AFM systems a more apt order parameter is the magnetization of the individual sublattices as the net moment in the ideal case is zero. Systems which are antiferromagnets often have a small FM moment due to canting of the moments away from perfect alignment or surfaces which may have a non-trivial magnetic structure.

In FM systems at finite temperature it will often be more energetically favorable to form domains in the macroscopic sample which are regions of the same type of magnetic order, but may be oriented in different directions with respect to one another. Regions with different directions are separate by domain walls which move in response to the applied field such that there will be a balance between the energy of the bulk of the domain in the applied field and that required to create or move the domain surface. We can study the formation of these domains by cycling the magnetic field over a closed loop, known as an isothermal hysteresis loop. There are two important parameters are extracted from this analysis, the remnant moment, and the coercive field. The remnant moment is the residual dipole moment of the sample after sweeping the applied field from zero up to the point at which the magnetic moment saturates, and then back to zero field again; a larger remnant moment means that the domains have a larger polarization and are more resistant to thermal fluctuations, thus have a larger energy cost associated with them. The coercive field is the field required to return the magnetization to zero after saturation. Together, the area inside the hysteresis loop represents the work performed in reversing the magnetization which is dissipated through the motion of the domain walls, for example [8].

Ideally, we want to measure magnetic materials so that we can understand how such phase transitions occur as a result microscopic interactions. We also want to study the fluctuations about the ordered state due to thermal or quantum excitements as these also reveal a great deal of information about the underlying ground state. Many different types of experiments have been developed over the years to measure various properties of magnetic samples, and can be broken up into two broad catagories: bulk probes and local

probes. Bulk probes include techniques like SQUID or cantilever magnetometry which measures the average magnetization or susceptibility of an entire sample, and neutron scattering which measures the wave-vector specific magnetization and allows for determination of the magnetic structure in antiferromagnets. Local probes include techniques such as muon spin relaxation, nuclear magnetic resonance, and Mossbauer spectroscopy, all of which probe the interactions of the magnetic ions with a collection of magnetic nuclei or particles which sit at specific points within the lattice. As these probe different properties, both bulk and local probes are necessary to fully understand the evolution of the magnetic state in complex systems.

3.3.2 SQUID Magnetometry

As described above, a great deal of information about the magnetic state can be gained from measurements of the bulk magnetization and susceptibility as a function of temperature and magnetic field. There are numerous ways to perform these measurements which have been developed over many years, however the most commonly used procedure today involves applying a small magnetic field to a sample, such that there will be a net moment even if the sample is paramagnetic or diamagnetic, and any additional spontaneous moment will be easily observed. The net dipole moment induced in the sample will then be measured by one of the many types of magnetometers available today. Most magnetization measurements in the range of 2 K to 400 K, including the measurements presented in this work, are made with so-called SQUID (Superconducting Quantum Interference Device) magnetometers. The SQUID

magnetometer is built around a Josephson junction, and utilizes the fact that magnetic flux passing through a superconductor must be quantized in units of *h/2e* or 2.067 x 10^{-15} Wb; each unit of flux passing through induces a tunneling current between parts of the junction which are detectable by sensitive electronics. By carefully design of the electronics, very small amounts of magnetic flux can lead to large changes in the detected current, thus the device can detect minute changes in magnetic fields passing through the magnetometer [9].

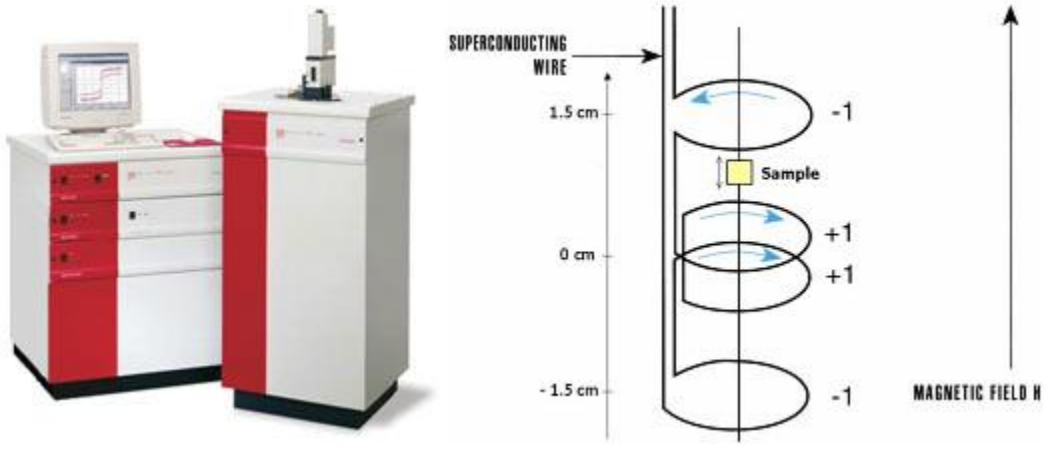

Fig 3.1 (a) Quantum Design's MPMPS system, (b) Schematic of the pick-up coil loop system. Images courtesy of Quantum Design [10].

Since the 1970's this technology has become widely commercialized, and is found in many systems such that the user may simply "insert and go" and collect accurate and reliable measurements. One of the most popular systems, and the one used in this work, is the Quantum Design Magnetic Property Measurement System (MPMS) shown in Figure 3.1(a) [10]. Inside the system is a superconducting magnet capable of

generating fields up to 9 T and all of the accompanying electronics for the SQUID device. Shown in the schematic in Figure 3.1(b), the sample is attached to a non-magnetic rod via a plastic straw and passed through sets of superconducting coils at a frequency of a few Hz. Thanks to either the applied field or spontaneous magnetization, the net dipole moment of the sample induces emf in the coils which is measured by the SQUID electronics (not shown). This information may then be used to determine the size of the moment using simple fitting routines to the theoretical curve for a moment passing through a coil. In this way, the MPMS can be used to measure static (or DC) magnetic properties. I note here that although the magnetic susceptibility is defined strictly as $\chi = \frac{\partial M}{\partial H}$ which may have time or frequency dependence, it is often reported in literature as static magnetization normalized to the field, or $\chi = \frac{M}{H}$; for simple paramagnets and diamagnets this definition is exact, however in the ordered state this serves simply as a normalization process. The frequency dependent response (or AC) of the magnetization may also be measured in this way by applying a small driving field with a fixed frequency to the sample and using lock-in techniques to study relaxation mechanisms. In this thesis, the MPMS or the Oxford Maglab DC extraction magnetometer, which relies on the same principle but lacks the sensitive SQUID technology, are used measure the of the DC susceptibility $\chi = M/H$ as a function of temperature, and the magnetization as a function of the applied field, *M(H)*. As a side note, I constructed a dedicated device utilizing the AC technique in an earlier project to study the dynamics of the Shastry-Sutherland material Yb_4LiGe_4 to 300 mK. These results along with others from this project can be found Appendix A1.

3.3.2 Procedural Details

In order to explore the effect of external magnetic field on the magnetic ground state, samples are cooled to base temperature (2 K in the case of the MPMS) in two conditions: with no applied field (zero field cooled or ZFC) and in a finite field (field cooled or FC). In all measurements to be presented, samples are first ZFC, then a modest field on the order of 1 kOe, is applied and the sample slowly warmed to 300 K either at constant rate or in small incremental steps. The sample is then FC and the measured during warming again to ensure an equal comparison to ZFC in the case that there is significant thermal hysteresis about a transition.

After saturation, it is important to note that the magnetization and field never comes back to the origin unless warmed above the Curie temperature and cooled in zero field again. Therefore, to compare the low field behavior at different temperatures samples must be cooled in a virgin state after each isothermal hysteresis loop. The data in this work have been measured in such fashion; after each loop the sample is warmed above the transition temperature determined from the temperature dependent susceptibility measurement, and then cooled in zero field to the next temperature. This procedure requires significant extra time however results in data which contains no ambiguities regarding the low field behavior.

3.4 Muon Spin Measurements

In the previous section, I have discussed the primary technique which is used to measure the macroscopic or bulk magnetism in this work. As will become evident, this alone cannot provide all of the necessary information about the magnetic state, particularly in complex materials such the pyrochlore iridates. In order to gain more information about onset of magnetism and the evolution of the dynamic properties of these systems we wish to be able to probe these systems at local level, rather than the spatial average obtained from bulk probes. This section will introduce one powerful set of techniques known as muon spin rotation/relaxation/resonance (μSR) that make up a large portion of this thesis. This section will provide a detailed background of μSR and why it is a useful tool to study magnetism in complex materials, as well as details regarding how experiments are performed the way which useful information is extracted from these measurements.

3.4.1 Why μSR?

Muon spin rotation/relaxation/resonance (μSR) was first realized in the 1950's when fundamental experiments studying the asymmetry of the muon decay noted the that the preferential emission of positrons from positive muon decay along the spin orientation could be used as a local probe of interstitial regions in solid materials. The first μSR measurements were carried out only weeks later [11]. Since this time the technique has become widely used by those in the chemistry and physics communities in a variety of research areas. The muon is a second generation lepton with physical

properties that are intermediate that of the proton and electron, as shown in Table 3.2. From this we can see why the technique has become so popular: with a weight of ~1/9 that of a proton and equal charge, the muon can be used by chemists as an additional means of studying hydrogen diffusion and bonding in polymers, semiconductors, and refractory metals used in industry. Conversely, with its spin of ½ and mass of ~200 m_e the muon has a much smaller (larger) gyromagnetic ratio than the electron (proton) and can be used to study local magnetic fields similar to nuclear magnetic resonance (NMR) but without the need for large magnetic fields, or for microwave cavities used in electron spin resonance (ESR) [13]. The remainder of this section will now focus on the production of muons and how they are utilized in our condensed matter experiments.

Property	e	μ	p	n
Mass	m_e	207 m_e	1870 me	1870 me
$\gamma/2\pi$ (MHz/T)	28.04 x 10^3	135.5	42.57	29.14
Lifetime	∞	2.2 μs	∞	885 s

TABLE 3.2: Physical constants of important fundamental particles, taken from Ref [12].

3.4.2 Muon Production

Muons are leptons, which together with electrons, taus and their corresponding neutrinos make up half of the known particles of the standard model. Their free lifetime of ~2.2 μs makes them the most stable particles in the model after electrons and the light baryons (protons and neutrons). Intense beams of muons are routinely produced as

several facilities over the world [14], each involving a two-step process to final muon production.

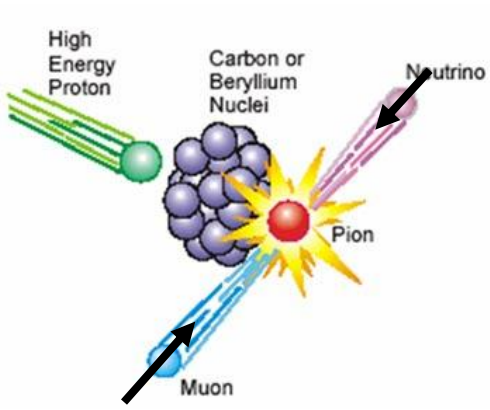

Figure 3.2: Cartoon overview of the muon production process via pion decay as described in text. Image courtesy of ISIS website.

In the first step a beam of protons with energy greater than 500 MeV is passed through a graphite or beryllium sheet of thickness ~1 cm. The interactions of the high energy protons with the light nuclei lead to the following possible reactions, each resulting in the creation of a pion:

$$p + p \rightarrow \pi^+ + p + n \qquad (3.3a)$$

$$p + n \rightarrow \pi^+ + n + n \qquad (3.3b)$$

$$p + n \rightarrow \pi^- + p + p \qquad (3.3c)$$

The pion is an unstable particle that decays with a lifetime of ~26 ns via the weak interaction into a muon and a corresponding neutrino shown in Eq. 3.4, making up the second step of the muon production. This process is depicted in the cartoon shown in Figure 3.2.

$$\pi^{\pm} \rightarrow \mu^{\pm} + \nu_{\mu} \qquad (3.4)$$

When the pion undergoes decay is at rest, conservation of linear momentum dictates that the resulting muon and antineutrino must be emitted in opposite directions.

A fundamental property of the neutrino is that it has a fixed chirality such that the spin and momentum vectors must be antiparallel, as indicated by the arrow superimposed on the neutrino in Figure 3.2 Because the pion is a spin 0 particle and we are considering the case at rest, by conservation of angular momentum the emitted muon must also have a definite spin relative to the antineutrino, and therefore the muon is also produced in a chiral state having spin and momentum vectors antiparallel, also indicated by the arrow in the figure [13].

Using appropriate momentum and velocity selectors, the outgoing stream of particles from the target may be filtered into a spin polarized monochromatic beam of muons. The high energy muons (~26 MeV) are then steered by a variety of electromagnets to the sample-detector and implanted into the sample. In condensed matter experiments only positive muons are used; these readily lose energy through collisions with the lattice and will eventually comes to rest at an interstitial site within the host lattice, generally at the site of lowest electronegativity. Critically, because the interactions with the lattice are essentially electrostatic the polarization of the thermalized muon is unaffected during this process. Depending on the sample density, the stopping lengths at which the muon comes to rest are typical are of the order 100-300 μm for solid-state systems, therefore the probe is not sensitive to surfaces and does not require specialized ultrahigh vacuum environments; the only requirement is that cryostats must be outfitted with specialized windows made of thin foils to minimize scattering and absorption of the oncoming beam [14].

3.4.3 Muon Decay

The muon decays with a mean lifetime of 2.1962 μs through the weak interaction into a positron and a pair of neutrinos, shown in Eq. 3.5.

$$\mu^+ \rightarrow e^+ + \nu_\mu + \nu_e \qquad (3.5)$$

Neutrinos are charge-less and (nearly) mass-less particles which make them very difficult to detect; therefore all μSR systems detect only the resultant positron emission. Because of parity violation in this decay, the angle at which the positron is emitted is correlated to the direction of the muon spin ***S*** (shown as the yellow vector in Figure 3.3) at the time of decay; in fact it can be shown that the probability of the positron emission at angle θ relative to ***S*** is:

$$W \sim [1+\alpha(\varepsilon)\cos(\theta)] \qquad (3.6)$$

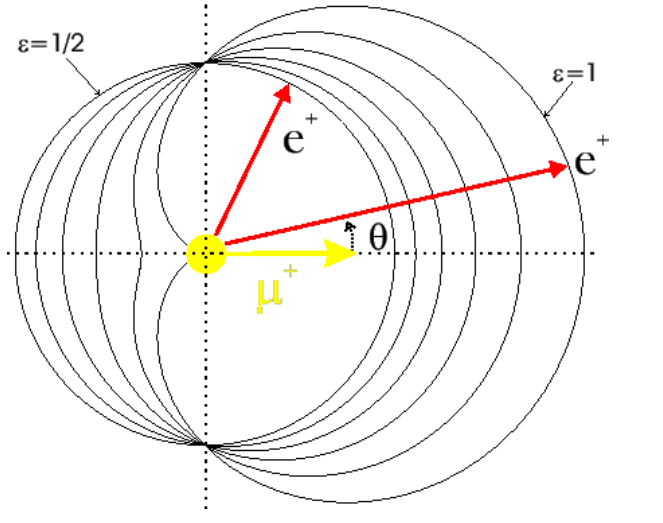

Fig 3.3 The asymmetric emission of a positron following a muon decay event.

where α(ε) depends on the positron kinetic energy, ε, and varies from from α = 1 for the maximum energy ε = 52 MeV to α = -1/3 for ε = 0. Because we do not detect just the highest energy muons, we can average this over all possible energies, which yields an average asymmetry for positron emission of α = 1/3.

From section 3.3.1 we see that we may prepare an ensemble of muons all with the identical initial state given by the fixed spin direction when they enter the sample. Because of the parity violation in the muon decay described above, we now also have a method of detecting the muon spin at the time of the decay. However, this decay is probabilistic in that not all positrons will be emitted directly in the direction of the muon spin, so we must collect many decays for each time that we are interested if we wish to determine the actual spin at some time *t*. As the muon decays with a characteristic lifetime of ~2.2 μs each individual decay may occur at a random time *t,* by measuring many decay events we may also measure the spin not just for a single time *t*, but as a semi-continuous function of time [13]. The next section will describe facilities which produce these muons and the details of how these detectors work and how they are used to extract useful information which can be analyzed to learn more about the magnetic state of the sample.

3.4.4 Muon Sources and Detectors

Muon sources come in one of two varieties, continuous sources such as is available at the Paul Scherrer Institute (PSI) in Switzerland, and pulsed sources such as is available at the Rutherford-Appleton Laboratories at ISIS (ISIS) in the UK. Data from both facilities will be presented so it is worth taking a moment to describe the specifics of each.

The source at ISIS is the highest flux of pulsed muons in the world, where a synchrotron creates pulses of 800 MeV protons at 50 Hz. Roughly 2 % of the outgoing

protons create muons resulting in pulses containing several hundred muons each [15]. The decay event timer starts when the pulse arrives, therefore very few stray events are detected allowing the observation time to be upwards of 20 μs (note that at only 1% of the muons haven't decayed by 10 μs and that number drops to 0.01% by 20 μs). Because many decays will be happening within a short time, many individual detectors are needed to catch all of the emitted positrons in this setup. EMU, the detector used in this work detector and shown in Figure 3.4(a), has 96 plastic scintillator/photomultiplier tube detectors to capture these events, allowing over 100 million decay events per hour to be observed[8]. The down side of pulsed sources is that the muons arrive over a finite time period, with an average pulse width of ~80 ns. Because of this, the detector has an effective bandwidth of around 6 MHz, and very short timescale decay events cannot be resolved. Pulsed sources are therefore more suitable to slow depolarization processes in which long times are needed, such as weak dynamical fluctuations in magnetic materials or for sensitive transverse field measurements such as probing penetration lengths in type II superconductors [16].

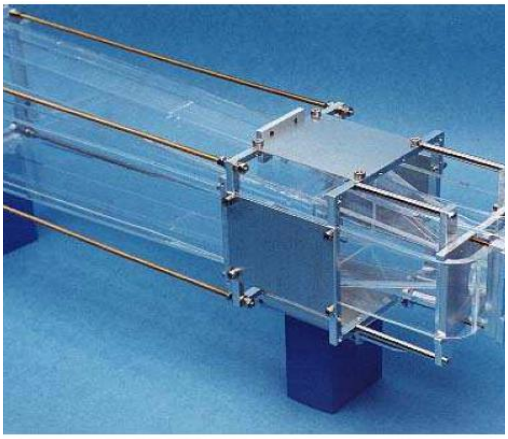

Figure 3.4 (a) EMU detector at ISIS (b) Scintillators inside GPS at PSI (Images courtesy of the ISIS and PSI Websites)

The muon source at PSI is the highest flux of continuous muons in the world; these are produced by protons which are accelerated in a cyclotron and therefore produce muons continuously [14]. This requires additional scintillators to act as the start timer and also to reject or 'veto' events in which two muons are in the sample simultaneously. As only one muon is in the sample at any given time during a valid decay event, the observation time is not limited to the pulsewidth and therefore very fast relaxation events are observable. The scintillator arrangement inside the detector at the General Purpose Spectrometer (GPS) at PSI is shown in Figure 3.4(b). However, the down side to this method is that the detectors are always 'looking' for events, so that there may be substantial background signal which limits the length of the observation time and must be accounted for in the analysis software. These sources also have considerably lower flux than pulsed sources to ensure that two muons are not in the sample simultaneously.

Both detectors record millions of decay events which are used to create a histogram of the positron emission asymmetry versus time based on the relative numbers of decays recorded in the forward (N_F) and backward (N_B) directions. Shown in Eq 3.7, an additional parameter α is used to account for differences in detector efficiencies, sample thickness, and other environmental factors, and must be determined experimentally [13]. The asymmetry is therefore a direct measured of the ensemble average of the muon polarization as a function of time, and will be used to extract meaningful physics about the local magnetic environment of the system.

$$A(t) = \frac{N_F - \alpha N_B}{N_F + \alpha N_B} \qquad (3.7)$$

The entire process of detecting and analyzing a muSR experiment is shown schematically in Figure 3.5, and may be described by a series of steps: (1) a spin-polarized muon (or muon bunch) enters the sample and the timer is started (2) the thermalized muon precesses in the local magnetic field (3) the muon decays as described above at some later time (governed by the mean lifetime), and the resulting positron is detected by the scintillators, (4) millions of these events are recorded and the number of decay events in different time bins is recorded (5) results from individual detectors are combined to give a plot of the asymmetry versus time according to Eq. 3.7.

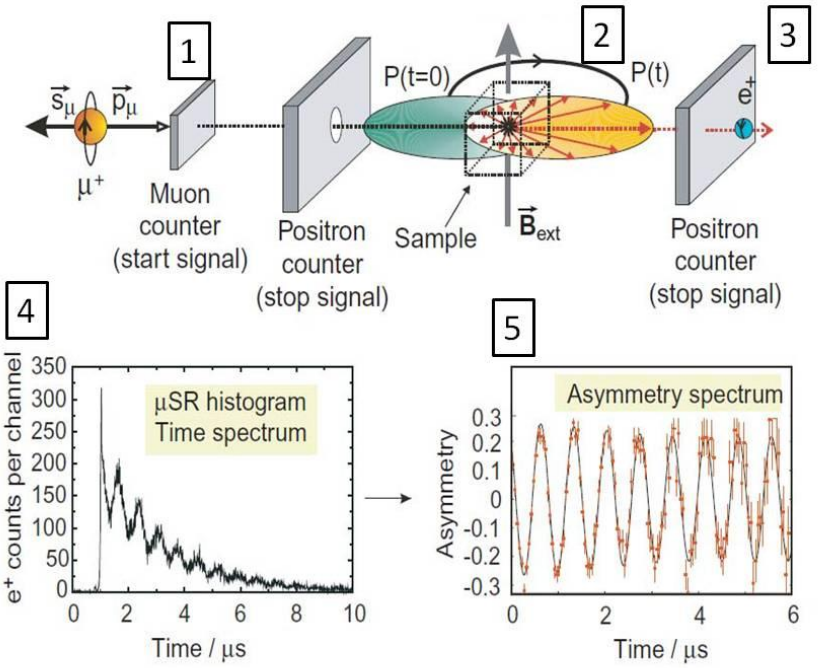

Figure 3.5 Schematic of μSR experiment. (1) The polarized muon enters and the timer is started. (2) The muon precesses due to magnetic fields, (3) the muon decays resulting in a positron being detected in one of several detectors, (4) Histograms are built of millions of decay events, (5) Adjusting for the muon lifetime, a plot of the asymmetry versus time is created from the histograms [17]

3.4.5 Basic Polarization Functions

In measuring the asymmetry as a function of time, we are attempting to measure the properties of the local magnetic fields $\boldsymbol{B}_{loc}$ experienced by the implanted muons in order to gain insight into the underlying magnetic structure or dynamic properties of the system of interest. To do this, we introduce models of various simplified conditions, *i.e.* randomly oriented static nuclear moments, fluctuating electronic moments, *etc*. for which analytic functions of the polarization versus time may be derived. The polarization, *P(t),*

is simply the measured asymmetry normalized to the initial value measured experimentally. There are several excellent texts which go into far more detail than space permits here [13], [18] therefore I will now only introduce a few of the simplest cases to aid in the explanation of results in future chapters. Much of the formalism and discsussion in the following sections is modeled after Ref. [13], [18].

First we consider quasi-static magnetic fields in the sample which are constant in time relative to the muon lifetime; in the next section we will discuss the effects of dynamical fields. In the simplest case, a single magnetic field $\boldsymbol{B}_{loc}$ is oriented at some angle θ to the initial muon polarization direction. From simple classical mechanics then, the resulting time-dependent polarization of the precessing muon will be described by,

$$P(t) = cos^2(\theta) + sin^2(\theta)\cos(\omega t) \qquad (3.8)$$

where $\omega = \gamma_\mu B_{loc}$ is the frequency of the muon precession as seen in Figure 3.5. In principle this equation is valid when every muon in the decay ensemble experiences the same local magnetic field, i.e., the field is perfectly uniform through the sample; clearly this is not a realistic situation. In practice the local field experienced by the muons stopping in different regions of the sample can be described by a distribution of fields. To calculate the depolarization function in a more general way, we may average Eq. 3.9 over a normalized field distribution $D_V(\boldsymbol{B}_{loc})$:

$$P(t) = \int [cos^2(\theta) + sin^2(\theta)\cos(\omega t)]\, D_V(\boldsymbol{B}_{loc}) d^3\boldsymbol{B}_{loc} \qquad (3.9)$$

If we consider now an isotropic distribution depending only on the magnitude the local field that is $D_V(\theta, \varphi, |\boldsymbol{B}_{loc}|) = D_m(|\boldsymbol{B}_{loc}|)$, we may integrate over the angular coordinates such that Eq. 3.9 may be simplified to only an integral of the magnitude of the local field:

$$P(t) = \frac{1}{3} + \int [cos^2(\theta) + sin^2(\theta)\cos(\omega t)]\, D_m(\boldsymbol{B}_{loc}) d\boldsymbol{B}_{loc} \qquad (3.10)$$

For example, in a perfect magnetically ordered polycrystalline sample the distribution may be represented by a delta function about of the static local field, $D_m = \delta(B_{loc} - B_0)$, and we find:

$$P(t) = \frac{1}{3} + \frac{2}{3}\cos(\omega t) \qquad (3.11)$$

The constant 1/3 is essentially the contribution of local fields which lie parallel to the initial polarization and thus do not contribute to oscillatory phenomena. An example of this can be seen in Figure 3.6 along with the depolarization for other static forms.

In the other extreme, we may consider a system in which the magnetic moments are not ordered in a uniform way, but rather are randomly oriented. This would occur for example, in a paramagnetic material with no dynamical fluctuation; this approximation is particularly useful for describing depolarization in materials with magnetically active nuclei which have spin-spin relaxation times on the order of milliseconds (~10^3 times the muon lifetime) at low temperatures. In this case, the field distribution is most aptly represented as a Gaussian of width Δ such that

$$D_V d^3\boldsymbol{B}_{loc} = \left(\frac{1}{\sqrt{2\pi}\Delta}\right)^3 \exp\left\{-\frac{1}{2\Delta^2}\left(B_{loc,x}^2 + B_{loc,y}^2 + B_{loc,z}^2\right)\right\} dB_{loc,x} dB_{loc,y} dB_{loc,z} \qquad (3.12)$$

Substituting Eq. 3.12 into Eq. 3.10 and integrating yields Eq. 3.13, known as the Gaussian Kubo-Toyabe depolarization function. This function was originally derived as an academic exercise to describe the shape of an NMR depolarization function in the absence of an applied external field [19].

$$P(t) = \frac{1}{3} + \frac{2}{3}(1 - \gamma^2 \Delta^2 t^2)\exp\left(-\frac{\gamma_\mu^2 \Delta^2 t^2}{2}\right) \qquad (3.13)$$

This form yields a characteristic shape of the depolarization shown in Figure 3.6 which is identified by a half oscillation with a minimum occurring at $t = \sqrt{3}/\gamma_\mu \Delta$ and which recovers to 1/3 at long times. Obviously, many other distributions beyond the constant field and Gaussian are possible, and many can be solved to form close-form analytic *P*(*t*), the blue curve in Figure 3.6(a), for example is the depolarization function for a Lortentzian distribution with a FWHM equal to Δ.

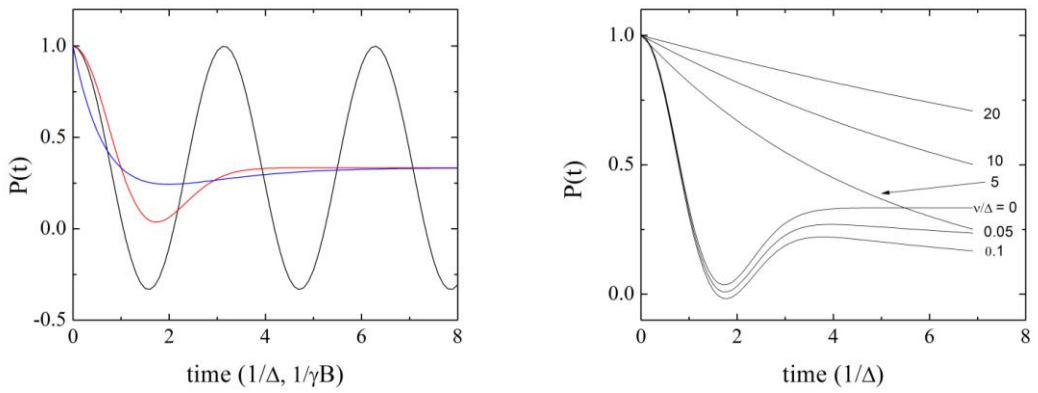

Figure 3.6. (a) Depolarization functions for polycrystal (black), Gaussian (red) and Lorentzian (blue) distribution functions calculated from Eq. 3.10. (b) Evolution of the Kubo-Toyabe function as a result of magnetic fluctuations. The functions shown are taken in either the slow or fast limits with the number beside each figure corresponds to the value of ν/Δ.

For systems which are neither perfectly ordered nor fully random, the resultant depolarization will be somewhere in between these two extremes depending on the correlation length. In general this will appear as a damping of the oscillating 2/3 component in Eq. 3.11 which decreases as the correlation length increases, and the distribution of the local field at the muon site become more uniform between unit cells. Derivations of other depolarization forms arising from other types of static arrangements of the local moments may be found in the excellent texts referenced herein (see [18] for example) and which may yield a more accurate representation of the local magnetism.

3.4.6 Dynamical Phenomena

In addition to static fields, μSR is also useful to examine dynamical effects over a large frequency range which spans the frequency gap from AC-susceptibility (kHz) to electron spin resonance (GHz) and inelastic neutron scattering (THz). There are two basic approaches in dealing with dynamical effects: the first is the purely phenomenological Bloch formalism developed for NMR, and the second is the stochastic or Markovian approach. I will outline the Markovian approach as it yields more limited cases and apply this to the terminology more typically used in the Bloch case.

The basic way of discussing dynamical fields is to examine the correlation function of the field as a function of time. The Markovian approach assumes that for the same point in space the correlation of the local field decays exponential which is characterized by a single correlation time τ_c as shown in Eq. 3.14.

$$\langle B_{loc}(t_0)B_{loc}(t_0+t)\rangle = \langle B_{loc}\rangle^2 \exp(-\nu_c t) \qquad (3.14)$$

As this process also describes diffusion, we may think of this as either a flipping of a localized moment somewhere, or of the muon 'jumping' to a new site via diffusion. In this case we can interpret $\nu_c = 1/\tau_c$ as the flip/jump rate. In the strong-collision model, the polarization at time t contains contributions from muons which jump at time t ($P_0(t)$), 'jump' once before *t ($P_1(t)$)*, twice *($P_2(t)$)*, and so on *($P_n(t)$)* such that

$$P(t) = \sum p^i(t) \qquad (3.15)$$

For the case of a single jump we find:

$$p^0(t) = p_0(t)e^{-\nu_c t} \qquad (3.16)$$

Where *$p_0(t)$* is the polarization function describing a static distribution of fields as in 3.4.5. If the muon first jumps at time t_1, and again at *t* this is described by:

$$p^1(t) = \int_0^t dt_1 e^{-\nu_c(t-t_1)} p_0(t-t_1) e^{-\nu_c t} p_0(t_1) \qquad (3.17)$$

For each additional jump another integral must be performed, which leads to an infinite series which must be terminated and numerically integrated to give a total depolarization function. Kubo and others showed that one could take the Laplace transform of this series as a way of examining analytically several important limits rather than terminate the series or turning to numerical methods. For brevity, I will discuss the implications of this method, and point to several other works in which detailed derivations may be found.

The two limited cases of interest occur when the fluctuations are either very fast or very slow. For our Gaussian distribution of fields, the minimum of the polarization

function occurs at ~ $1/\gamma\mu\Delta$. If the fluctuations (or jumps) are such that $\nu_c/\gamma\mu\Delta >> 1$ we may consider this the "fast-fluctuation" or "motional-narrowing" limit. In this case the local field is "reset" long before the depolarization reaches the Kubo-Toyabe minimum, and so the depolarization is given by an exponential function:

$$P(t) = \exp(-\lambda t), \qquad \lambda = 2\gamma_\mu^2 \Delta^2/\nu_c \qquad (3.18)$$

Comparatively, if we now look at the slow fluctuation regime, that is $\nu_c/\gamma_\mu\Delta << 1$, we find that the short time part of the depolarization is relatively unaffected as no jumps or fluctuations have occurred, and instead only the 1/3 "tail" found in Eq. 3.18 shows exponential behavior:

$$P(t) = \frac{1}{3}\exp\left(-\frac{2}{3}\nu_c t\right) + \frac{2}{3}(1-\gamma^2\Delta^2t^2)\exp\left(-\frac{\gamma_\mu^2\Delta^2t^2}{2}\right) \qquad (3.19)$$

The evolution of the depolarization function as function of fluctuation rate is shown in Figure 3.6(b) for several ratios of ν_c/Δ taken for either the slow fluctuation limit or the fast fluctuation limit. Here we can see that for intermediate values of ν_c both approximations poorly describe the resulting function; in this intermediate regime numerical simulations are required to fit the data. It should also be noted that in system with long-range magnetic order, dynamical depolarization of the longitudinal component by transverse fluctuations can produce signal damping, and this can be used to describe interactions of the muons with spin waves and other excitations.

For both static and dynamic situations, the asymmetry curves must be fit using suitable software to extract meaningful parameters. Typical examples are the *Wimda* package developed by Francis Pratt [20] at ISIS or *musrfit* developed by A. Suter and others at PSI [21].

3.5 Transport Measurements

As described in the introduction, the electrical transport properties of these materials are also of fundamental importance; these include the temperature dependence of the electrical resistivity and also the Hall effect. In this section I will describe how these properties are measured in our laboratory.

3.5.1 Electrical Conductivity and Resistivity

The electrical conductivity, σ, is defined as the proportionality constant between an applied electrical field and the resultant current density, or $\mathbf{J} = \sigma\mathbf{E}$. Because these are vector quantities, the conductivity is inherently a tensor and may contain off diagonal elements if magnetic fields are present; this is known as the Hall effect and will be discussed in the next section. In the absence of magnetic fields, these off diagonal components may be neglected and the resistivity is defined as simply the inverse of the conductivity. We generally report the resistivity rather than conductivity as it is the resistance $R = \rho L/A$ which is more commonly measured. The resisivity is an important measurement as it probes the

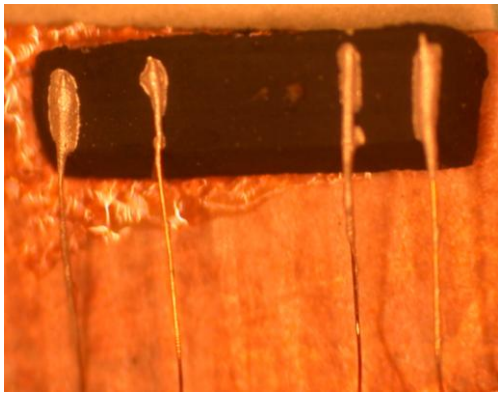

Figure 3.7 Four point setup to measure the electrical resistivity of Nd-227.

response of itinerant electrons in the system, and describes the average response due to various scattering effects and band structure of the material under investigation. While on the surface this may seem a rather trivial measurement, a great deal of care must go into the design and preparation of the system in order to obtain accurate results [22]. I will now outline the major problems in making accurate measurements and describe what is done to overcome them.

1. Small resistances. The first difficulty, particularly in metallic samples, is that the resistance of a sample is generally quite small, possibly even on the order of milli-ohms while the wires used inside a cryostat may be on the order of hundreds of ohms. To overcome this difficulty a four-point measurement is required, as shown in Fig. 3.7 for a sample of Nd-227. The outer two leads are used to inject current across the sample, while the inner two are used to measure the resulting voltage drop across the sample only. As the internal impedance of any voltage measuring device is very large, minimally over 100 MΩ, all of the current travels through the sample providing an accurate measurement of the resistance of the sample alone.

2. Joule Heating. Resistive components such as wires, the sample, and the junctions of the wires to the sample (contacts) are all sources of Joule heating once current is applied to the circuit, and will dissipate heat at a rate $P = I^2R$. This can be especially problematic at low temperatures where we are limited by the small cooling power and high vacuum environments of most refrigeration systems. This heating will create localized temperature differences, or increase the operating temperature of the refrigerator. Minimizing extraneous resistances in connections and contacts to the sample is necessary to reduce this effect, and even more importantly the current must be kept as

small as possible, typically well under a mA in most cases. This leads to the next problem – signal size.

3. Small Signals. When the applied currents are very small, it can be difficult to measure the resistance accurately above the background noise. One technique is to use a low frequency AC resistance bridge to utilize filtering techniques to reduce the background signal. The two devices used in our experiments are the LR 700 from Linear Research and the LS 370 from Lakeshore Inc. These sophisticated instruments inject an oscillating current at a fixed frequency and measure the resulting voltage drop with an internal lock-in amplifier which uses the orthogonality of sine waves to measure the response at only the applied frequency. This is unlike a DC voltmeter which is basically a broadband measurement and may sense signal from any nearby noise source. In every experiment, great care is taken to find the best operating parameters to maximize the signal to noise ratio without causing detrimental heating or other effects.

For very large resistance samples, such as insulators or semiconductors at low temperatures, another type of instrument known as an electrometer may be used. This device is similar to a DC digital voltmeter, however typically has an input impedance of well over 100 GΩ and in some cases over 2 TΩ allowing resistances of many GΩ to be measured accurately. This device can also be used as a sensitive current meter and has been used to measure IV curves at 300 mK for $Sr_3Ir_2O_7$, for example [23].

3.5.2 Hall Effect

As mentioned in the previous section, the conductivity tensor may contain off diagonal elements if magnetic fields are present; these will inherently lead to a transverse voltage perpendicular to the applied current known as the Hall effect or Hall voltage. Contributions to the Hall effect may be divided into two broad categories: 1) the normal Hall effect due to the semi-classical motion of charge carriers in an external magnetic fields, and 2) the Anomalous Hall Effect (AHE) which occurs in materials with either ferromagnetic or non-collinear magnetic structures. Both occur in pyrochlore materials and will be discussed now.

The typical bar geometry used in Hall effect measurements is shown schematically in Figure 3.8(a). An external current source (AC or DC) injects a current of constant amplitude I along the sample (x-direction), with a magnetic field B_z applied normal to the surface, the resulting Hall voltage is then measured perpendicular to both (y-direction) [24].

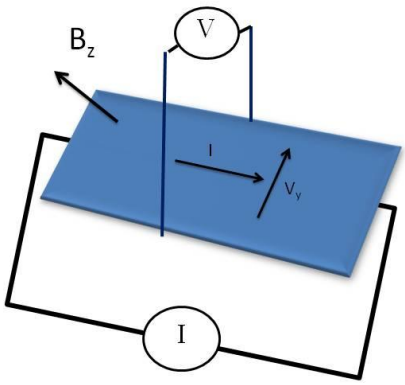

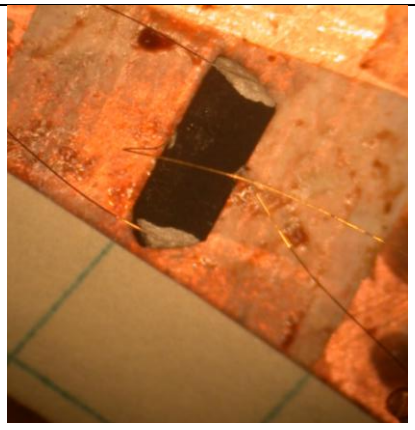

Figure 3.8 (a) Geometry for a typical Hall Effect measurement [Image courtesy of Warwik University] . (b) Typical Hall Sample used in this work, the spacing of the graph paper is ¼" for scale. The wires are 2 mil Au attached using silver paint.

The transverse motion due to the Lorentz force, $\vec{F} = q\ (v_x \times B_z)$ will cause the mobile charge of magnitude q to accumulate along one side of the sample resulting in a net transverse electric field ε_y counteracting the Lorentz force from the magnetic field until steady state is reached, such that the total force on a charge carrier is $\vec{F} = q\ (v_x \times B_z) + q\varepsilon_y$ [6]. Using the fact that that $I = J*wt = nqv*wt$, where n is the carrier concentration, we can easily show that for the normal Hall effect $V_H = R_{xy}I$ where:

$$R_{xy} = \rho_{xy}t = R_H Bt \qquad (3.20)$$

Here, R_{xy} is the Hall resistance, ρ_{xy} is the Hall resistivity, and R_H is known as the Hall coefficient, given by $R_H = 1/nq$ in the simple case of a single type of carrier. If the band structure is sufficiently complex and both types of carriers are present, this simple expression breaks down, and the resulting Hall effect voltage depends on the ratios of the mobilities of the respective carriers [25]. As the R_H depends on the inverse of the carrier concentration, this becomes quite easy to measure in insulators while requiring significant more care in metals and degenerate semiconductors, therefore the precautions described in 3.5.1 must be used here as well to obtain accurate measurements.

Additionally, leads and samples are never perfectly aligned or of uniform thickness throughout, therefore any measurement of the transverse resistance will inherently contain a fraction of longitudinal resistance, $R = R_{xy} + R_{xx}$, both of which may be functions of magnetic field. In order to separate the two, we rely on the fact that from Eq. 3.20 R_{xy} is odd or antisymmetric with respect to field, while R_{xx} must be even. By measuring the transverse resistance as a function of magnetic field for both positive and

negative field values, we find the antisymmetic and symmetric components which will yield the true transverse and longitudinal values:

$$R_{xy} = (R(B) - R(-B))/2 \qquad R_{xx} = (R(B) + R(-B))/2 \qquad (3.21)$$

we can use the relations derived above to then extract carrier densities, *etc*., from this corrected transverse resistance.

The origin of the AHE is somewhat more subtle, and in fact a complete theoretical description has been the source of conflict ever since it was first discovered in the early 1930's. Since then several excellent reviews have been written on this subject which treat the problem in far more detail than may be given here; therefore I will only point on several important conclusions. In general, the anomalous Hall effect is the result of broken time reversal symmetry in the presence of spin-orbit coupling [26]. This is particularly strong in ferromagnets where the magnetization is large and does not vary spatially over the extent of an electron mean free path. The Hall resistivity is often written empirically as the sum of two terms:

$$\rho_{xy} = R_H B_z + R_S M \qquad (2.20)$$

R_H is the normal Hall coefficient described in the previous section, and R_S is the anomalous coefficient which was found to be proportional to ρ_{xy}^{α}, $\alpha = 1$ or 2 depending on the material.

There are three contributions that give rise to the AHE: intrinsic, skew scattering, and the side-jump. The intrinsic contribution stems only from the band structure and magnetic order of the material: an electron traversing along a closed path may obtain a non-zero Berry phase; this will give rise to a fictitious magnetic field which will couple to the actual motion of the electron. Skew scattering arises when there is an unequal

probably of transition between opposite moving Bloch states due to spin orbit coupling of the conduction electrons to local moments, modifying the Boltzmann transport equations. Side jump mechanism is due to impurities and other external factors which may arise due to scattering in particular cases [26].

Because the Hall effect now depends on the magnetization and not just applied field, in measuring the AHE we must take into account the effects of hysteresis discussed in 3.3.2 for magnetization. Therefore, in the measurements presented in this work the Hall effect has been measured over a complete loop. The asymmetric components are taken for a single sweep direction beginning at $+B$ and sweeping down to $-B$, or vice versa. We then have two sets of field dependent Hall measurements which can be compared to examine the effects of magnetic hysteresis. Because of the relationship with the magnetization of the sample, the AHE may be comprised of reversible and irreversible components. The field dependence of the reversible component can be found by taking the average of the 'up' and 'down' sweep directions; this gives the contribution to the signal from the normal Hall effect which has no field history effects, as well as the anomalous part due to the coupling to the field dependent magnetism which results from reversible processes like rotations of the magnetic domains and elastic motion of the domain walls. The irreversible component on the other hand is defined as the difference between the 'up' and 'down' sweep directions and is only contains contributions from the hysteretic part of the coupling of the carriers to the magnetization and includes effects due to discontinuous domain formation and movement, for example [26].

3.6 Cryostats

Transport measurements to 2 K have been performed in one of several cryostats: a gas-flow SVT by Janis Instruments, a cryogen free cryostat built by Janis, or the Physical Property Measurement System (PPMS) built by Quantum Design. The Janis gas flow and PPMS utilize the flow of cold helium vapor across the sample under a pressure slightly under one atmosphere, and are used in conjuction with a superconducting magnet to produce fields of up to 9 T. The cryogen free Janis system utilized a Gifford-McMahon cryocooler to reach temperatures of roughly 3 K with the sample in high vacuum, and does not have magnetic field capabilities. Special cryostats that utilize ^{3}He, a rarer isotope of helium must be used to get below the 2 or 3 K limit of the other systems. The two systems which will be described in this section are the ^{3}He adsorption refrigerator and a ^{3}He/^{4}He dilution refrigerator. In this section I will give brief description of these two and how they are used in experiments.

2.6.1 ^{3}He Cryostat

Refrigerators based on ^{4}He can easily reach temperatures of ~ 1.5 K by using a large throughput vacuum pump to reduce the vapor pressure above the liquid and thus lower the temperature of the bath. The lowest temperature is typically limited by several factors, one is that as the temperature is lowered the vapor pressure decreases exponentially, meaning that the throughput of the vacuum pump must increase exponentially, another is that at low temperatures residual heat leaks into the bath system can dominate the evaporative cooling [Richardson]. Practically however, this cooling is

also limited because of the large amount of liquid helium (LHe) that is boiled away as the temperature is reduced through the superfluid transition at 2.2 K. To reach lower temperatures, we may use the ^{3}He isotope of helium which due to its lighter mass liquefies at 3 K rather than 4.2 K, and may be pumped under its own vapor pressure to below 300 mK. However, as ^{3}He is a very rare isotope (most of the ^{3}He in use is the by-product of tritium decay in high flux nuclear reactors), we cannot simply pump it away into the atmosphere as with ^{4}He [27].

The refrigerator used in our laboratory is a Janis He-3-SSV, shown in Figure 3.9, and operates in two stages. In the first stage, liquid ^{4}He is taken in from the bath and pumped on inside the "He4 Pot" to below the liquefaction temperature of ^{3}He, typically operating below 1.6 K for efficiency. The ^{3}He gas reservoir is stored above in an external tank with a thin tube running through the He4 pot; this gas is then liquefied and drops down into the lowest chamber labeled "He3 Pot" in the figure. In order to get below 1.6 K, cold He gas from the bath is around a piece of activated charcoal (the Sorb) which is inside of the sealed He3 gas system. Because of the large surface energy of the sorb, He3 vapor adsorbs to its surface, effectively lowering the vapor pressure above the liquid, resulting in a reduction of the temperature of the liquid.

To reduce convective cooling between different parts of the system, the section shown in Figure 3.9 is placed under a high vacuum ($\sim 10^{-6}$ torr) by a turbo or diffusion pump. Phosphor bronze and manganin wires are used instead of copper to provide electrical connections to the experiment platform as they have poor thermal conductivity and reduce the heat flow from the room temperature top of the fridge. For a properly

designed experiment, base temperatures of 320-350 mK are routinely reached in this system.

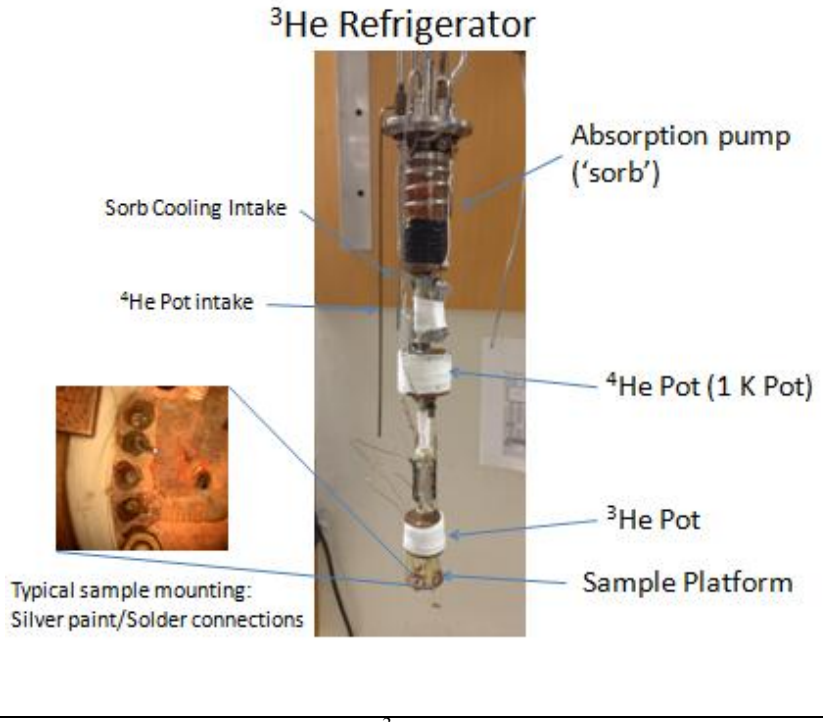

Figure 3.9 Image of the Janis ^{3}He Refrigerator used in our lab

The drawback to this system is that the ^{3}He is not continuously recondensed so that eventually it will all be collected onto the sorb and the temperature will begin to rise; to reach base temperature again the Sorb must be warmed to remove the adsorped ^{3}He so that it may be recondensed and cooled to base again. Because of this, this type of system is known as a 'single shot' refrigerator, however holding times of up to 24 hours are possible if the temperature is kept well below the boiling point of ^{3}He. To reach temperatures above 2 K without immediately boiling away the ^{3}He, the sample platform is thermally isolated from the ^{3}He Pot by G10 fiberglass posts, and either brass wire or a

brass post is used to provide a weak thermal connection. By attaching a suitable resistance heater to the experiment platform the temperature may be varied from ~300 mK to several Kelvin while maintaining a stable ^{3}He pot level and extending the time duration of the run. Experiments ranging from transport, magnetization and heat capacity are all routinely performed in this manner.

2.6.2 Dilution Refrigerator

If temperatures lower than 300 mK are required, or an experiment needs to be operated for an extended period of time, a dilution refrigerator (DR) must be used. This is a complex system which uses a mixture of ^{3}He and ^{4}He isotopes which are continuously circulated, and may reach temperatures of only a few millikelvin if designed properly. While the details of the entire operation of this system are beyond the scope of this work, I will for the sake of completeness give a brief overview of the cooling mechanism.

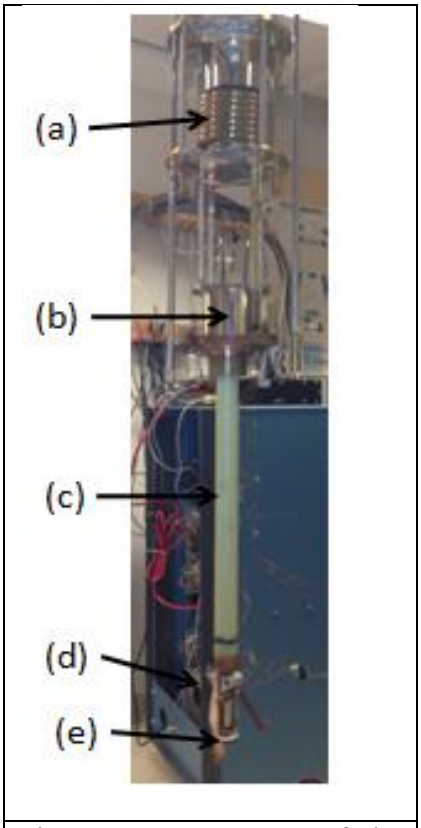

Fig. 3.10 Lower part of the Oxford MX50 Dilution refrigerator with transport platform. (a) heat exchanger, (b) mixing chamber, (c) G10 tube weak thermal link/extension (d) sample platform, (e) RuO_2 thermometer (Lakeshore)

The DR relies on the fact that due to the quantum mechanical zero-point motion of the helium atoms, a finite amount of ^{3}He remains soluble in ^{4}He even to absolute zero [28], [29]. A critical point exists at 800 mK, depending upon the initial ^{3}He concentration which is typically around 15 % of the total volume, below which the mixture phase separates into a ^{3}He poor (dilute) phase containing $\geq$ 6% ^{3}He and a ^{3}He rich (concentrated) phase with is 100% ^{3}He. The phase boundary between a ^{3}He rich phase and a ^{3}He poor phase is established inside the mixing chamber (b). By pulling out ^{3}He from the dilute phase, we force diffusion of ^{3}He from the concentrated to the dilute side which adsorbs heat from the surrounding area. The ^{3}He that is pulled away is then recirculated through pumps and introduced into the rich phase again so the process can run continuously. Careful engineering of the heat exchangers (a) are required to minimize the amount of heat flow from the circulating mixture into the mixing chamber. The experiment may either be bolted directly to the mixing chamber, placed inside the mixing chamber (top-loading system) or as shown in Figure 3.10 attached indirectly via a weak thermal link so the temperature may be varied above 1 K. As the cooling power of the DR is quite small (50 μW at 100 mK) extreme care must be taken in order to minimize

additional heat loads from the sample platform connections (d) and joule heating as a result of (e) resistive thermometers [27].

3.7 Conclusions

In this chapter I have discussed at length the experimental techniques which I will be using to investigate several members of the pyrochlore iridates. I should point out at this point that an important technique which was not described here but used extensively in this work is elastic neutron scattering; these measurements were performed entirely by members of Prof Stephen Wilson's group, and as such I will merely be discussing the results in subsequent chapters. As each technique has its own strengths and weaknesses, it is the goal of my work to utilize several diverse tools in order to obtain a more complete understanding of the interactions which give rise to such interesting phenomena in these materials This work is of substantial importance because such broadly based studies utilizing many different techniques have been lacking in these materials. It is of vital importance that comprehensive studies such as this are done to ensure that the proper conclusions are reached and not biased based on one technique alone.

Chapter 3 References

[1] A. R. West, *Basic Solid State Chemistry* (John Wiley and Sons, Chichester, 1997)

[2] W. D. Callister, *Materials Science and Engineering, An Introduction* (John Wiley and Sons, United States of America, 2003)

[3] S. M. Disseler, C. Dhital, A. Amato, S. R. Giblin, C. de la Cruz, S. D. Wilson, and M. J. Graf, Physical Review B 86 (2012).

[4] S. M. Disseler, C. Dhital, T. C. Hogan, A. Amato, S. R. Giblin, C. de la Cruz, A. Daoud-Aladine, S. D. Wilson, and M. J. Graf, Physical Review B 85 (2012).

[5] J. Rodriguez-Carvajal, Physica B **55** 192 (1993).

[6] N. Ashcroft and N. Mermin. *Solid State Physics* (Brooks Cole 1976)

[7] L. D. Landau and E. M. Lifhitz. *Statistical Phyiscs I* (Butterworth-Heinemann 1980).

[8] S. Blundell. *Magnetism in Condensed Matter* (Oxford University 2001).

[9] H. Czichos, T. Saito, and L. Smith, Handbook of Materials Measurement Methods (Springer Science and Buisness Media, Leipzig, 2006).

[10] http://www.qdusa.com/products/mpms.html

[11] A. Schenck, Physics Letters a A 32 (1970).

[12] D. Griffths, *Introduction to Elementary Particles* (Wiley-VCH, Weinheim, 2008)

[13] A. Schenck, Muon spin rotation spectroscopy : principles and applications in solid state physics (Bristol, Boston, 1985).

[14] A. Amato, *GPS User Guide*. //lmu.web.psi.ch/facilities/gps/User Guide version march 2006.pdf, 2006).

[15] J. Lord, *The EMU Users Guide.* http://www.isis.stfc.ac.uk

[16] A. J. Greer and W. J. Kossler, Low magnetic fields in anisotropic superconductors (Springer, Heidelberg, Germany, 1995).

[17] E. Morenzoni, *μSR: An Introduction.* http://www.neutron.ethz.ch

[18] A. Yaouanc and P. D. de Reoteir, *Muon Spin Rotation, Relaxation, and Relaxation: Applications to Condensed Matter* (Oxford University Press Inc, New York, 2011).

[19] R. S. Hayano, Y. J. Uemura, J. Imazato, N. Nishida, T. Yamazaki, R. Kubo, Phys. Rev. B **20** 850 (1979).

[20] F. L. Pratt, Physica B 710, 289 (2000).

[21] A. Suter and B. M. Wojek, Physics Procdeia 30, 69 (2012).

[22] R. C. Richardson and E. N. Smith, Experimental Techniques in Condensed Matter Physics at Low Temperatures, edited by D. Pines (Addison-Wesly Publishing Company, California, 1988), p. 338.

[23] Chetan Dhital, Sovit Khadka, Z. Yamani, Clarina de la Cruz, T. C. Hogan1, S. M. Disseler, Mani Pokharel, K. C. Lukas1, Wei Tian, C. P. Opeil1, Ziqiang Wang, and Stephen D. Wilson. Phys. Rev. B **86**, 100401(R) (2012).

[24] W. R. Runyan and T. J. Shaffner, Semiconductor Measurements and Instrumentation (McGraw Hill, New York, 1998), p. 454.

[25] S. O. Kasap, *Principles of Electronic Materials and Devices* (McGraw Hill, New York, 2006).

[26] N. Nagaosa, J. Sinova, S. Onoda, A. H. MacDonald, and N. P. Ong, Reviews of Modern Physics 82, 1539 (2010).

[27] D. S. Betts, *An Introduction to Millikelvin Technology* (Cambridge University Press, New York, 1989)

[28] J. C. Wheatly, O. E. Vilches, and W. R. Abel, Physics 4, 1 (1968).

[29] 22 J. C. Wheatly, R. E. Rapp, and R. T. Johnson, Jour. Low. Temp Phys 4, 1 (1971).

Chapter 4: $Y_2Ir_2O_7$ and $Yb_2Ir_2O_7$

The goal of this chapter is to present results from muon spin relaxation/rotation, magnetization, neutron scattering, and transport measurements on polycrystalline samples of the pyrochlore iridates $Y_2Ir_2O_7$ (Y-227) and $Yb_2Ir_2O_7$ (Yb-227). Much of this chapter, including many of the figures have been adapted from the article "Magnetic order in the pyrochlore iridates $A_2Ir_2O_7$ (A = Y, Yb)" by S. M. Disseler *et al*., published in Phys. Rev. B **86** 014428 (2012). To summarize, well-defined spontaneous oscillations of the muon asymmetry are observed together with hysteretic behavior in magnetization below 130 K in Yb-227, indicative of commensurate long-range magnetic order. Similar oscillations are observed in Y-227 below 150 K; however, the onset of hysteretic magnetization at T = 190 K indicates a transition to an intermediate state lacking long-range order. Our results also show that insulating members of the iridate family have nearly identical magnetic Ir^{4+} ground states, and that the presence of magnetic A-site species does not play any significant role in altering the ground-state properties. Indeed, I present evidence that the Yb^{3+} ions may order independently from the Ir^{4+} at a much lower temperature.

4.1 Introduction

Described in the introductory chapters, the combination of frustration, spin-orbit interaction, and electronic correlations which may all be relevant in the pyrochlore iridates put the series at the intersection of many of the most important developments in condensed matter physics over the last half-century. Early measurements indicated that the ground state electrical and magnetic properties depend strongly upon the radius of the rare earth *A*-site, with the smaller members of the series exhibiting insulating behavior and a magnetic transition above 100 K [1, 2], while the largest members are metallic and lack long-range magnetic order to 25 mK [3, 4]. The appearance of spontaneous oscillations in muon spin relaxation/rotation (μSR) measurements of Eu-227 below this temperature provided convincing evidence of a transition to a state with long-range order (LRO) [5]. As Eu^{3+} has a $J = 0$ Hund's rule ground state, the oscillations can be attributed to magnetic order of the Ir^{4+} moments.

Based on these early results it was speculated that the magnetic transition may be Mott-like, driven by electron correlations that split the narrow $j_{eff} = ½$ band formed by the *5d* band of the Ir^{4+} ions. Other iridates that are part of the Ruddlesden-Popper series such as Sr_2IrO_4 and $Sr_3Ir_2O_7$ [6, 7] have shown similar behaviors, however these are essentially layered compounds which can be discussed in terms of quasi-two dimensional behavior; the pyrochlore iridates represent one of the few fully three-dimensional iridate compound fabricated to date. Because of the added symmetries of the three-dimensional pyrochlore lattice, numerous exotic topological states have been theorized to exist in this family. It is thus important to characterize additional members of the *A*-227 family to

gain insight into the competing interactions in this system, the resultant magnetic ground states, and the prospects for observing novel topological states of matter.

This chapter will focus on measurement of two members of this series which have *A*-site radii which are smaller than that of Eu, and therefore are expected to have a similar insulating and magnetically ordered ground state based on magnetization measurements by Matsuhira [8] and Maeno [1]. It is not known however, what the magnetic structure of these materials are, and how that might change as the structure is distorted by variation of the important lattice parameters as discussed in the introduction. Furthermore, work in the pyrochlore titanates has revealed a plethora of interesting ground states which remain a topic of intense investigation to this date [9]; it is only natural to question what the role of these large local moments might be when surrounded by a second magnetic sublattice, and how subsequent exchange interactions may affect the previously observed magnetic order. The following chapter presents a thorough investigation of the bulk and local magnetism in two different pyrochlore iridates which have different lattice parameters, and contain both magnetic (Yb-227) and non-magnetic (Y-227) rare earth sites; it is the hope that through this study we will be able to answer as many of these questions as possible in addition.

4.2 Results: $Y_2Ir_2O_7$ and $Yb_2Ir_2O_7$

4.2.1 Synthesis and Characterization

Polycrystalline samples of $A_2Ir_2O_7$ (A = Y, Yb) were synthesized as described in Chapter 3; all samples were determined to be nearly phase-pure with the exception of two

minor impurity phases of IrO_2 and A_2O_3 (A = Y, Yb) each individually comprising less than ~1% of the total volume fraction. X-ray diffraction measurements were performed on a Bruker D2 Phaser diffractometer on both of the above two samples at room temperature for crystal structure determination. Using the cubic Fd-3m space group, the lattice parameters were found to be a = 10.1699(4) Å for Y-227 and 10.1015(5) Å for Yb-227, with the free parameter on the O 48f site x/a determined to be 0.3527 and 0.3505 respectively. Polycrystalline $Y_2Ir_2O_7$ was also probed via neutron diffraction measurements inside of a closed cycle refrigerator at the High Flux Isotope Reactor (HFIR) at Oak Ridge National Lab on the HB2-A diffractometer. Data from HB-2A were collected with λ_i=1.5385 Å, a Ge(115) monochromator, and 12'-31'-6' collimations. All diffraction data were refined using the FullProf software package. The XRD and neutron diffraction patterns along with refinement can be seen in Figure 4.1.

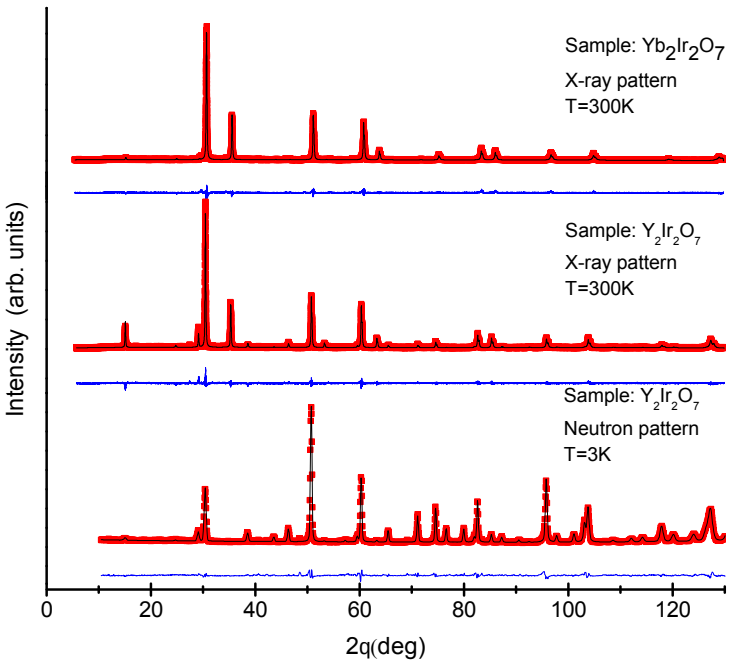

Figure 4.1. XRD patterns for (a) Y-227 and (b) Yb-227 with Rietvald refinement. (c) Diffraction pattern from elastic neutron scattering of Y-227 at 3 K.

4.2.2 Resistivity and Susceptibility

The electrical resistance was measured using a standard four-terminal ac bridge technique discussed in Chapter 2, inside a gas-flow He-refrigerator with a temperature range 2 K <.T < 300 K. Bulk magnetization was measured between 300 K and 2 K using a Quantum Design MPMS at the characterization facility at ISIS. The magnetization data were taken during warming in a 1 kOe applied field preceded by cooling from 300 K to 2 K in either zero field (ZFC) or 1 kOe (FC).

The temperature dependent static susceptibilities, $\chi = M/H$, for Y-227 and Yb-227 are shown in Figures 3.2(a) and 3.2(b) respectively. Under ZFC conditions we observe a

peak for Y-227 at T = 180 K, while FC conditions show a sudden increase beginning at 190 K, and a second inflection near 150 K. A similar bifurcation is observed in χ for Yb-227 at 135 K, as seen in the inset of Figure 4.2(b), although it is superimposed on a much larger paramagnetic component. The difference between ZFC and FC below the bifurcation temperature is of similar magnitude in both samples (of order 10^{-2} emu/mol), suggesting that the bifurcation arises from the Ir-sublattice, with an additional large paramagnetic contribution in Yb-227 due to the weakly coupled Yb^{3+} ($J = 7/2$) moments.

The temperature dependence of the zero field resistivity is shown in Figures 4.2(c) and 4.2(d) for Y-227 and Yb-227, respectively. Both samples exhibit monotonically increasing resistivity with decreasing temperature, with resistivity of approximately 30 Ω-cm at room temperature, and which exceed 1 MΩ-cm by 10 K. Neither sample has a resistivity that follows a thermally activated exponential behavior expected for simple semiconductors, indicating these materials are not band insulators. Systems which become insulators due to localization of electrons due to defects (Anderson localization) or correlations (Mott insulators) are often instead found to obey variable range hopping (VRH) phenomenology in which electrons hop from site to site with a probability which diminishes continuously with hopping distance [10]. In *d* dimensions the resistivity is found to vary with temperature as:

$$\rho = \rho_0 \exp\left[-(\mathrm{T}/\mathrm{T}_0)^{\frac{1}{d+1}}\right] \qquad (4.1)$$

Because of the cubic symmetry, it is natural to assume a three-dimensional system ($d = 3$), therefore we plot the log of the resistivity normalized by the value at 300 K versus $T^{-1/4}$ in the insets of Figure 4.2(c) and 4.2(d) for Y-227 and Yb-227 respectively. A

study of single crystal Eu-227 also found this behavior below the magnetic transition at 120 K indicating that this not a sample dependent phenomena [11]. This establishes that the insulating behavior at low temperatures is due to electron localization, rather than a simple gapped band-structure with non-interacting electrons. Although these compounds are semiconducting at high temperatures, the onset of the VRH behavior also provides a measure of the strength of the correlations similar to the true metal-insulator transition observed in some compounds at T_{MI}.

Several samples from different batches yielded identical results to these, although only those of one sample are shown. A sample of Y-227 was annealed in a flowing O_2 at 1000 C for 24 hours and was measured again with no change in the observed behavior, thus we conclude the samples are not oxygen deficient, and if anything contain a slight abundance of oxygen meaning that any deviations from stoichiometry would be in the direction of excess Ir^{4+}. These samples exhibit much stronger insulating properties than previously reported [1], most likely due to reduced impurity carrier contributions and/or a more uniform oxygen stoichiometry. Recently, a series of single crystals Eu-227 with small variations in stoichiometry were studied via transport and susceptibility in which detailed x-ray absorption measurements were used to verify the Eu to Ir ratio with much greater detail than achievable with EDXS alone [11]. In this study, samples with the most ideal stoichiometry exhibited the strongest temperature dependence of the resistivity, and followed the VRH formalism over the widest temperature region below T_{MI}. This suggests that the VRH is not a stoichiometric or site-disorder effect in these materials, but is intrinsic to these materials, and further suggests that this is the result correlations between the *d*-electrons.

It should be noted that many pyrochlore oxide materials show a strong stoichiometric dependence, a prime example is $Yb_2Ti_2O_7$ in which the polycrystalline samples were found to have consistently better stoichiometry and low temperature properties than single crystals [12]. While single crystal samples may be considered more useful as one can probe the magnetic and crystalline anisotropies more easily, the single crystal growth process is prone to the introduction of defects and distortions of the stoichiometry away from ideal cases. Therefore, while we may not be able to obtain all of the information we desire from our polycrystalline samples, I have a stronger confidence in the accuracy and reproducibility of the results presented in this thesis.

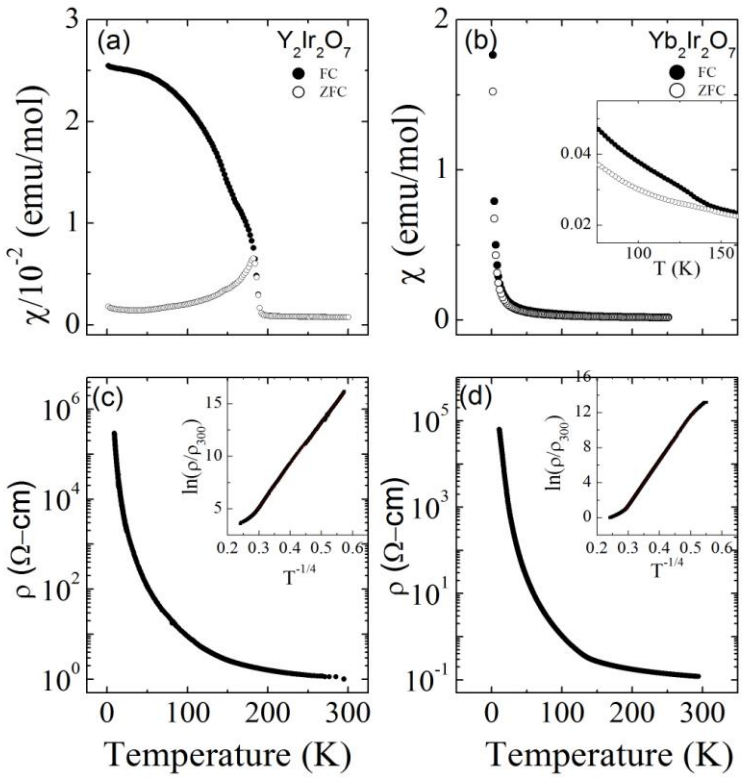

Figure 4.2: Temperature dependent susceptibility of (a) Y-227 and (b) Yb-227 with inset showing enlargement of data around bifurcation of Yb-227 near 130 K. Temperature dependent resistivity of (c) Y-227 and (d) Yb-227; insets show the log of the resistivity versus $T^{-1/4}$ according to VRH theory as described in the text.

4.2.3 Muon Spin Relaxation Measurements

It is worth noting that before discussing the results of our μSR results, elastic neutron scattering measurements were carried out as an initial probe of Ir^{4+} order for Y-227. Structural refinement of the data (Figure 4.1(c)) showed excellent agreement with the lattice parameters obtained from x-ray diffraction, and allowed for a greater refinement of the oxygen parameter at x = 0.3455. Neither new Bragg peaks nor changes

in peak height or locations were observed in measurements down to 3 K. This allows us to rule out any structural transitions within our resolution below T_M occurring with the magnetic transition. Conservatively, this powder measurement places an upper limit of the Ir^{4+} ordered moment with a $Q \neq 0$ wave vector of 0.2 μ_B and for $Q = 0$ mode of 0.5 μ_B based on the collected statistics and the resolution of the diffractometer. However neutron studies of small moment iridates often require single crystal measurements to resolve correlated spin scattering [6,7]. Shapiro et al., noted that as the orbital angular moment component projected into the t_{2g} states is l = -1, Ir^{4+} magnetic moment should have a maximum value of 0.33 μ_B, which is below the resolution of the detector $Q = 0$ modes [13]. Because of the magnetic anomaly clearly present in susceptibility, the use of another direct probe of the magnetic order is necessary to discern if this is due to magnetic order or spin-glass like phenomena.

As discussed in Chapter 2, μSR provides an excellent means of further probing the local magnetic order due to large gyromagnetic ratio of the muon ($\gamma_\mu/2\pi$ = 135.5 MHz/T) which makes it possible to detect static fields of few Gauss or less while simultaneously probing spin dynamics and correlations in the MHz regime [14]. Example asymmetry curves showing the early time behavior from PSI are shown in Figure 4.3(a) for Y-227 and Figure 4.5(a) for Yb-227. The most significant feature is the appearance of spontaneous muon spin precessions below T = 150 K and 130 K for Y-227 and Yb-227, respectively. These data signify the presence of a static local magnetic field $\langle \boldsymbol{B_{loc}} \rangle$ at the muon site. Furthermore, the oscillations are well defined with only a single characteristic frequency indicating commensurate order with a single magnetically unique muon

stopping site. The resultant asymmetry curves were fit by the simple depolarization function for a magnetically ordered polycrystal, as used in Ref [5] for Eu-227:

$$A(t) = A_1 \exp\left[-(\Lambda t)^{\beta}\right] \cos(\omega t + \phi) + A_2 \exp(-\lambda t) \qquad (4.2)$$

The first component describes the oscillations from muon spin precessing about a spontaneous static local field with frequency $\omega_\mu/2\pi = \langle \boldsymbol{B}_{loc} \rangle \gamma_\mu/2\pi$ and damping described by a stretched exponential with characteristic rate Λ and $\beta < 1$. The second component describes the relatively slower longitudinal relaxation due to spin-lattice relaxation or fluctuations of the local moments. Because this component also reflects muons for which the initial muon polarization is parallel to the internal field at the stopping site, we expect $\eta = A_2/(A_1 + A_2) = 1/3$ at temperatures well below the ordering temperature, and indeed we find that $\eta = 0.30(2)$ and 0.35(1) for Y-227 and Yb-227, respectively, when $T = 1.8$ K. The phase factor φ was found to be rather large for a system described by a single oscillatory frequency, which should be zero in the ideal case; nonetheless, suitable fits for both samples at all temperatures were obtained by fixing φ to -20°, the value obtained at 1.5 K.

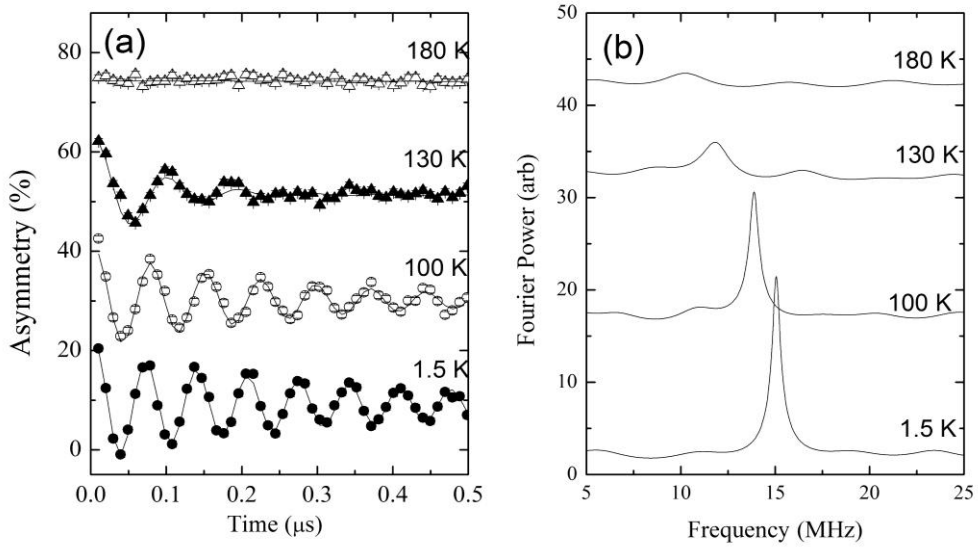

Figure 4.3 (a) Representative short time asymmetry data taken from GPS for Y-227 with curves offset for clarity and solid lines representing fits to Equation (1). (b) FFT transforms of the asymmetry data smoothed to highlight evolution of the peak.

For Y-227, the temperature dependence of ω_μ as determined from fitting to Eq. 4.2 is shown in the top panel of Figure 4.4. The onset of muon spin precession occurs near 150 K, and the precession frequency increases monotonically, reaching a maximum value of $\omega_\mu / 2\pi$ = 14.5(1) MHz at 1.6 K, corresponding to a low temperature value of $\langle \boldsymbol{B}_{loc} \rangle$ = 1100(10) G. This is also mirrored in the temperature dependence of the peak frequency when analyzing the data using the maximum entropy method [15] shown in Figure 4.3(b). This approach is similar to a Fast Fourier Transform, however the manner in which the resulting frequency spectrum is determined is quite different, see [15] for details. The occurrence of only a single peak in Figure 4.3 is verification of the existence of a single magnetically unique muon stopping site. This is somewhat unexpected given the complexity of the crystal structure, especially the number of oxygen sites which

would be likely stopping sites for the muon. This will be discussed in greater detail later in this chapter.

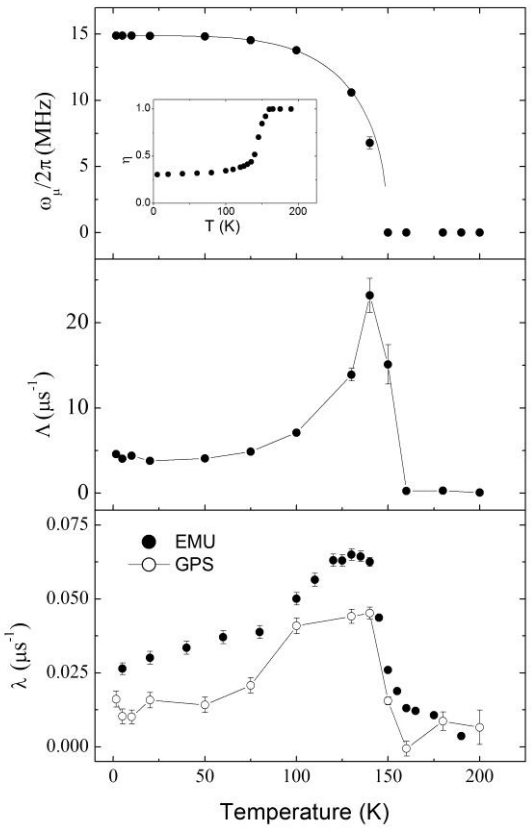

Figure 4.4. Temperature dependence of the parameters extracted from fitting Eq. 342 for Y-227 TOP: $\omega_\mu/2\pi$ with η inset; the solid line is a mean field fit, as described in the text. MIDDLE: Λ, solid lines are guides for the eyes. BOTTOM: λ from both GPS and EMU.

The resultant temperature dependence of the extracted frequency below 150 K is representative of the magnetic order parameter and is described by the phenomenological mean-field expression $\langle \boldsymbol{B_{loc}} \rangle \sim (1-(T/T_C)^{\alpha})^{\beta}$. It should be noted that this expression explicitly fits near the transition temperature, where we have few points. Nevertheless, as shown as the solid line in Figure 4.5, fitting to this expression to the entire temperature range yields values of $\alpha = 4.1(1)$ and $\beta = 0.29(2)$. The value of β is close to that expected for three-dimensional Ising systems [16], however the value of α is much larger than the value ~2 usually found for spin-wave excitations [17]. Fitting the data taken in Ref [5] this function revealed similar values for the critical exponents, indicating that these values

may be intrinsic to fluctuations about the non-coplanar magnetic order, which is expected to behave quite different from simpler higher, symmetry systems [18].

The appearance of the spontaneous precession occurs at a temperature significantly below the bifurcation temperature. We believe this behavior is intrinsic to the sample and indicative of a transition from a intermediate temperature magnetic phase with short-range order to a phase with long range order. XRD and neutron scattering have ruled out the presence of impurity phases above 1% volume fraction (and both impurity phases do not order magnetically), and μSR is a volumetric probe, so the success of Eq. 4.2 in describing the low-temperature depolarization curves, along with the longitudinal field results described below, rule out any coexistence of two phases at low temperatures.

Dephasing of the spontaneous muon spin precession is described by the phenomenological damping parameter Λ, shown in the middle panel of Figure 4.4 for Y-227. The sharp increase of Λ just below T_M is likely an artifact of the rapidly vanishing contribution to the asymmetry of the oscillatory component rather than critical divergence, as no such increase is seen in the paramagnetic region above T_M. The fractional quantity Λ/ω was found to be ~ 0.1 and constant at low temperatures, verifying that the internal field is fairly uniform at each muon stopping site except at temperatures near T_M. The stretching exponent β was found to be 0.6(1) and roughly temperature independent for Y-227 for temperatures below 120 K.

Shown in Figure 4.6, the onset of spontaneous muon spin precession is also observed in Yb-227 below T = 130 K, with a monotonic temperature dependence down temperatures near 20 K, with an extracted frequency $\omega_\mu/2\pi$ = 14.4(1) MHz ($\langle \boldsymbol{B}_{loc} \rangle$ = 1100 G) at 20 K. Below a characteristic temperature T* ~ 20 K, however, the frequency

is observed to increase again from 14.4 MHz to 15.5 MHz at 1.6 K, indicating the onset of a second contribution to the local field. Correspondingly, a second increase of Λ is observed below T^* indicating an increased width of $\langle \boldsymbol{B}_{loc} \rangle$.

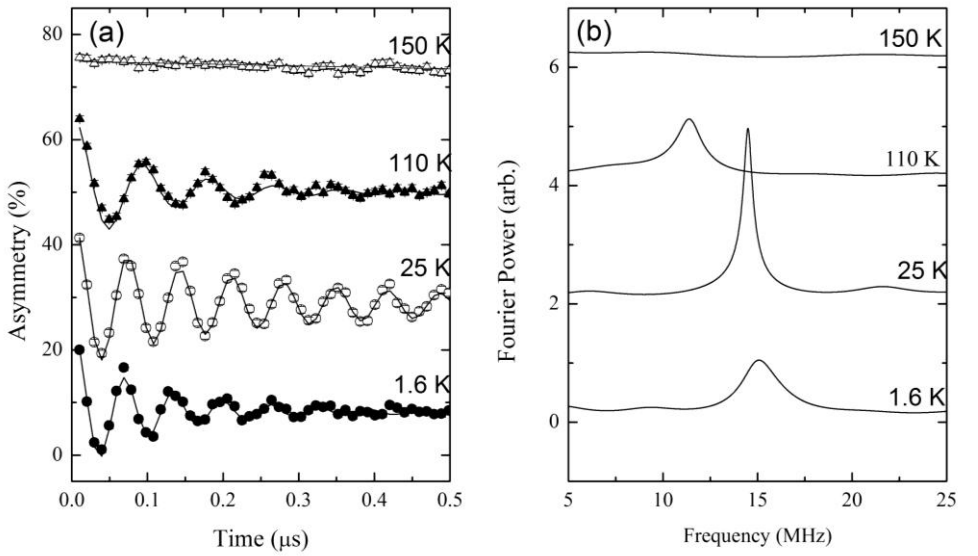

Figure 4.5. (a) Representative short time asymmetry data taken from GPS for Yb-227 with curves offset for clarity, and solid line representing fits to Eq. 4.2. (b) FFT transforms of asymmetry data.

The maximum entropy analysis of the asymmetry curves, seen in Figure 4.5(b), show that below T^* there is an increase in both the location and width of the peak and confirm the onset of an additional static local field. We do not observe any features in the magnetization near this temperature that would suggest a change in the magnetic order, and no such feature is observed in either Y-227 or Eu-227, which have non-magnetic ions on the *A*-site sublattice. A similar phenomenon was observed in the series *RFeAsO*, in which the localized rare earth moments become polarized via hyperfine or exchange

interactions with the ordered Fe lattice [19]. We find the temperature dependence of the muon spin precession frequency for Yb-227 is well described by the same modified mean-field form used in Ref [19] to describe CeFeAsO:

$$f = f_0 \left[1 - \left(\frac{T}{T_N}\right)^{\alpha}\right]^{\beta} \left[1 + \frac{C^*}{T-\theta}\right] \qquad (4.3)$$

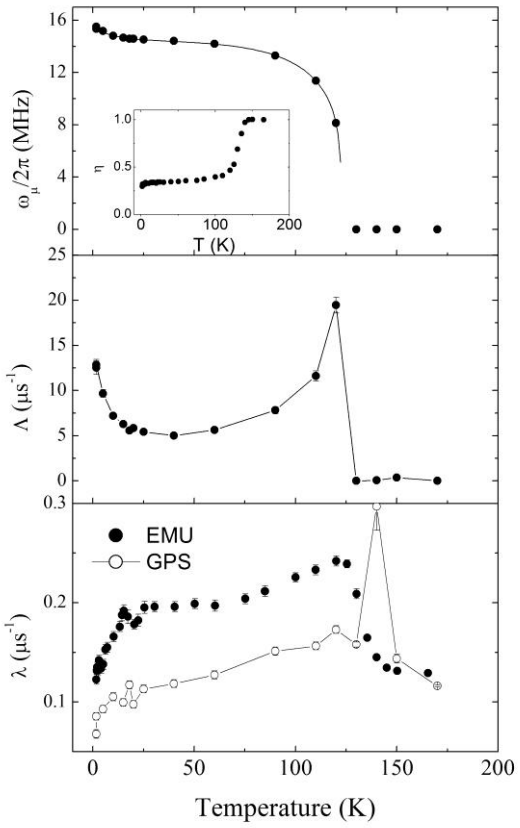

Figure 4.6. Temperature dependence of parameters extracted from fitting Eq 4.2 for Yb-227. TOP: $\omega_\mu/2\pi$ with η inset; the solid line is afit to Eq. 4.3 as described in the text. MIDDLE: Λ solid lines are guides for the eyes. BOTTOM: λ from both GPS and EMU.

Shown as the solid line in Figure 4.6, the extracted values f_0 = *14.1(2),* α = 4.3(6), and β = 0.23(5) are in reasonable agreement with those determined from the simple mean-field fit for Y-227, with T_N = 122(2) K. The last factor in Eq 4.3 describes contribution of the polarized Curie-like Yb^{3+} moments to the total magnetic field at the muon stopping site, with phenomenological parameters found to be C^* = 0.8(5) K and θ = -7.5(2) K, where θ is the Curie-Weiss temperature and C* depends on both the Yb^{3+} effective moment and the hyperfine coupling of the Yb^{3+} with the muon. The negative value of θ

indicates that the Yb^{3+} correlations are antiferromagnetic, and its magnitude suggests that ordering may occur at a low temperature; this is discussed further below.

We have also studied the ZF and LF depolarization on the EMU spectrometer at ISIS to exploit its sensitivity to slow muon depolarization processes. Oscillations observed on GPS lie above the bandwidth of the EMU detector and thus only the slow-relaxing components are observable. The resulting asymmetry curves can be described by a simple exponential function,

$$A(t) = A_S exp(-\lambda t) \qquad (4.4)$$

where A_S is the initial asymmetry and left as a fit parameter to account for the apparent loss of asymmetry due to the onset of oscillations. After correcting for background contributions and normalizing to full asymmetry, the low temperature value of A_S was found to be nearly identical to η as determined from data taken on GPS. Finally, as a test of our model proposed in Eq. 4.2 the longitudinal field dependence of A_S was measured for both samples at 1.8 K, as shown in Figure 4.7. For polycrystalline samples, the dynamic or longitudinal fraction of the total asymmetry (η or A_S) should vary as a function of applied longitudinal field as:

$$A = \frac{3}{4} - \frac{1}{4b^2} + \frac{(b^2-1)^2}{8b^3} \ln \left|\frac{b+1}{b-1}\right| \qquad (4.5)$$

with $b = \langle \boldsymbol{B_{loc}} \rangle / B_{ext}$, the ratio of the internal field to the applied external field [21]. Performing a fit of the data to Eq. 4.5, shown as the solid line in Figure 4.7 for Y-227, we find $\langle \boldsymbol{B_{loc}} \rangle$ = 950(200) G for Y-227 and 1130(150) G for Yb-227. These results are consistent with the values extracted from the low temperature muon spin precession

frequencies, and the good fit of the model to our data confirm that nearly 100% of the sample has uniform long-range ordering.

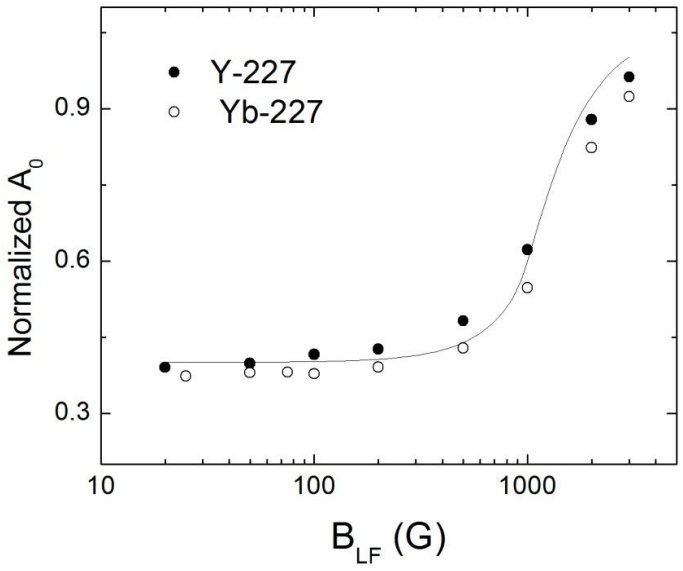

Figure 4.7. Field dependence of the initial asymmetry taken on the EMU spectrometer at 1.8 K for Y-227 and Yb-227. The solid line is the fit of Eq (4) to the Y-227 data.

Even more important, these values are consistent with the temperature evolution and magnitude of the local magnetic field obtained for Eu-227 by Zhao *et al* [5]. That such behavior is observed in all three insulating samples examined thus far is indicative of a single type of magnetic configuration across this part of the series. The similarity of the critical exponents obtained from our analysis, and later extracted later from Ref [5], is further evidence that the magnetic ordering transition is driven by the same mechanisms in all three systems, regardless of microscopic details such as the lattice parameter or presence of the magnetic moment on the A-site.

The temperature dependence of λ is shown in the lower panel of Figure 4.4 for Y-227 for both spectrometers. The rates are somewhat higher for data taken on EMU than GPS, and could either reflect the difficulty of measuring such small depolarization rates at continuous muon sources such as PSI and/or a very slight underestimation of the background signal in the ISIS data. However, we note these rates are 10^3 – 10^4 times smaller than Λ or ω, therefore such disagreement between spectrometers produces negligible error in describing the temperature dependence of the oscillatory component. A small increase in λ is observed beginning at 190 K in Y-227 and correlates with bifurcation of the magnetization. As λ represents depolarization primarily from dynamic mechanisms, this increase signifies a modification of the local fluctuation spectra which may arise from any number of mechanisms in this frustrated system, including a growing presence of short-range order as suggested to occur in other iridate compounds [22].

Although λ exhibits a slight peak near the onset of spontaneous oscillations, there is no sign of paramagnetic divergence as typical for slowing down of spin-lattice fluctuations near a transition to a magnetically ordered or glassy state. Below 150 K, λ shows only weak temperature dependence and is clearly non-zero at 1.5 K. Similar effects have been observed in many pyrochlore systems [23-25] and is known more generally as persistent spin dynamics (PSD). There considerable debate about the origin of this behavior, and include quantum diffusion between nearby muon stopping sites [26], quantum fluctuations of the magnetic moments [27] and or an unknown zero energy (gapless) mode contributing of the excitation spectra near zero energy [5], [28,29]. Our observations in Y-227 do not attempt to answer these questions, thus it is beyond the

scope of this work to comment further; I leave this debate instead as the proposed topic of future work in this system.

The qualitative behavior of λ is remarkably similar between Y-227 and Yb-227 as well as Eu-227 [5] near the onset of oscillations, indicating that the local magnetic field is not substantially altered by the presence of additional moments. For Yb-227, below T^* we observe a rather dramatic decrease of λ indicating substantial slowing down of fluctuations coinciding with the increase of the static local magnetic field. As a probe of this behavior, the longitudinal field dependence of λ was measured at 1.8 K in an applied magnetic field up to 3 kG. Shown in the inset of Figure 4.8, λ is well described by a modified Redfield formula which describes depolarization due to dynamic fluctuations with a single relaxation channel with characteristic correlation time $\tau_c >> (\gamma_\mu \Delta)^{-1}$ [14]

$$\lambda = \frac{\gamma^2 \Delta^2 \tau_c}{1+\omega\tau_c} + \lambda_0 \qquad (4.6)$$

where $\omega/\gamma_\mu = B_{ext}$, and Δ is the width of the field distribution of the fluctuating moments at the muon site. The constant λ_0 = 0.05(2) MHz is used here as a correction for other field independent relaxation channels. Fitting Eq. 4.6 to this field dependent data yields Δ = 20(2) G and τ_c = 1.0(5) x 10^{-9} s; this value of Δ indicates small variations of the local field relative to $\langle \boldsymbol{B_{loc}} \rangle$. The τ_c extracted from Eq. 4.6 has a characteristic temperature of $\hbar/k_B\tau_c \sim 7$ mK which in ordinary antiferromagnets should be close to the Neel temperature [30]. This implies then that either (1) there is a magnetic transition at roughly 7 mK, or (2) that the fluctuations do not follow the simple formalism for antiferromagnets or are not due to fluctuations of the AFM order parameter. The τ_c extracted for Yb-227 is 40 times larger than estimated for Eu-227 [5], however the low temperature values of the λ

are quite similar, and in fact appear to follow the same behavior near T_M; this implies that the low temperature depolarization is not due to thermal fluctuations of the ordered moments, but rather more likely stem from the same anomalous PSD that are observed in other pyrochlore samples.

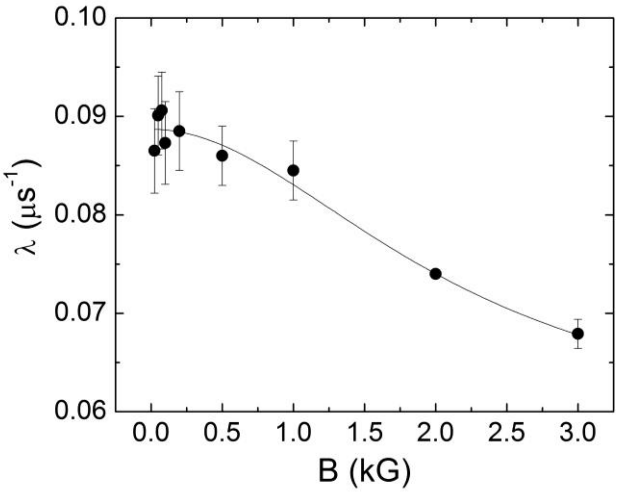

Figure 4.8 Field dependence of λ for $Yb_2Ir_2O_7$ taken from the EMU spectrometer at 1.8 K. The solid line represents the fit of Eq 4.6.

4.2.5 Low temperature results for $Yb_2Ir_2O_7$

The negative Curie-Weiss temperature (θ = -7.5 K) extracted from Eq. 4.3 suggests that the Yb^{3+} sublattice may undergo a separate transition to a long range ordered state at low temperature. To study this hypothesis, measurements of the zero-field muon precession frequency in Yb-227 were recently made down to 20 mK at the Low Temperature Facility (LTF) at PSI. To accurately measure the change in precession

frequency and field-broadening the long-time exponential decay (t > 1 μs) was first fit and subtracted from the total asymmetry curve and a Fourier transform was performed on the resulting spectra. By fitting the resulting peak to a Lorentzian, the central frequency and FWHM could then be determined systematically with less error than would result by fitting to Eq. 4.2 to the real-time data alone. It is found that the broadening of the precession frequency does not continue to increase as dramatically as indicated by the dramatic upturn in Λ, and levels off within error to the value obtained near 2 K. The temperature dependence of the central precession frequency is found to have non-monotonic behavior as shown in Figure 4.9, with a peak occurring at approximately 1.5 K. Also shown in the figure is the data taken from Figure 4.6 showing the overlap of the two data sets confirming that this is not a spurious result of the analysis technique.

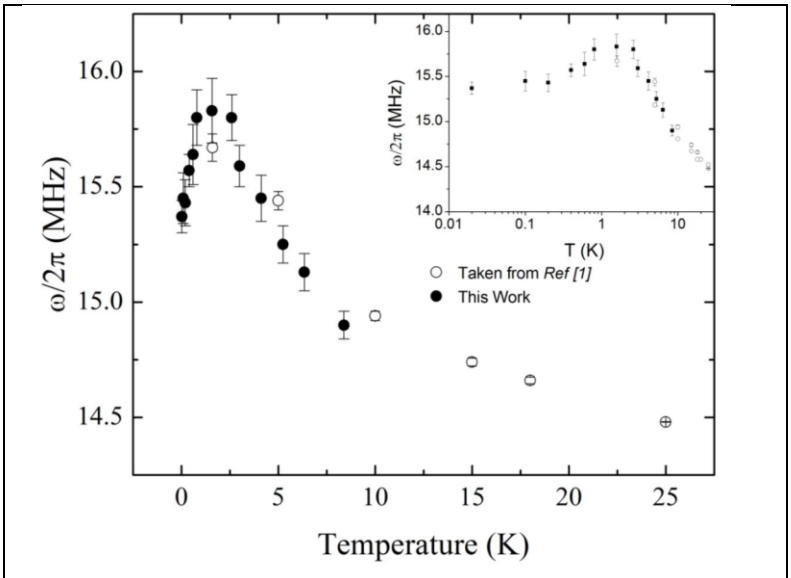

Figure 4.9 the low temperature precession frequency as a function of temperature in Yb-227. The open circles are data taken from Ref [20] while the closed circles are the result of more recent measurements which were extended to 20 mK. The same data is shown in the inset on a logarithmic scale.

The formation of such a peak means that the configuration of the Yb^{3+} moments act to produce a finite magnetic field at the muon stopping site which partially cancels that of the Ir sublattice. This occurs on the same order as the Curie-Weiss temperature extracted from the temperature dependence of the spontaneous precession frequency measurements above 2 K. A possible cause of this behavior is the onset of long-range order on the Yb^{3+} sublattice below ~ 1.5 K as occurs in *R*FeAsO compounds samples at low temperature [19]. We compare this to the situation occurring in the pyrochlore titanate $Yb_2Ti_2O_7$. Specific heat measurements of poly- and single- crystals indicate that a first order transition occurs in this compound at 250 mK, while an analysis of the mean-field Hamiltonian using exchange parameters extracted from inelastic neutron scattering predicts a second order phased transition should occur at ~ 3 K [31, 32]. Because of this it was assumed that the 250 mK transition was to a long-range ordered state with a reduced ordering temperature due to the frustration of the pyrochlore lattice. Recently, however a μSR investigation found no evidence of spontaneous oscillations down to 20 mK, indicating that there is no long-range ordered state at low temperatures [33]. Subsequent Knight shift measurements using transverse field μSR revealed Curie-Weiss behavior above 400 mK with an effective T_{CW} = -1.3 K. A marked transition away from this behavior was also found to occur at 250 mK due to a change in the local spin susceptibility or hyperfine coupling across the phase transition. As no long-range order occurs, this was taken as a signature of the formation of a more exotic type of spin liquid or spin ice state [32] which may exist on the pyrochlore lattice [34] and suggests a hidden-order symmetry reminiscent of URh_2Si_2 [35].

At low temperatures, we may consider the static field resulting from the ordered Ir moments in much the same way as the applied transverse field used in Ref [33]. The shift in the peak precession frequency in Yb-227 is thus due to an effective Knight shift arising from the muon coupling to the Yb ions, either through dipolar or hyperfine mechanisms. In this framework, we may interpret the deviation from Curie-Weiss behavior in much the same way, such that well below this temperature we have a significant change in the hyperfine spectra resulting from the entrance of a new spin state that lacks long-range order on the Yb-sublattice. Heat capacity and magnetization data are absolutely pertinent to determine the possible origins of this behavior and to further explore this comparison with the titanate compounds.

4.2.4 Magnetic Hysteresis Measurements of $Y_2Ir_2O_7$

The preceding measurements of the dc-susceptibility and μSR have shown that two distinct magnetic transitions exist in Y-227. We have observed that the dc magnetization anomaly at T_M = 190 K does not represent the onset of long range order as occurs in Yb-227 and Eu-227. Instead, long-range order is only observed below T_{LRO} = 150 K. To further investigate this unusual series of the transitions and the nature of the intermediate state, magnetization loops were measured in each of the important temperature regimes, shown in Figure 4.9. Great care was used to ensure each the zero field state was unbiased from previous measurements, therefore for each isothermal measurement the samples were warmed to T > 200 K and then cooled in zero field to the corresponding measurement temperature. Above T_M = 190 K simple paramagnetic

behavior is observed, while below T_M a narrow hysteresis with remnant moment ~ 1 x 10^{-3} μ_B/Ir^{4+} is found. At 2 K (well below T_{LRO}) the remnant moment has approximately doubled, while the coercive field has increased by more than an order of magnitude to nearly 10 kOe.

Shapiro *et al* also performed hysteresis measurements on polycrystalline samples of Y-227 [13]. They report magnetization with a very small coercive field and remnant moment of order 10^{-5} μ_B/Ir^{4+} which is much smaller than that which we observe; as an example, they presented data taken at T = 100 K < T_{LRO} which shows a linear dependence with field. They also report the onset of a small remnant moment at 190 K, above the bifurcation at 150 K they observe in their samples, which is consistent with our observation of a SRO state in the temperature range $T_{LRO} < T < T_M$. The quantitative rather than qualitative differences between their data and ours supports an extrinsic explanation, such as surface magnetism or domain wall boundaries due to variations in the crystallinity and grain size rather than an intrinsic mechanism such as canting of the Ir moments.

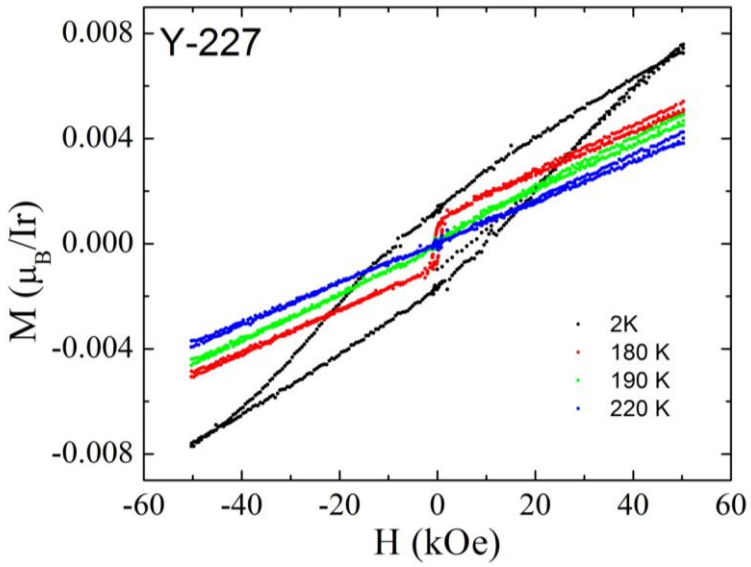

Figure 4.10 Magnetization versus field isotherms taken on Y-227

The remnant moment is a very small fraction of the expected magnetic moment for a localized Ir^{4+} therefore it is clear that the ordered phase is not of any ferromagnetic variety which would produce a much larger remnant moment. The net moment is either the result of a small degree of canting, as observed in other iridate structures [6,7] or from extrinsic mechanisms such as surface magnetism or domain wall effects as recently suggested for AIAO structures [36]. It should also be noted that a small paramagnetic-like contribution has been theorized to exist in AIAO structures based on the octupolar structure of the AIAO configuration, and may be related to the apparent linear 'background' magnetism [36]. This interesting feature of the theory may produce notable changes as the system passes through the boundary from SRO to LRO which warrants further study. Based on this, we can definitely say the long-range order is of the

antiferromagnetic type including AIAO. The curve taken at 180 K is in the intermediate region $T_{LRO} < T < T_M$ does have a finite remnant moment due to magnetic order, however the coercive field is extremely narrow which indicates a very small energy barrier to spin reversal. This suggests that in the intermediate region there exists either a clustered or glassy type state, in which small regions of magnetic order weakly interact via a paramagnetic matrix, or a state with short-range order lacks a global coherence but with a field distribution that does not cause rapid muon depolarization. Detailed measurements AC-susceptibility, which probes the frequency dependence of the spin-fluctuation spectra, will play a key role in deciphering the true nature of this unusual intermediate region [37].

4.3 Simulation of Muon Stopping Site and Dipole Field Calculations

The existence of long-range order of the Ir^{4+} moments in Y-227 and Yb-227 determined by μSR measurements is an important result as it has been reported previously only in Eu-227. To obtain more information about the magnetic structure from this measurement one must know what site the muon occupies in the lattice. Once this information is known, one can then calculate the magnetic field at the muon stopping site for different magnetic configurations, and compare with that extracted from experiment in order to determine the appropriate long-range structure. One can determine this information experimentally using single crystals which may be rotated to provide information about the symmetry of the muon stopping site [38]. One can also determine them if the material contains large nuclear moments which dominate the relaxation at high temperatures [39]. However, in general this is not possible for every material of

interest, and so one must resort to calculations of the electrostatic potential within a unit cell to find the most likely stopping site(s). This section will describe our attempts to calculate the possible stopping sites inside of Y-227 utilizing an electrostatic approximation. I will then calculate the local magnetic field at the muon site for several possible magnetic configurations based on our experimental μSR observations.

4.3.1 The Muon Stopping Site

The muon, being a positively charged particle will stop near the most electronegative ion in the lattice, particularly in the case of insulating oxides and fluorides. This typically results in the muon partially bonding to these ions at a distance of about 1 Å. A simplified approach to determine these sites utilizes a technique known as Ewald's method, which pre-dates even the vast acceptance of quantum mechanical approaches to solids. Although this lacks the accuracy of modern techniques, it can provide an adequate approximation in the case of ionic compounds which do not have free conduction electrons. A detailed explanation of this technique may be found elsewhere [40, 41], and I will now merely outline the important steps.

One of the main problems which this method addresses is that due to the long range nature of the Coulomb interaction, the number of ions which must be summed to reach a convergent answer often diverges meaning that the direct summation in real space is not possible [41]. By writing the troublesome $1/r$ in terms of error functions we find that the Coulomb potential for a test charge $q_j = 1$ is the sum of two terms:

$$\phi(r_j) = \sum_{i \neq j} \frac{q_i}{r_{ij}} = \sum_{i \neq j} \left[\frac{q_i \mathrm{erf}\,(\varepsilon r_{ij})}{r_{ij}} + \frac{q_i \mathrm{erfc}\,(\varepsilon r_{ij})}{r_{ij}} \right] \qquad (4.7)$$

where $r_{ij} = |r_i - r_j|$. The first term becomes a constant as $r \rightarrow 0$ but has a long range tail extending out as $r \rightarrow \infty$, while the second term vanishes quickly as $r \rightarrow \infty$ but becomes singular as $r \rightarrow 0$. The key to this problem is that the first term may be accurately represented by a sum over the first few terms in reciprocal space through a Fourier transformation, while the second term sums to a convergent value quickly in direct space. Performing this transformation of Eq. 4.7, the potential can thus be written as

$$\phi = \sum_{i \neq j} q_i q_j \left[\frac{4\pi}{\Omega} \sum_{K_m \neq 0} \frac{\exp\left(-\frac{|K_m|^2}{2\varepsilon^2}\right) \exp\left(-iK_m r_{ij}\right)}{|K_m|^2} + \sum_T \frac{\operatorname{erfc}\left(\varepsilon |r_{ij}+T|\right)}{|r_{ij}+T|} \right] - - \frac{\pi}{\Omega \eta} \qquad (4.8)$$

The first sum is over all reciprocal lattice vectors $\boldsymbol{K_M} \neq 0$, while the second is over all lattice vectors $\boldsymbol{T}$ which avoid self-energy contributions and the unit cell volume is given by Ω. The beauty of this approach is that each of these sums converge rapidly in its own space, that is, the sums may be taken only over the first few reciprocal lattice vectors and real-space unit cells without needing to extend the sums to infinity as occurs in the real space sum alone. The drawback is the presence of the free parameter ε may not be easily estimated from physical parameters such as ionic radii, however in general it is found that the exact value of this parameter does not make that great of a difference assuming a sufficiently large volume is used to begin with. Regardless, this approach allows for a good first approximation to the possible stopping sites suitable for the purposes herein.

We have taken this approach to calculate the muon stopping sites in Y-227 at low temperatures when the system is in a fully insulating state, and charges are well localized, thus meeting the ionic condition necessary for Ewald's approximation. The code for simulating the electrostatic potential over a single unit cell has been written using

MatLab and can be found in Appendix A2. The calculations were performed on the Scorpio Linux cluster at Boston College, with a typical run time of 3 to 4 days hours for a unit cell with a grid with spacing ~ 0.1Å.

The locations of all of the ions were determined for the the *Fd3m* space group (No. 227) taken from the International Table of Crystallography 2006 [42]. The value of the unit cell and free oxygen parameter 'x' were taken from the Rietveld refinement of our neutron diffraction data shown above. All atoms were taken to contain the full ionic charges, i.e. A^{3+}, Ir^{4+}, and O^{2-}. The results were not affected by the size of the distribution parameter ε over an order of magnitude between $1 < \varepsilon < 20$, therefore was set to 10. The first attempts at this calculation produced potential minima which were unreasonably close to the oxygen sites, well under the ~ 1 Å or so expected in real materials. Therefore, as done for the calculation of the stopping sites in $Y_2Mo_2O_7$ an additional exponential potential was added in an *ad-hoc* method to act as a hard-core repulsive term and push out the corresponding minima to a reasonable distance. Without an additional non-trivial normalization, this term distorts the overall charge conservation of Eq. 4.7, meaning that the numerical values of the depths of the potential minima which are calculated potential are probably underestimated.

The results of this calculation can be seen in Figure 4.11 which shows a detailed contour plot of electric potential for the x-y plane containing several global mimima of the potential. Here, I have indicated the lowest potential sites which do not lie at the center of an oxygen ion in red. The approximate locations, normalized to the unit cell length are [0.17, 0.63, 0.83] and [0.63, 0.17, 0.83]. The locations of the closest Y, Ir, and O atoms are shown for comparison. These are quite different from the muon-stopping

sites deduced by Dunsiger for the isostructural $Y_2Mo_2O_7$ also using Ewald's method to solve the electrostatic potential of the crystal [40], and by McClarty *et al.* [43] from experimentally measured muon rotation frequencies in insulating $Gd_2Sn_2O_7$ where the Palmers-Chaulker configuration was assumed for the ground state. The muon-stopping sites, normalized to the appropriate lattice parameter, were found to be [0.16, 0.16, -0.17] and [0.4402, 0.5005, 0.5625] for $Y_2Mo_2O_7$ and $Gd_2Sn_2O_7$, respectively. We note that while Dunsiger used a similar analysis, only data in the first quadrant centered at the origin (that is $x, y z$ = [$-a/4$, $+a/4$]) meaning that some of the sites which we observe may not have been captured.

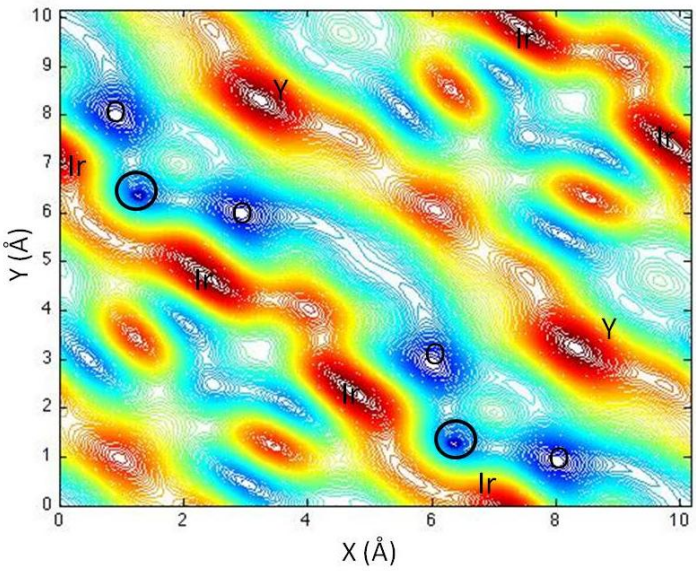

Figure 4.11 Contour plot of the electric potential at z = 0.83a (8.44 Å). The possible muon stopping sites lie on the black circles at a distance of ~ 1 Å from the nearest oxygen.

4.3.2 Dipole field Calculations

We now turn to the calculation of the magnetic field at the muon stopping sites. In general, the net field is a sum of the contributions from the local dipole moments, hyperfine interactions, Lorentz field (in ferromagnets) [44]. This may be greatly simplified in insulating antiferromagnetic systems such as Y-227 because the lack of conduction electrons at low temperature greatly reduces any hyperfine couplings, and the small bulk magnetization of the sample removes any effects demagnetization fields which lead to the Lorentz field becoming irrelevant [45]. Therefore, in calculating the field strength we need only to take into account the sum of the dipole moments at the stopping site.

The net dipole field $\boldsymbol{B}_{dip}$ at the muon site $\boldsymbol{r}_{\mu}$ is determined by the sum of the components of the field arising from all of the local moments; using a compact notation, the α-th component of the total dipole field (B^{α}_{dip}) be compactly written as a sum of the local moments $\boldsymbol{m_i}$ (with components m_i^{β}) via the following relationship:

$$B^{\alpha}_{dip}(\boldsymbol{r_{\mu}}) = \sum_{\boldsymbol{i}} D_i^{\alpha\beta}(\boldsymbol{r_{\mu}}) m_i^{\beta} \qquad (4.9)$$

where the sum is taken over all of the magnetic ions in the lattice, or as many as needed to achieve proper convergence, typically extending over a few unit cells in each direction. The dipole tensor $D_i^{\alpha\beta}(r_{\mu})$ in Eq. 4.9 relates the α-th component of the magnetic field at the muon site to the β-th component of the *i-th* magnetic moment, and is given by

$$D_i^{\alpha\beta} = \frac{\mu_0}{4\pi R_i^3}\left(\frac{3R_i^{\alpha}R_i^{\beta}}{R_i^2} - \delta^{\alpha\beta}\right) \qquad (4.10)$$

where $R_i = |\boldsymbol{r_{\mu}} - \boldsymbol{r_i}|$ is the distance between the muon site and the *i*-th magnetic moment and $\delta^{\alpha\beta}$ is the Kroneker delta function [BlundellDipole]. The difficulty then lies in

determining the appropriate representation of the magnetic configuration of interest in this formalism such that it may be easily summed over. By careful examination of the important symmetries of the crystal, this procedure has been done for several configurations suggested by Wan *et al* Y-227 [46]. These include the non-collinear all-in/all-out and the polarized 2-in/2-out configuration, two collinear ferromagnetic configurations aligned along either the (111) or the (100) directions (FM-(111) and FM-(100), respectively), and one co-planar state with orthogonal spins due to the indirect Dzyaloshinsky-Moriya interaction, or IDM. It is important to note here that the polarized 2I2O configuration is not the same as spin-ice: here the spin configuration is uniform for each tetrahedra, while spin-ice is actually a degenerate state made up of the superposition of the different possible polarized structures such that tetrahedra within a unit cell do not have the same identical configuration.

A MatLab program was written to perform this calculation, and can also be found in Appendix A1. For these simulations, the Ir^{4+}moment was chosen to be 1 μ_B which is higher than the estimated moment based on our neutron diffraction results; however it represents the largest value for a $j = 1/2$ Ir^{4+} and will therefore serve as a upper bound for the following results. From Eq. 4.9 we see that the net magnetic field is proportional to the magnitude of the local moments, so the total field may simply be scaled proportionally if a smaller moment is desired. These calculations have been performed for the sites which we have calculated based on our Ewald summation technique, as well as those reported by Dunsigner, McClarty mentioned above. The magnitude of the local field calculated for each configuration is listed in Table 4.1. For all three sites, we find that the non-collinear and FM-(111) configurations overestimate the size of the magnetic

field relative to that measured by ZF-μSR, while the co-planar IDM and FM-(100) configuration underestimate this value by a significant amount. As these values represent the upper bound of the local magnetic field we can rule out the IDM and FM-(100) as the correct ground state configurations. However, we are unable at this time to distinguish between non-collinear sites and FM-(111) configurations based on the imprecision in the determined muon stopping-site.

	all-in/all-out	2-in/2-out	FM-(111)	FM-(100)	IDM
Dunsiger	1400 (200)	730 (200)	1310 (100) G	1210 (100)	300 (100)
McClarty	640 (100)	550 (100)	1120 (100) G	800 (100)	620 (50)
[0.17 0.63 0.83]	3300 (100)	1450	1900	2800	680
[0.63 0.17 0.83]	3300 (100)	1550	1900	3170	680

TABLE 4.1. The resultant field at four possible muon-stopping sites for various configurations of the Ir^{4+} sublattice as described in the text assuming a 1 μ_B local moment. All fields are given in units of G.

I have also computed the magnetic field over the entire unit cell for the AIAO and 2I2O configuration using a similar approach to determine the spatial variation of the local field which is important to consider for inaccuracies of the stopping site. A contour plot of the magnetic field in the same plane shown in Figure 4.11 is shown below in Figure 4.12. From this I find that the local field varies dramatically depending upon the direction, for example it is found to reach ~1 T as distance from the nearest Ir ion approaches 1 Å, while it is found to be less than 100 G for the region well removed from any moments. However, for small displacements on the order of the grid spacing (0.1 Å) the maximum difference is on the order of 100 G.

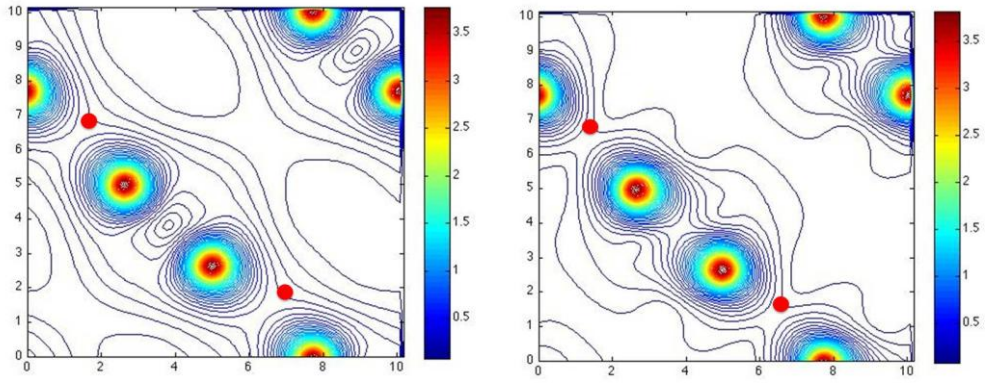

Figure 4.12 Dipole field contour map in the x-y plane z = 0.83*a* for (a) All-in/All-out configuration and (b) 2-in/2-out configuration. The approximate locations of the muon stopping site as determined by Ewalds's method are indicated by the red markers. The magnetic field in each panel is in units of Tesla.

As mentioned above, I have used the polarized 2I2O for simplicity, this of course is not the appropriate ground state to use if one suspects true spin-ice. μSR studies involving true spin-ice compounds such as $Dy_2Ti_2O_7$ and $Ho_2Ti_2O_7$ [47, 48] have yet to provide any evidence of spontaneous oscillations which would indicate commensurate order of the type indicated in the above of calculations. Ideally, one would need to simulate the above results for many different configurations which obey spin-ice rules, then average the resulting distributions accordingly to compare with real results taken from experiments. Therefore, while I have used this state, it is more as an academic exercise than one which should be used to directly compare with the field extracted from our measurements.

These calculations were performed for the overestimated 1 μ_B/Ir; if we instead consider a more realistic estimate moment for Ir^{4+} of 1/3 μ_B/Ir, then from Table 4.1 we

find that the local field at the stopping sites calculated in this work should actually be 1/3*(3300 G) = 1100 G, which is exactly the value extracted from our measurements. Further study is needed to confirm these stopping sites, however by assuming these are even approximately correct this appears to conclusively prove the existence of the AIAO state as all of the other calculated states are far too small. This is consistent with the growing body of experimental [49] and theoretical work [46, 50] which suggests the AIAO ground state is the most likely candidate for the ground state in the insulating pyrochlore iridates.

4.3.3 Bayesian Approach

The previous calculations have shown that our μSR measurements are consistent with the AIAO structure, based on the field estimated at a few selected points in the unit cell, and assuming an overestimated moment on the Ir-site. A different question one may ask is that given the magnetic configuration, can I extract any other useful information about the moments themselves? For example, while we have limitations on the expected size of the Ir moment based on the resolution of current neutron scattering detectors, we do not know currently how large the Ir moment actually is in any of these compounds; it would be extremely helpful then if using a combination of simulation and our knowledge of the local magnetic field, we were able to extract more information about the size of this moment. To do so, we may take advantage of simple yet extremely powerful procedure based on Bayes Theorem which will allow us to determine the probability of the that the Ir (or any other ion we choose) has a moment of size *m* given

that we have a local field of size *B*. This can be written as the joint probability *P(m|B),* which is effectively the inverse of that calculated above in section 4.3.2 which would be the probability of finding a field *B* given the moment of size *m* or *P(B|m)*. This procedure is outlined in great detail in Ref [51], but essentially follows the relation shown in Eq. 4.10:

$$P(m \mid B) = \frac{P(m)P(B \mid m)}{P(m)} \qquad (4.10)$$

Rather than assume any single muon-stopping site as in the previous analysis, I have chosen to use ten thousand randomly generated sites that lie between 0.9 and 1.1 Å away from any of the oxygen atoms, ensuring that the minimum Ir-muon distance is greater than 1 Å. An AIAO configuration will then be used to calculate the dipole magnetic field at these sites to produce *P*(*B*|*m)* as a function of the Ir moment. Equation 4.10 is then used with the local field extracted from our μSR measurements at 1.6 K to invert this function in order generate the new joint probability *P(m|B)*. The MatLab code written to perform this simulation and analysis can be found in Appendix A1.

The result of this calculation are shown in Figure 4.13; we find several interesting features including a van Hove-like singularity near 0.25 μ_B/Ir with small spectral tail extending to 0.6 μ_B/Ir or so, as well as another region of non-zero probability centered at 1.75 μ_B/Ir. The latter of these is far too large to be considered as a possibility for the actual size of the moment, and therefore is due to a number of simulated muon stopping sites which lie much farther away from the Ir site than the actual stopping site. Ignoring this spurious affect, I find a strong probability that the Ir^{4+} ions have a moment between

0.25-0.35 μ_B/Ir, exactly as expected from estimates by Shapiro *et al* and just below what is observable from our neutron scattering results for $Q = 0$ modes consistent with the AIAO structure. This is also consistent with conclusions extracted from the analysis of the magnetic field at the stopping sites determined by Ewald's method in sections 4.3.2. In order to rule out other structures using this analysis, the probability distributions should be calculated for many different configurations in hopes that they yield moments which are either unreasonably large or small.

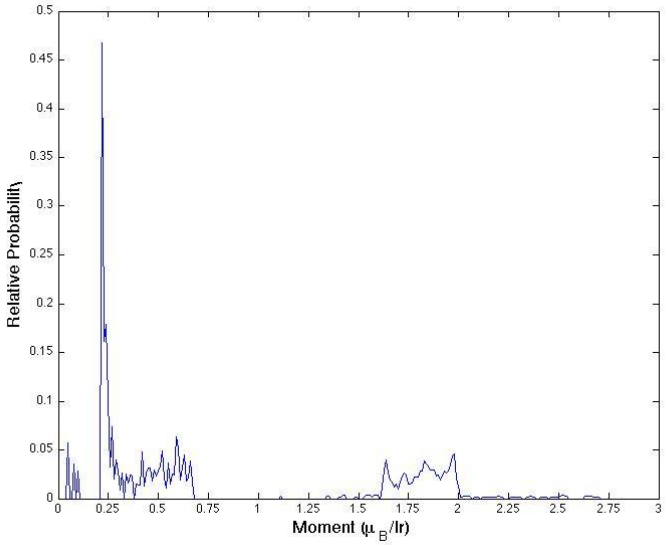

Figure 4.13 Probability distribution *P(m|B)* for the magnitude of the Ir^{4+} moments assuming an AIAO structure.

4.4 Discussion

In this chapter I have presented results from numerous measurements of two members of the pyrochlore iridates series, Y-227 and Yb-227. One of the first conclusions that become apparent from this work is that no single measurement is capable of fully determining precisely the nature of the magnetic state at any given temperature in either sample. From Section 4.2 we found that measurements of the bulk magnetization clearly show a transition to a magnetic state at low temperatures based on the bifurcation of the magnetic susceptibility at T_M = 190 K in Y-227 and 130 K in Yb-227, and hysteretic behavior of the magnetization in Y-227. We cannot distinguish based on this alone whether the low temperature is a spin-glass [2, 8, 20] or actual AFM order with some kind of canting or surface effects [36]. Elastic neutron scattering measurements also cannot prove the existence of a long-range ordered state in part due to the strong action of Ir as a neutron absorber, but can put limits on the size of the moments if order does occur, and even more importantly can rule out structural deformations as the cause of the order [13, 20]. Our μSR measurements presented in section 4.3 have so far been the only probe to conclusively prove that commensurate long-range order does exist in the Ir^{4+} sublattice below T_{LRO} = 150 K and 130 K for Y-227 and Yb-227.

While this order was observed before in similar μSR measurements of Eu-227 [5], it was unknown before this work if such order exists for other compounds, and how the configuration may evolve as the structure is distorted and magnetic rare earth elements are included. One of the primary results of this work has been our μSR measurements which have clearly shown for the first time that commensurate long-range order occurs on the Ir^{4+} sublattice in these compounds as well, regardless of lattice parameter or

presence of the rare earth moment on Yb. Furthermore, the structure of these two and Eu-227 appears to be identical, meaning that the driving exchange or correlations interactions which drive the insulating state do not differ greatly between Yb and Eu, the two extremes of the insulating region.

Before this work, several groups had speculated based on theoretically calculated phase diagrams [46, 50] that the magnetic order on the Ir-sublattice is of the non-coplanar type, such as the AIAO or 2I2O, however no concrete experimental proof existed before this work. Unfortunately, the lack of any signature of long-range ordering from neutron scattering measurements in Y-227 combined with recent studies of other frustrated Ir-based compounds [23] suggests that the large absorption cross section of the Ir-nuclei and inherently small ordered moments prevent the observation of any spin order in polycrystalline samples. These results, or rather lack thereof, were confirmed by independent magnetization and neutron scattering measurements on polycrystalline samples of Y-227 by Shapiro, *et al* in Ref [13]. In that work they noted that the estimated moment should be on the order of 1/3 μ_B based on the projection of the orbital component of the angular momentum onto the t_{2g}. This is near the limit detectable for $Q \neq 0$ modes, but just below that for $Q = 0$ modes. Currently, single crystals that have been grown by both our group and others are far too small to be used for neutron studies, even if they are combined to form a mosaic array. Therefore it is unlikely that such studies will be able to provide more information on the magnetic structure of these materials in the near future.

Numerical simulations were used to gain more information about the configuration of the magnetic moments based on our μSR results, the only conclusive measurements of long-range order thus far. Several likely muon stopping sites were

found in Y-227 using calculations of the electrostatic potential in 4.3.2; these were not the same as those determined previously for $Y_2Mo_2O_7$ and $Gd_2Ti_2O_7$ which indicates that the changes in the crystalline structure does have a significant impact on the location of the potential minima in this complex unit cell. More importantly, simulating the dipole field at these selected sites rules out many of the different $Q = 0$ modes suggested by previous theoretical works [46] indicating that the AIAO is the most likely candidate state. If the muon stopping sites can be verified either experimentally or with higher resolution simulations over smaller regions of the unit cell, then this will be the first conclusive evidence for this configuration. Other measurements presented in this work have corroborated this conclusions, for example the magnetic hysteresis in Y-227 have ruled out the presence of ferromagnetism as a possible ground state. Furthermore, the 2I2O is nominally degenerate and does not contain a global order from unit cell to unit cell, such disparity in magnetic field from stopping site to stopping site would induce rapid muon depolarization, which is in fact exactly what is observed in studies of the spin-ice compounds $Dy_2Ti_2O_7$ [48].

I compare these results to those obtained recently by resonant x-ray scattering techniques (RXS) which have recently been used to study the electronic and magnetic structure of these materials. Most recently, Sagayama *et al* utilized resonant diffraction at the L_3 edge to probe the magnetic structure single crystals of the insulating Eu-227 compound [49]. Resonant scattering peaks found at locations forbidden by nuclear structures alone gave evidence for the existence of long-range order in this compound with a $Q = 0$ configurations. From a careful analysis of the possible symmetry groups for the different possible configurations of they determined that the magnetic lattice retains

the face-centered-cubic structure of the crystal lattice below the transition indicating the AIAO magnetic order is the most likely candidate [49].

Our measurements have shown that our polycrystalline samples of Y-227 and Yb-227 are insulators with ground states driven by the electron localization as seen from VRH behavior below T_{LRO}. Comparison with single crystals of Eu-227 indicate that this is not a stoichiometric effect, and in fact consistent with the idea that the low temperature conduction and magnetization of these materials is determined by correlations of the *5d* electrons in the relatively narrow $j = ½$ band. Spectroscopic measurements using inelastic x-ray techniques on Y-227 and Eu-227 were also recently performed to investigate how the band structure changes as the lattice parameters vary as one moves across the series. In that work, they were able to show that 3 absorption lines exist which correspond to a lower-lying t_{2g} manifold which is split into $j = 3/2$ and ½ states, and an e_g state which lies several eV above [52]. Extensive DFT calculations were used to compare these results to the effects of the non-cubic crystal field term arising from the hexagonal arrangement of the A^{3+} surrounding each Ir^{4+} versus distortion of the local oxygen octahedra due to a non-ideal *x* parameter. However, because of the relatively poor resolution (FWHM ~ 300 meV) of the x-ray beam it is difficult to say with certainty which of the two is actually the more likely cause. These methods cannot determine any information about transitions between $j = ½$ levels which are necessary to gain information on the relative importance of the structural distortions compared to the correlations and spin-orbit interactions [Hozoi]. With improved resolution, future measurements should be able to measure parts of the magnon dispersion recently calculated [53] which would conclusively indicate the

proper ground state, and yield a great deal of information about excitation channels in these materials.

I next turn to the unusual behavior of Y-227; the onset of strong magnetism near 190 K in bulk susceptibility together with lack of spontaneous oscillations in ZF-μSR indicates that there is no long-range order at this transition. This is also not a transition to a traditional spin-glass state as in the isomorphic pyrochlore $Y_2Mo_2O_7$ [40, 25], since there is no divergence in the longitudinal relaxation rate λ characteristic of a critical slowing down of fluctuating moments at temperatures just above the freezing temperature. This existence of an unusual magnetically disordered phase near T_M is in contrast to the behavior observed for Yb-227, which exhibits a comparatively simple transition from paramagnetic behavior to long-range order with no intermediate phase. As we will see in the next chapter, Nd-227 also exhibits the intermediate lacking long-range order over a much larger temperature region [54], from which we conclude that the formation of the frustrated or short-ranged ordered state and its stability against transition to long-range order is closely associated with *A*-site radii R_A, as $R_{Yb} < R_Y < R_{Nd}$. It has been suggested separately that variations of the lattice parameter affect not only the conduction bandwidth, but also correlation and Ir-Ir exchange energy [55, 50, 46; 56, 57], both of which in turn determine transport properties and ground state configuration. We propose that competition between these parameters as determined by the *A*-site radii lead to the glassy/short-range ordered phase for a finite range of relative energy scales. It would be of great interest therefore to continue these comprehensive measurements for the remainder of the rare-earth series to verify this prediction and gain further insight into this mechanism.

4.5 Conclusions

In summary, we observe long-range order in both Y-227 and Yb-227 which is likely the same for all insulating phases Furthermore, we report an unusual disordered precursor spin phase in Y-227 which suggests that bifurcation, metal-insulator, and long-range ordering need not occur at the same temperature as previously reported. Our results support the predictions that correlation strength can be controlled by choice of *A*-site element and has direct consequences on the magnetic structure, including the stabilization of an intermediate glassy or short-range ordered phase in Y-227 as observed in Nd-227. While these observations have provided significant insight into the underlying complexity of these materials, fabrication of large volume, high-quality single crystals is still necessary for the conclusive determination of the magnetic structure. Comprehensive studies of the remaining members of the iridate family are vital to answering the remaining questions and to assist with the development of future theoretical models.

Chapter 4 References

[1] D. Yanagishima and Y. Maeno, J. Phys. Soc. Jpn. **70**, 2880 (2001).

[2] N. Taira, M. Wakeshima, and Y. Hinatsu, J. Phys.: Condens. Matter **13**, 5527 (2001).

[3] S. Nakatsuji, Y. Machida, Y. Maeno, T. Tayama, T. Sakakibara, J. van Duijn, L. Balicas, J. N. Millican, R. T. Macaluso, and J. Y. Chan, Phys. Rev. Lett. **96**, 087204 (2006).

[4] D. E. MacLaughlin, Y. Ohta, Y. Machida, S. Nakatsuji, G. M. Luke, K. Ishida, R. H. Heffner, Lei Shu, and O. O. Bernal, Physica B **404**, 667 (2008).

[5] S. Zhao, J. M. Mackie, D. E. MacLaughlin, O. O. Bernal, J. J. Ishikawa, Y. Ohta, and S. Nakatsuji, Phys. Rev. B **83**, 180402(R) (2011).

[6] Chetan Dhital, Sovit Khadka, Z. Yamani, Clarina de la Cruz, T. C. Hogan, S. M. Disseler, Mani Pokharel, K. C. Lukas, Wei Tian, C. P. Opeil, Ziqiang Wang, Stephen D. Wilson, Phys. Rev. B **86** 100401(R) (2012).

[7] Chetan Dhital, Tom Hogan, Z. Yamani, Clarina de la Cruz, Xiang Chen, Sovit Khadka1, Zhensong Ren, and Stephen D. Wilson. Phys. Rev. B **87**, 144405 (2013).

[8] K. Matsuhira, M. Wakeshima, Y. Hinatsu, and S. Takagi, J. Phys. Soc. Jpn. 80 094701 (2011).

[9] J. S. Gardner, M J. P Gingras J. E. Greedan, Rev. Mod. Phys **82**, 52 (2010).

[10] N. F Mott *Phil. Mag.* **19**: 835. (1969).

[11] Jun J. Ishikawa, Eoin C. T. O'Farrell, and Satoru Nakatsuji, Phys. Rev. B **85**, 245109 (2012).

[12] K. A. Ross, Th. Proffen, H. A. Dabkowska, J. A. Quilliam, L. R. Yaraskavitch, J. B. Kycia, and B. D. Gaulin, Phys. Rev. B **86**, 174424 (2012).

[13] M. C. Shapiro, S. C. Riggs, M. B. Stone, C. R. de la Cruz, S. Chi, A. A. Podlesnyak, and I. R. Fisher, Phys. Rev. B 85, 214434 (2012).

[14] A. Yaouanc and P. Dalmas de Réotier *Muon Spin Rotation, Relaxation, and Resonance : Applications to Condensed Matter*, (Oxford University Press, Oxford, 2011).

[15] T. M. Riseman and E. M Forgan, Physica B **326** 226 (2003).

[16] C. Domb, *The Critical Point* (Taylor and Francis, Bristol PA, 1996).

[17] R. Kubo, Phys. Rev. **87**, 4568 (1952).

[18] P. Parruccini, Phys. Rev. B **68**, 104415 (2003).

[19] H. Maeter, H. Luetkens, Yu. G. Pashkevich, A. Kwadrin, R. Khasanov, A. Amato, A. A. Gusev, K. V. Lamonova, D. A. Chervinskii, R. Klingeler, C. Hess, G. Behr, B. Büchner, and H.-H. Klauss, Phys. Rev. B **80**, 094524 (2009).

[20] S. M. Disseler, Chetan Dhital, A. Amato, S. R. Giblin, Clarina de la Cruz, Stephen D. Wilson, and M. J. Graf, Phys. Rev. B **86**, 014428 (2012).

[21] F. Pratt, J. Phys.: Condens. Matter **19,** 456207 (2007).

[22] S. Fujiyama, H. Ohsumi, T. Komesu, J. Matsuno, B.J. Kim, M. Takata, T. Arima, and H. Takagi. Phys. Rev. Lett. **108** 247212 (2012).

[23] O. Ofer, A. Keren, C. Baines, J. Phys. Cond. Matter **19** 145270 (2007).

[24] D. E. MacLaughlin, M. S. Rose, J. E. Anderson, Lei Shu, R. H. Heffner, T. Kimura, G. D. Morris, O. O. Bernal. Physica B **374** 142 (2006).

[25] S. R. Dunsiger, R. F. Kiefl, J. A. Chakhalian, J. E. Greedan, W. A. MacFarlane, R. I. Miller, G. D. Morris, A. N. Price, N. P. Raju, and J. E. Sonier. Phys. Rev. B **73**, 172418 (2006).

[26] P. Quémerais, P. McClarty, and R. Moessner, Phys. Rev. Lett. **109**, 127601 (2012).

[27] Shigeki Onoda and Yoichi Tanaka, Phys. Rev. B **83**, 094411 (2011).

[28] S. Dunsiger, R. Kiefl, K. Chow, B. Gaulin, M Gingras, J. Greedan, A. Keren, K. Kojima, G. Luke, W. MacFarlane, N. Raju, and J. Sonier, Phys. Rev. B **54**, 9019 (1996).

[29] O. Ofer, A. Keren, J. Gardner, Y. Ren, and W. MacFarlane, Phys. Rev. B **82**, 092403 (2010).

[30] T. Moriya, Progr. Theoret. Phys. **16**, 23 (1956).

[31] K. A. Ross, J. P. C. Ruff, C. P. Adams, J. S. Gardner, H. A. Dabkowska, Y. Qiu, J. R. D. Copley, and B. D. Gaulin, Phys. Rev. Lett. 103, 227202 (2009).

[32] Kate A. Ross, Lucile Savary, Bruce D. Gaulin, and Leon Balents, Phys. Rev. X **1**, 021002 (2011).

[33] R. M. D'Ortenzio, H. A. Dabkowska, S. R. Dunsiger, B. D. Gaulin, M. J. P. Gingras, T. Goko, J. B. Kycia, L. Liu, T. Medina, T. J. Munsie, D. Pomaranski, K. A. Ross, Y. J. Uemura, T. J. Williams, and G. M. Luke. ArXiv 1303.3850 (2013).

[34] L. Savary and L. Balents, Phys. Rev. Lett. **108**, 037202 (2012).

[35] J. A. Mydosh, and P M. oppeneer. Mod Phys. Rev. **83** (2011).

[36] T. Arima, J. Phys. Soc. Jpn. **28**, 013705 (2013).

[37] J. A. Mydosh, *Spin Glasses: An Experimental Introduction* (Taylor and Francis, London, 1993).

[38] M. C. Guidi, G. allodi, R. De Renzi, G. guidi, M. Hennion, L. Pinsard, A. Amato., Phys. Rev. B **64** 064414 (2001.

[39] G.J Nieuwenhuys, N.G Patil, H Noijons, D.G Tomuta, D.E MacLaughlin, R.H Heffnerc, A Amato. Physcia B **289** 228 (2000).

[40] S. R. Dunsiger, Ph.D. thesis, University of British Columbia, 2000.

[41] T. Schlick, *Molecular Modeling and Simulation: an Inerdisciplinary Guide* (Springer, New York NY 2002)

[42] ed. T. Hahn, International Tables for Crystallography, Volume A (Springer Norwell MA, 2005).

[43] P. A. McLarty, J. N. Cosman, A. G. Del Maestro, and M. J. P. Gingras, J. Phys. Cond Matter **23**, 164216 (2011).

[44] A. Schenk, *Muon Spin Rotation Spectroscopy: Principles and Applications in Solid State Physics* (Bristol, Boston 1985).

[45] S. J. Blundell, Physica B **404** 581 (2009)

[46] X. Wan, A. M. Turner, A. Vishwanath, and S. Y. Savrasov, Phys. Rev. B **83**, 205101 (2011).

[47] R. Aldus, S.T. Bramwell, S. Calder, T. Fennell, S.R. Giblin, and D. Prabhakaran. Nature **461** 956 (2009).

[48] S. R. Dunsiger, A. A. Aczel, C. Arguello, H. Dabkowska, A. Dabkowski, M.-H. Du, T. Goko, B. Javanparast, T. Lin, F. L. Ning, H. M. L. Noad, D. J. Singh, T. J. Williams, Y. J. Uemura, M. J. P. Gingras, and G. M. Luke, Phys. Rev. Lett. **107**, 207207 (2011).

[49] H. Sagayama, D. Uematsu, T. Arima, K. Sugimoto, J. J. Ishikawa, E. O'Farrell, and S. Nakatsuji. Phys. Rev. B **87** 100403(R) (2013).

[50] W. Wilcezk-Krempa and Y. B. Kim, Phys. Rev. B **85** 045124 (2012).

[51] S. J. Blundell, A. J. Steele, t. Lancaster, J. D. Wright, F. L. Pratt. Physics Procedia **30** 113 (2012).

[52] Liviu Hozoi, H. Gretarsson, J. P. Clancy, B.-G. Jeon, B. Lee, K. H. Kim, V. Yushankhai, Peter Fulde, Young-June Kim, and Jeroen van den Brink, ArXiv 1212.4009 (2012).

[53] E. K. Lee, A. Bhatacharjee, Y. B. Kim, AriXiv 1210.5242 (2012).

[54] S. M. Disseler, C. Dhital, A. Amato, C. Baines, S. Giblin, S. D. Wilson, C. R. de la Cruz, and M. J. Graf, Phys. Rev. **B** 85, 174441 (2012).

[55] D. Pesin and L. Balents, Nature Physics **6**, 376 (2010).

[56] M. Sakata, T. Kagayama, K. Shimizu, K. Matsuhira, S. Takagi, M. Wakeshima, and Y. Hinatsu, Phys. Rev. B **83**, 041102(R) (2011).

[57] F. F. Tafti, J. J. Ishikawa, A. McCollam, S. Nakatsuji, and S. R. Julian, Phys. Rev. B **85** 205104 (2012).

Chapter 5: Investigations of the Magnetic Structure of $Nd_2Ir_2O_7$

In the previous chapter I presented results for the two compounds with small A-site radii such that they were found to be insulating and magnetically ordered. $Nd_2Ir_2O_7$ (Nd-227) on the other hand, has a much larger A-site radius that places the compound on the border of metallic behavior and should therefore be an excellent place to begin probing for the novel exotic states proposed to exist in the series, as well as understand the formation of the unusual chiral spin-liquid suggested to exist in the metallic $Pr_2Ir_2O_7$ (Pr-227). In the first part of this chapter, I will present results from magnetization, resistivity muon spin relaxation measurements of polycrystalline Nd-227. The latter half of the chapter will be devoted to exploring measurements of the unusual hysteresis observed in field dependent magnetization, Hall effect and magnetocaloric effect of this compound. Together these results demonstrate the unusual characteristics of this material which makes it an intermediary between the metallic unordered Pr-227 and the remainder of the series which is insulating and magnetically ordered. The last portion of the chapter will examine the role of mobile charge carriers in the system through a study of calcium-substitution on the magnetic and electronic properties of Nd-227. Much of this chapter is based on the articles "Magnetic order and the electronic ground state in the pyrochlore iridate $Nd_2Ir_2O_7$" by S. M. Disseler, et. al., Phys. Rev. B **85**, 174441 (2012) [1] and "Magnetization and Hall effect studies on the pyrochlore iridate $Nd_2Ir_2O_7$" by S. M. Disseler et al., Phys. Rev. B **87**, 060403 (2013) [2]; the Ca-substitution work is ongoing.

5.1 Introduction

Much of the focus on the pyrochlore iridates from the theoretical community stems from early predictions for novel topological states of matter such as the Weyl semimetal and axion insulator phases [3-5]. As described previously, compounds with small A-site radii are Mott-like insulators [6, 7], while the largest A-sites Pr and Bi [8, 9] have unusual metallic ground states. The transition to one of the predicted exotic states is likely occurs between these two extremes by tuning the A-site ionic radius which should adjust relative effects of electron correlations to spin-orbit interactions [3,4]. Because of this, the most likely places to look for such interesting states should be in the cross-over region in which the ground state evolves from metallic to insulating, which occurs between $A = Eu$ and $A = Pr$ in the series. A number of recent studies on one compound which lies within this region, $Nd_2Ir_2O_7$ (Nd-227), have shown that the electronic ground state in this material is a delicate balance between sample stoichiometry and other extrinsic factors, and the precarious nature of the insulating state is evidenced by the variability in previously observed properties: initial reports by Yanagishima et al. showed Nd-227 was clearly metallic at all temperatures [10], whereas in later studies by Matsuhira et al. a MI transition was reported at 37 K [11]. Subsequent studies of the resistivity under pressure [12] revealed a small upturn in the resistivity below 20 K - interpreted as the onset of the MI transition - which was suppressed under an increased pressure of 10 GPa. At these higher pressures, a small resistive anomaly was observed near T = 3.3 K that was associated with the onset of magnetic order via an RKKY interaction facilitated by the suppression of the MI transition. Together, these support a developing picture of Nd-227 residing either very close to or just inside the boundary of

correlated, insulating behavior and suggest close proximity to the Weyl semimetal phase transition line. Studies of the intrinsic behavior of the Nd-227 ground state are thus an important metric for exploring the viability of the proposed topological phase diagram in the pyrochlore iridates and for exploring Nd-227's capacity for being tuned into the Weyl semimetal phase.

The presence of long-range magnetic order associated with this compound has also been disputed in recent years; it was initially presumed to be ferromagnetic based on the detailed magnetic response of the resistivity under pressure, with a 2-in/2-out structure of the Nd^{3+} (J = 9/2) moments [12]. However, recent neutron scattering measurements reported by Tomiyasu *et al* suggest that magnetic may also order occur at ambient pressure with long-range magnetic order on both Ir and Nd sublattices, with order of the Ir occurring below 33 K and of the Nd below 15 K ,both with an all-in/all-out arrangement [13]. As the Ir magnetic order cannot be observed directly, this result was inferred from the formation of a finite energy splitting between the lowest lying Nd doublet which was itself extracted from variation in the peak height of a single peak. Furthermore, because of the proximity to the large difference between the reported MI transition temperature in Nd-227 and the remainder of the series may arise by numerous mechanisms, especially given the relatively strong coupling of the Nd and Ir moments suggestive of additional interactions relevant in the ground state of this material.

In order to explore the relationship between the possible correlated spin order and the dynamics of mobile charge carriers in this material, we undertook a combined magnetization, electron transport, neutron diffraction, and muon spin relaxation/rotation (μSR) study on polycrystalline samples of Nd-227. In addition, we have begun isolating

the role of charge carriers through hole-doping the parent compound using calcium substitution. By leveraging both bulk and local probes on these samples, we gain a more complete picture of the complex magnetic states which form in this compound and how it can be used to discuss the evolution of magnetism and electron correlations in the entire pyrochlore iridate system.

5.2 Results: Resistivity, Susceptibility, and μSR

5.2.1 Synthesis and Characterization

Polycrystalline samples of Nd-227 were synthesized using the same solid-state techniques used to fabricate Yb-227 and Y-227. The samples were determined to be phase-pure with the exception of two minor impurity phases of IrO_2 and Nd_2O_3 each comprising less than 1% of the total volume fraction. Neutron experiments were performed on the HB-2A powder diffractometer at the High Flux Isotope Reactor at Oak Ridge National Lab and on the HRPD instrument at the ISIS spallation neutron facility. The resulting neutron diffraction patterns were refined using the *Fd-3m* cubic space group, and the lattice parameters were determined to be a = 10.3588(4) at 4 K and a = 10.3647(9) at 200 K with an O 48f parameter x/a = 0.3525, which did not vary appreciably over the temperature range.

Magnetization measurements were performed in an Oxford MagLab dc-extraction magnetometer while electrical resistivity was measured using standard AC four-probe techniques in gas flow and 3He cryostats with a 9T magnet as described in Chapter 3. Magnetic fields were applied parallel to the current, and the excitation level was varied at

several temperatures to ensure no self-heating occurred. Muon spin relaxation (μSR) measurements were carried out over the temperature range 1.6 K < T < 150 K on the EMU spectrometer at the ISIS pulsed beam facility at the Rutherford Appleton Laboratories, and the GPS spectrometer on the πM3 continuous beamline at Paul Scherrer Institute (PSI). Data was also taken at 20 mK at the Low Temperature Facility (LTF) at PSI. Powder samples were studied at ISIS in a silver holder with a Mylar window, and the small contribution (10%) of muons stopping in the silver was independently measured and subtracted from the data. Powder samples at PSI were sealed in metalized Mylar packets, with no background contribution.

5.2.2 Magnetic Susceptibility

The temperature dependent static susceptibility χ(T)=M/H of polycrystalline Nd-227 was measured from 250 K to 1.8 K in samples under a field of 1000 Oe under both zero field cooled (ZFC) and field cooled (FC) conditions, and the results are shown in Figure 5.1(a). Under ZFC conditions, we observe a small peak in of Nd-227 at T_M = 105 K, while under FC conditions we see a sharp increase at same temperature. This behavior is similar to that seen in the other *A*-227 compounds [6, 7], and occurs at a comparable temperature to the feature found in the insulating members of the series. As shown in the previous chapter, this is associated with the onset of magnetism in the Ir sublattice, as it occurs when the *A*-site species is either magnetic or non-magnetic. The anomaly at T_M is typically linked to a MI transition, which occurs at comparable temperatures. We note however that the onset temperature of the magnetic anomaly from these magnetization

measurements is considerably higher than the value of T_{MI} = 37 K extracted from earlier resistivity [11] and susceptibility measurements [6]. Such a substantial difference between samples which were fabricated under slightly different conditions indicates the sensitivity of the ground state of this compound to stoichiometric defects and disorder. This effect will be discussed in greater detail later in this chapter.

Upon continued cooling below 100 K there is a significant difference between the FC and ZFC behavior until 8 K, below which the ZFC and FC curves converge and continue to increase weakly with a further decrease in temperature.

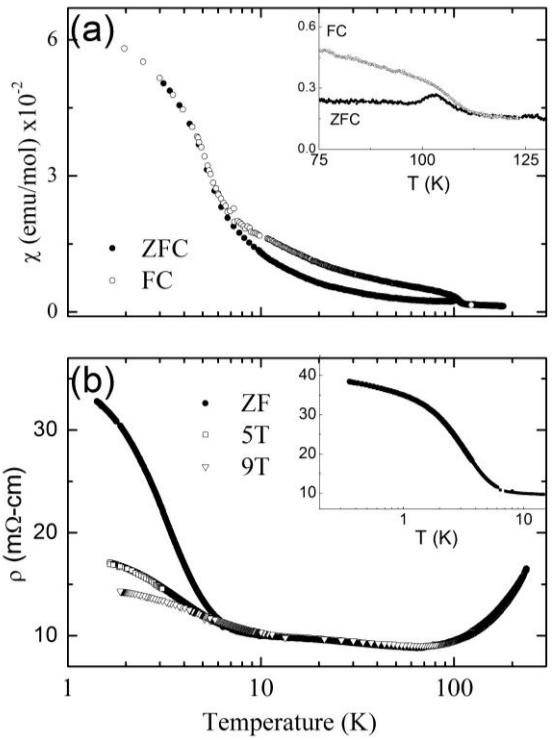

Figure 5.1. (a) Magnetization versus temperature in an applied field of 1000 G for field cooled (solid symbols) and zero field cooled (open symbols) sample of $Nd_2Ir_2O_7$. Inset: Expanded view of the susceptibility in the vicinity of T = 120 K. (b) Resistivity versus temperature for $Nd_2Ir_2O_7$ in applied fields of 0 T, 5 T, and 9 T. Inset: Temperature dependent resistivity at low temperatures in zero applied field [1]

The temperature dependent resistivity of these samples of Nd-227 is shown in Figure, 5.1(b). A decrease in the resistivity is observed below room temperature and reaches a broad minimum at T ~ 65 K. Between 65 K and 8 K there is a very weak increase in the resistivity; however below 8 K there is a second slope-change followed by a slow, nearly logarithmic increase in resistance with decreasing temperature (inset of Figure 5.1(b)) below 1 K. This logarithmic temperature dependence differs greatly from the exponential behavior expected for an insulating state, but is characteristic of correlations in a weakly metallic system (e.g., Kondo effect); this strongly suggests the absence of a metal-insulator transition in this system. Applying a magnetic field of up to 9 T we find that in the region above 8 K the magnetic field has very little effect on the resistance; in contrast a very large negative magnetoresistance is observed abruptly below this temperature the effect of which increases with decreasing temperature. To verify this behavior, samples from two different batches were measured including one sample before and after a 24 hour anneal in an oxygen environment; in all cases the data were the same, demonstrating that the observed behavior is insensitive to small changes in chemical composition.

In Figure 5.2, we show the magnetic field dependence at T = 1.8 K of both the magnetization and resistivity. Calculations shown that J = 9/2 state of Nd^{3+} splits into five Kramers doublets in the crystal field of the magnetic ion, assuming a trigonal symmetry [14]. Measurements of the crystal field energy levels indicate that the energy difference between the lowest two sets of doublets is well over 100 K [13], such that we can treat the low temperature properties as an isolated doublet. Therefore, a nonlinear least-squares fit of a Brillouin function with J_{eff} = 1⁄2 was used to describe the data. The

fit is shown as the dashed curve in Figure 5.2, corresponding to paramagnetic moments with J_{eff} = 1⁄2 and an effective moment μ_{eff} = 1.3± 0.1 μ_B. The saturation moment is consistent with measurements on other samples, including those on more insulating variants of Nd-227 [15]. This μ_{eff} is larger than the maximum estimated size of the Ir^{4+} moment, which system is greatly reduced due to the action of the orbital part of the angular momentum in t_{2g} state and is expected to be at most 1/3 μ_B [16]. Although larger than Ir^{4+}, the saturation moment is much smaller than the free Nd^{3+} moment, this is due to constraint of the Ising symmetry which greatly reduces the effective paramagnetic saturation moment, up to a factor of two for a perfect Ising axis [15]; taking this into account we expect an actual moment of 2.6 μ_B/Nd which is similar to that extracted from inelastic neutron scattering [13]. From this, we conclude that the Nd moments remain in a paramagnetic or degenerate state down to at least 1.8 K whereas the Ir^{4+} moments undergo a magnetic transition at 120 K.

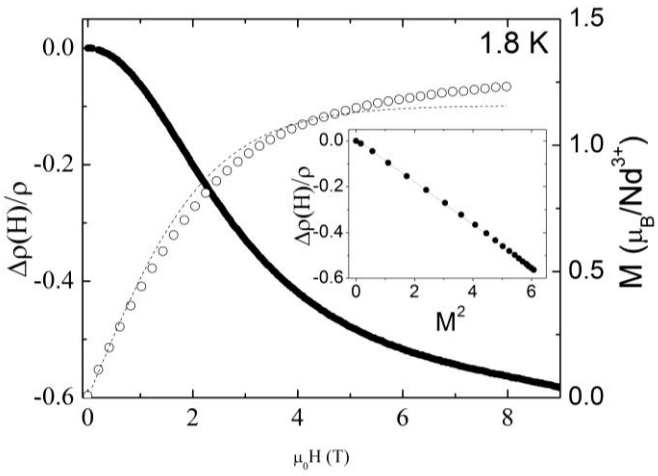

Figure 5.2. Magnetic field dependence of the resistivity and magnetization at T = 1.8 K. The dashed line shows the fit to a Brillouin function as described in the text. Inset: variation of the fractional change in resistivity with the square of the magnetization, with magnetic field as an implicit parameter; the straight line is a guide to the eye [1]

We performed detailed elastic neutron scattering measurement to study possible correlated Ir^{4+} spin order or indications of structural transitions which could lead to the magnetism we observe in susceptibility below 100 K or 8 K. Two separate batches of polycrystalline $Nd_2Ir_2O_7$ powder were studied on the HB-2A and HRPD diffractometers at the ORNL High Flux Isotope Reactor and the ISIS spallation neutron sources respectively. Data from HB-2A were collected with λ_i = 1.5385 Å with a Ge(115) monochromator and 12'-31'-6' collimation, and data were refined using the FullProf software package. The results of the refinement at T = 3K are plotted below in Figure 5.3. No structural transitions or new antiferromagnetic Bragg peaks were observed nor was there any ferromagnetic enhancement of the nuclear peaks upon cooling below the magnetic transitions at both 120 K and 8 K. This sets a conservative estimate of the maximum size of the long-range ordered moment of ~ 0.5 μ_B for Q = 0 modes and 0.2 μ_B for $Q \neq 0$ modes, similar to those limits obtained for Y-227 [16, 7]. A highly disordered magnetic state such (*e.g.* spin-ice) or a state with a small correlation length may also preclude detection of correlated magnetism in this measurement.

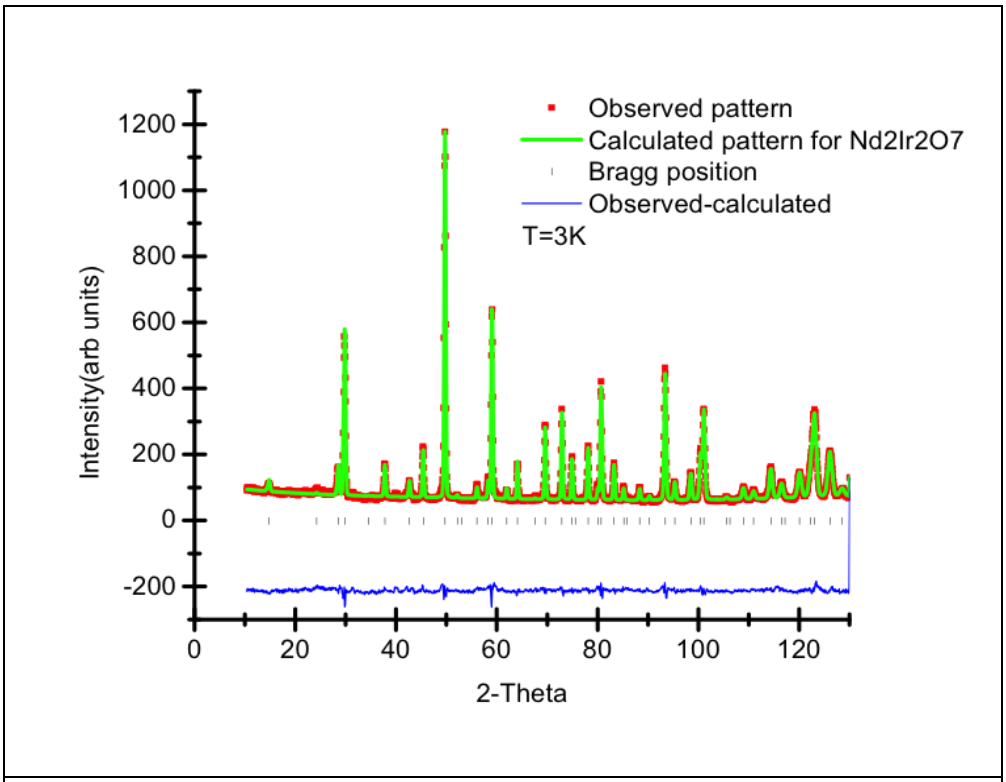

Figure 5.3. Neutron powder diffraction data collected on HB-2A. The measured data (red circles) are overplotted with the calculated pattern described in the text. Vertical tick marks denote the calculated Bragg positions and the solid blue line denotes the difference between the calculated and observed patterns.

Further diffraction measurements at the HRPD diffractometer at the ISIS spallation source, which should allow for better statistical resolution due to enhanced detector coverage, did not improve upon our initial results, and solidified the lower bounds of the possible ordered moments described above. In order to directly compare with the order parameter reported by Tomiyasu *et al.* [13], we plot the integrated intensities from the Q = (2, 2, 2) and Q = (1, 1, 3) nuclear reflections at T = 4 K, 75 K, 180 K, and 300 K (Figure 5.3). The window of integration is plotted in Figure 5.3(a), and upon cooling from 300 K, we observe a continuous decrease in this integrated signal with

no observable increase at 4K due to Nd^{3+}-ordering (Figure 5.3(b)). This integrated time-of-flight data approaches the statistical accuracy of the earlier report by Tomiyasu *et al.* and allows us to conclude that the ordered moment reported in $Nd_2Ir_2O_7$ is either substantially diminished or not present in our samples. This discrepancy may be due to an extreme sensitivity to the sample stoichiometry or oxygen content; however this would be surprising given the higher energy scale of the Ir^{4+} ordering anomaly observed at T_{Ir} = 105 K in our samples relative to the earlier reported T_{Ir} = 37 K [6, 11].

From these combined measurements, we can conclude that within comparable statistical confidence of Ref. [13] that the long-range magnetic signal reported below 15 K in earlier reports is not present in our sample. Detailed inelastic scattering measurements should in theory provide more information on this state through measurements of the diffuse scattering and fluctuation spectra, however the smallness of the moments on the Ir sublattice will continually be a mitigating factor in these materials [16]. While this could be overcome with sufficiently large single crystals, current growth methods preclude this possibility.

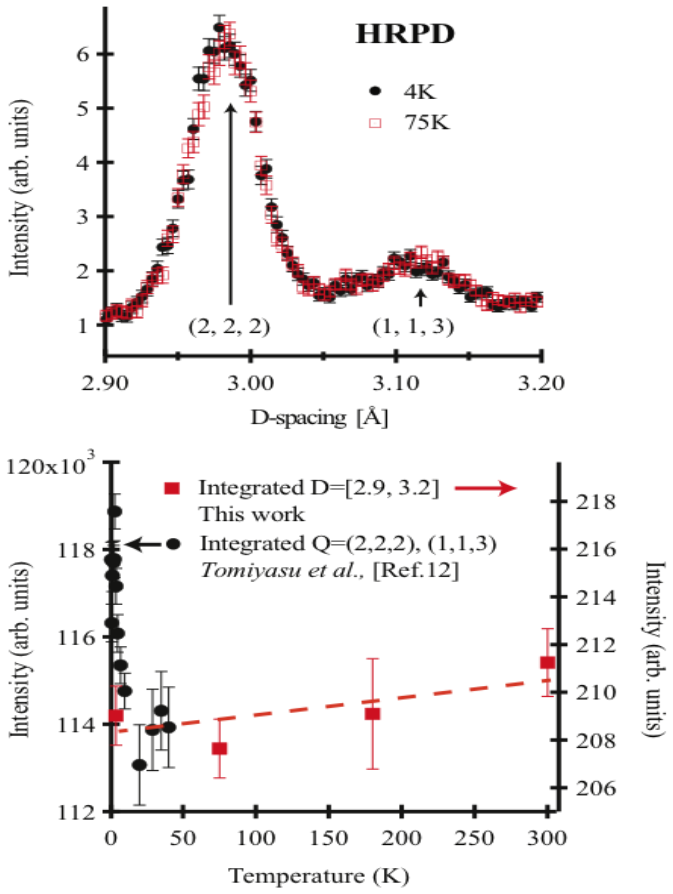

Figure 5.4. Top panel shows scattering intensities measured at 4K (black circles) and 75K (open squares) in the low angle bank of HRPD. Bottom panel shows the integrated intensities measured between D-spacings of 2.9 and 3.2 Å as a function of temperature (red squares). Black circles are data taken from Ref. [13] for relative, statistical comparison [1].

5.2.3 μSR

In order to explore the magnetic state further, μSR measurements were performed on two spectrometers with complementary resolutions/sensitivities to both fast relaxation processes (GPS and LTF at PSI) and slow relaxation processes (EMU at ISIS). By combining these measurements, we obtain a picture of both static and fluctuating magnetic fields throughout the bulk of the sample over a broad frequency domain. In modeling the data at higher temperatures (T ≥ 8 K), the time-dependent depolarization curves can be fit by a stretched exponential function

$$P(t) = A_s exp[-(\lambda_s t)^{\beta}] \qquad (5.1)$$

where A_S is the asymmetry of the depolarization, normalized to the independently measured full asymmetry, λ_s is the slow depolarization rate and β is the stretched exponent. For the ISIS data, A_S and λ_S are both left as fit parameters, since the onset of fast depolarization will be manifest in a loss of apparent asymmetry. As for the GPS data, the asymmetry was independently measured and A_S was fixed at this value. The results are shown in Figure 5.5, where above 10 K we see excellent agreement between the results taken at the two different facilities. The slow depolarization rate λ_S shows a clear change at T_M ~ 105 K, close to the temperature at which the magnetization exhibits the onset of hysteretic behavior (see inset of Fig. 5.1). Note that no muon precession is observed for 8 K < T < T_M showing lack of long-range order in this temperature region. Below 10 K, a dramatic increase in the relaxation rate is observed. For the EMU data, A_S is nearly constant near its full value at higher temperatures indicating that fast relaxation processes are negligible. However, below about 10 K A_S drops rapidly, reaching a value of approximately 0.39(1) of the full asymmetry at 1.6 K. This behavior clearly

demonstrates the onset of fast depolarization processes, and accounts for the difference in λ_S for the two data sets below 10 K. The exponent β is shown in the inset of Figure 5.5 for both the GPS and EMU data, and has a value 1.05 ± 0.02 at high temperatures which drops to 0.80 ± 0.02 below 120 K, then drops again below 20 K to a value of 0.50 ± 0.05 at 8 K.

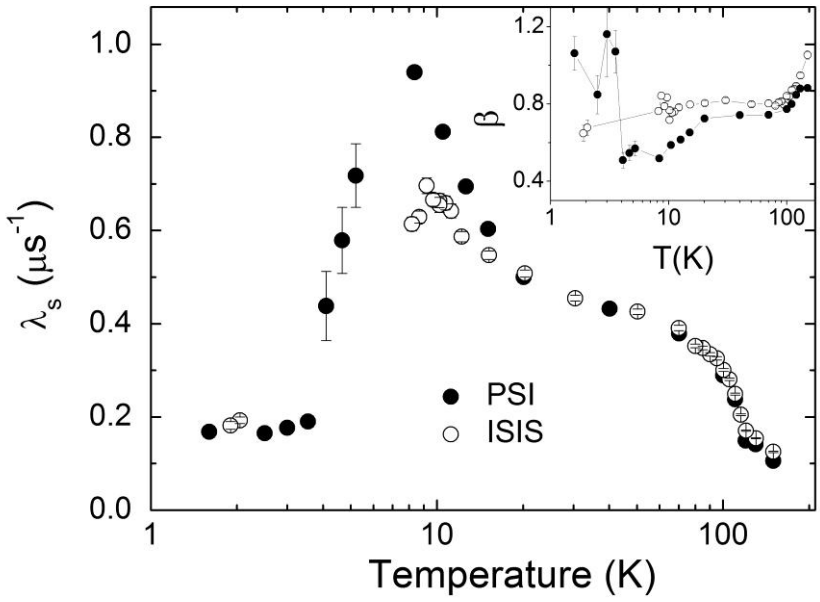

Figure 5.5. Temperature dependent muon depolarization rate for extracted from data taken at ISIS and PSI, as described in the text. Inset: Temperature dependence of the stretching exponent β as described in the text [1].

In Figure 5.6, we show a sequence of low-temperature depolarization curves taken on GPS, where the fast relaxation processes can be observed. Upon cooling below T = 8 K, we see the onset of spontaneous oscillations, unambiguously demonstrating the existence of magnetic ordering. The oscillations are heavily damped, and attempts to fit the data to the expected two-component depolarization function for polycrystalline

samples with magnetic order utilized in Ref. [17] and [7] and described in Chapter 4, Eq. 4.2, were unsuccessful. A three-component depolarization function of the form

$$P(t) = A_1 \exp(-\lambda_1 t)\cos(\omega t + \phi) + A_2 \exp(-\lambda_2 t) + A_3 \exp\left[-(\lambda_3 t)^{\beta}\right] \quad (5.2)$$

yields an adequate fit to the data at 1.6 K, as shown applied to the lowest temperature curve taken for Nd-227 as shown in Figure 5.6. This can be compared to the uppermost curve, taken at 8 K, which is shown fit to the stretched exponential as described above. From the fit of Eq. 5.2, we find a muon precession frequency $\omega_\mu/2\pi$ = 8.8(2) MHz, corresponding to an average local field for the precessing muons of $\langle \boldsymbol{B_{loc}} \rangle$ = 665 G. Fourier transforms of the data confirm the location of the peak in the field distribution, and indicate a very broad with a half-width of approximately 5 MHz which stems from the large damping of the oscillations observed in Figure 5.6. The extracted frequency is significantly smaller than the 13.3 MHz value observed for Eu-227 ($\langle \boldsymbol{B_{loc}} \rangle$ = 987 G) [Zhao], and the 14.8 MHz ($\langle \boldsymbol{B_{loc}} \rangle$ = 1100 G) found for Y-227, and Yb-227 [Disseler A-227]. The extracted depolarization rates are λ_1 = 13(1) μs^{-1}, λ_2= 15(2) μs^{-1}, λ_3= 0.18(1) μs^{-1}, and β = 1.07(6) with relative amplitudes A_1 = 9.3, A_2 = 6.7(6), and A_3 = 7.1(4); the total amplitude $A_1 + A_2 + A_3$ was constrained to be the measured full asymmetry, with the ratio of slowly decaying asymmetry (A_3) to the total asymmetry found to be approximately 0.30(2). The resultant phase angle is extremely large, φ = -63° and the fit deviates from the data at very short times.

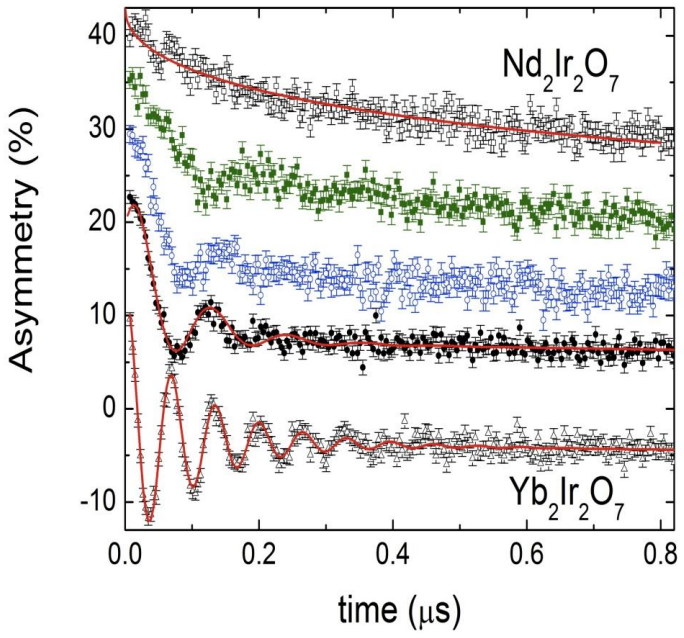

Figure 5.6. Evolution of the short-time muon depolarization curves (PSI) with decreasing temperature. The upper four curves are for $Nd_2Ir_2O_7$, at temperatures of 8 K, 5 K, 3.5 K, and 1.6 K from top to bottom; higher temperature curves have been offset from the 1.6 K curve by successive increments of 6 for clarity. The bottom curve is for $Yb_2Ir_2O_7$ at 1.6 K (from Ref. 5), and has been offset by -12. The solid lines are fits to Eq. 1 for the T = 8 K data and to Eq. 2 for the T = 1.6 K data for the $Nd_2Ir_2O_7$ curves; the solid line for the Yb curve is a fit to the depolarization function as described in Chapter 4.

We also achieved a reasonable alternative fit of the data at 1.6 K using a two-component Bessel function:

$$P(t) = A_1 exp(-\lambda_1 t)\, J_0(\omega_\mu t) + A_2 exp\left[-(\lambda_2 t)^\beta\right] \qquad (5.3)$$

where J_0 is the spherical Bessel function of the first kind, as commonly used in systems exhibiting spin density wave ordering [18]. For Eq. 5.3, we extracted the parameters $\omega_\mu/2\pi$ = 8.26 MHz, λ_1 = 9.8 μs^{-1}, λ_2 = 0.23 μs^{-1} β=0.45, and η = 0.42. Here again the relative contribution of A_2 of the total asymmetry and λ_2 are found to be roughly

independent of temperature below 5 K. Although this fit captured the very short and long times accurately, it failed to accurately describe the entire time interval below 1 μs meaning that this is not the most accurate description of the locally ordered state either. Both Eq. 5.2 and 5.3 yield similar values for the local field and damping components which measn that regardless of the actual fitting function we can be reasonably certain of the extracted value of the local field, as well as rate of the slow depolarization term below 8 K.

The asymmetry spectrum taken at 1.6 K on Yb-227 is also shown as the lowest curve in the figure; we find that even though Yb^{3+} has a large, localized moment approximately equal to that found on Nd^{3+} there are considerable differences in both the frequency and damping of the oscillations. Comparing the results from Chapter 4 of Y-227 and Yb-227 with those of Nd-227, we find that presence of a magnetic rare-earth sublattice leads to a broader distribution of the local field than if Ir is the only magnetic species lattice alone, however this effect alone cannot explain the differences between the Yb-227 and Nd-227. While 1.6 K is well below the transition temperature of Yb-227 ($T/T_{LRO} \sim 0.01$) for Nd-227 we find $T/T_{LRO} \sim 0.2$, meaning that one could argue the above result is not really an even comparison. To achieve a similar temperature fraction, we have performed measurements of Nd-227 to 20 mK on LTF at PSI with a very large number of counts. The short time asymmetry at 20 mK can be seen below in Figure 5.7; f we find that the data is largely unchanged from that taken at 1.6 K, with neither the frequency nor amplitude of the oscillations increasing. The Fourier transform of this curve (after subtracting the long-time exponential decay) is shown in the inset with highlights the extremely large width of the local field distribution. Based on these results,

we see that the order parameter is sufficiently saturated by 1.6 K meaning that the long-range magnetic order has fully developed by this temperature. These low temperature measurements also indicate that the local field does in fact broaden slightly with decreasing temperatures similar to Yb-227 and may suggest a non-trivial magnetic state on the Nd sublattice as well.

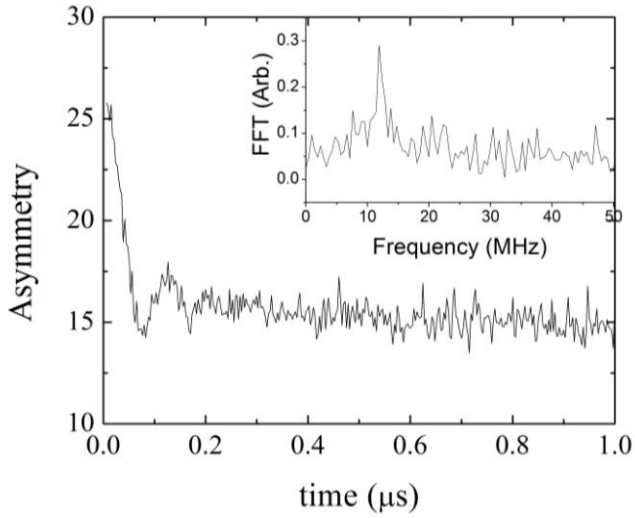

Figure 5.7 Short-time Asymmetry curve for Nd-227 at 20 mK from LTF. Inset: FFT spectrum of the data below 4 μs showing the broad peak above 10 MHz.

We have also conducted low temperature longitudinal field measurements on EMU, where the fast decaying component is not detected by the spectrometer so we are only measuring the slowly relaxing component (equivalent to the third component in Eq. 5.2). The normalized asymmetry $\eta_S = A_S/A_{total}$ and the depolarization rate λ_S are shown as a function of the applied field at T = 1.6 K in Figure 5.8. We find that the zero-field limits, η_S = 0.36(1) and λ_S = 0.17(2) μs^{-1} are in good agreement with the GPS results. A

field of about 350 G is required to restore half of the missing asymmetry by decoupling the muon from the local magnetic field; this is similar to the results of Y-227 and Yb-227 shown in Figure 4.7 where half of the local field was needed to restore the full asymmetry. We also find that the depolarization rate λ_S is independent of applied field up to 300 G, at which point the muon is decoupling from the local field. Since $\lambda_S / \gamma_\mu \approx 2$ G, the lack of magnetic field dependence in λ_S demonstrates that the long-time depolarization is dynamical in origin. The jump in the depolarization rate near 600 G is due to the return of the initial asymmetry, which causes the short-time relaxation to appear anomalously fast. For fields above 1000 G λ_S does begin to decrease again suggesting that the long-time rate is entering the motional-narrowing limit and that the behavior may follow something akin to the Redfield model discussed in Chapter 4, Eq. 4.6.

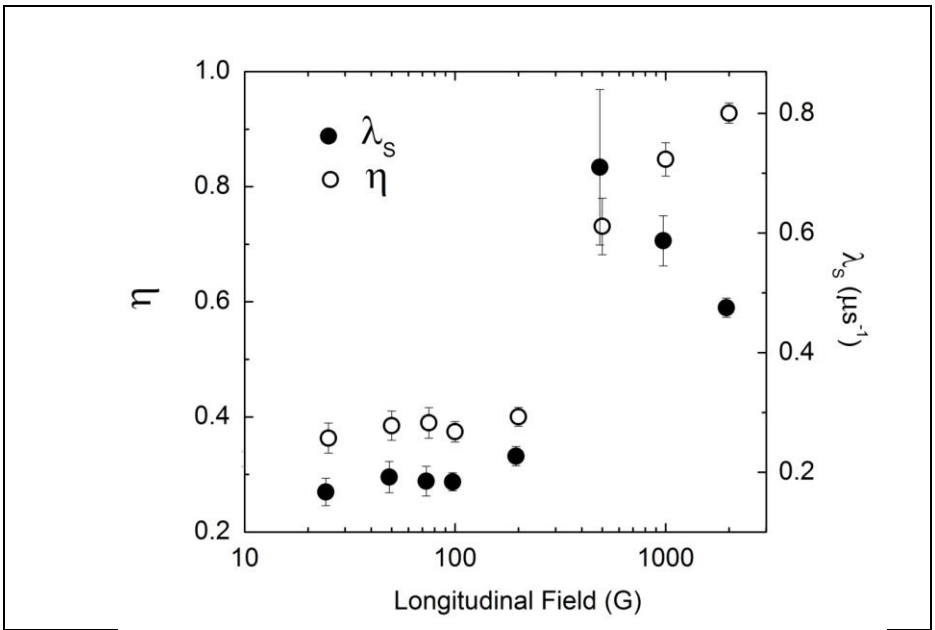

Figure 5.7. Longitudinal magnetic field dependence of the slow depolarization rate $Å_S$ and its fractional asymmetry component η at T = 1.6 K extracted from data taken at ISIS [1].

5.3 Hysteresis in the Hall Effect and Magnetization

The μSR measurements have unambiguously indicated the presence of long-range order below 8 K, however as the local field distribution was found to be so different from the insulating Y-227, Yb-227 and Eu-227, we cannot speak in much greater detail about the nature of the ordered state without additional information. One possible way to gain such insight is through detailed study of the magnetic field hysteresis of the magnetization and Hall effect through the magnetic transitions at T_M and T_{LRO} described in the previous section. This is of considerable interest because of the proximity in size of Nd-227 to Pr-227 which appears to contain an unusual chiral metallic ground state [19]. As described in the Chapter 2, μSR measurements of Pr-227 have shown that long-range magnetic order as occurs in the insulating *A-227* series does not exist on either Pr or Ir sublattices to 20 mK [20]. On the other hand, numerous transport and magnetization studies of single crystals reveal that the Pr sublattice sublattice likely exhibits a spin-ice like configuration with the Ir ions containing little or no local moment, i.e. complete itinerant [19-21]. Through measurements of Nd-227 we hope be able to draw conclusions about how such a state may evolve from the magnetically ordered correlated insulators in the series.

The polycrystalline samples of $Nd_2Ir_2O_7$ measured in this section were taken from the same batches as those used in the preceding measurements. Magnetization measurements presented in this section were performed using a Quantum Design MPMS SQUID magnetometer. Data for isothermal hysteresis loops were taken by cooling the sample in nominal zero field, and sweeping the field over the cycle 0 → 5 → -5 → 0.1 or 5 T. Individual data points were taken while sweeping magnetic field at a constant rate of

70 mT/min. The sample was warmed to T = 130 K > T_M after each isothermal run. Magnetotransport was measured at and above 2 K in a Quantum Design PPMS system, and below 2 K in a ^{3}He cryostat with a 9 T magnet. Several pressed samples prepared from independent batches were studied; all were polished into bar geometries with typical sample with thicknesses in the range 0.5 – 1 mm. For Hall effect measurements, two contacts were placed at sample edges perpendicular to both the current flow and field directions, while for longitudinal magnetoresistance measurements the Hall voltage was shorted with the voltage leads extending across the sample, and the magnetic field was applied parallel to the current direction.

5.3.1 Field Dependent Magnetization

In Figure 5.9 we show the magnetization at T = 2 K over the field cycle 0 → 5 → -5 → 0.1 T. Data are presented as μ_B per Ir or per half formula unit or μ_B/$NdIrO_{3.5}$ although in reality as Nd^{3+} makes a large contribution to the total magnetization. A small hysteresis loop centered on zero field (lower right inset) is seen with a zero-field moment of ±0.015μ_B/Ir, roughly three orders of magnitude larger than that observed for Y-227in the long-range ordered state near 100 K as reported in Ref. [16], and two orders of magnitude larger than that measured by us on our own Y-227 samples shown in Chapter 4. Also evident is a hysteresis loop centered on a field value -B_c ≈ -2.5 T. The magnitude of the hysteresis is 2.5 times larger than that at zero field. Measurements over the field cycle 0 → 5 → -5 → 5 T at T = 3, 4, and 5 K show that the hysteresis occurs at both positive and negative values of B_c. Plotting the derivative dM/dB for the up and down

field sweeps (upper left inset) shows that a peak occurs at a field of magnitude B_c and pointing opposite to the previous magnetizing field direction, that is, at $+B_c$ for the field sweep -6 to 6 T, and at $-B_c$ for 6 to -6 T. The virgin curve 0 → 6T also shows a peak in dM/dB at B_c (not shown), but with a size about one-half those depicted in the inset. This behavior is not typical for metamagnetic transitions (*e.g.* spin-flip or spin-flop), which typically occur at $\pm B_c$ for both sweep directions, with potentially some small hysteresis about that value.

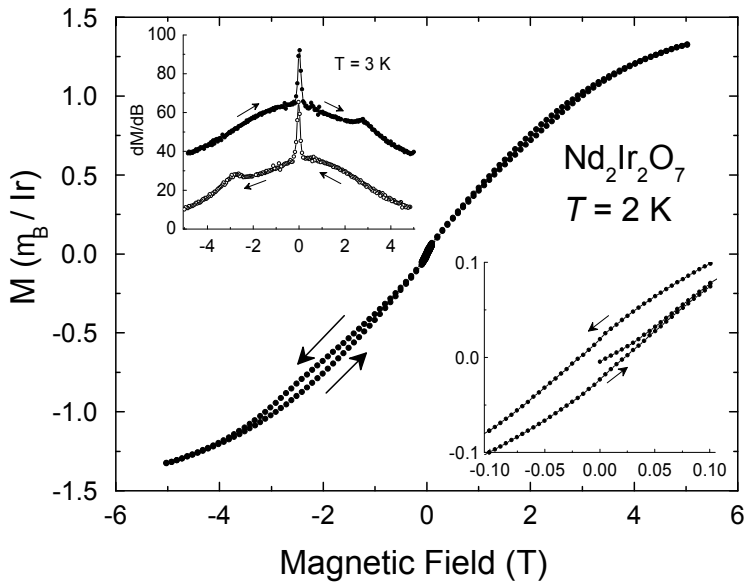

Figure 5.9 Magnetization hysteresis loop for $Nd_2Ir_2O_7$, with a field cycle of 0 → 5→ -5→0.1T. Lower right inset: close-up of the hysteresis in the vicinity of zero field. Upper left inset: Derivative *dM/dH* (in units of $10^{-2}\mu_B$/T) for 5→ -5T (lower curve) and -5 to 5 T (upper curve), taken at T = 3 K [2].

In Fig. 5.10 the temperature dependence of the difference between the down and up sweep magnetizations, $\Delta M = M_{down}(B) - M_{up}(B)$ are shown for zero field (ΔM_{ZF} in Fig. 5.10a) and at B_c (ΔM_{HF} in Fig. 5.10b); the insets show representative curves taken at several temperatures about the magnetic field range of interest. In Figure 5.10(a) we see

two abrupt changes in ΔM_{ZF}, near 110 K and 10K. These temperatures correspond closely to the two transitions observed previously in μSR, transport, and dc susceptibility results , $T_M \approx 110$ K and $T_{LRO} \approx 8$ K. A similar two-step transition was observed in Y-227, with $T_M \approx 190$ K and $T_{LRO} \approx 150$ K, while μSR measurements of Bi-227 also show a two-step change in the relaxation rate at 2 K and 0.3 K [Baker]. As will be discussed in detail in Chapter 6, these suggest that this effect is ubiquitous to the pyrochlore iridates, and may be the result of a short-range ordered phase preceeding the long-range or glass-like true ground state.

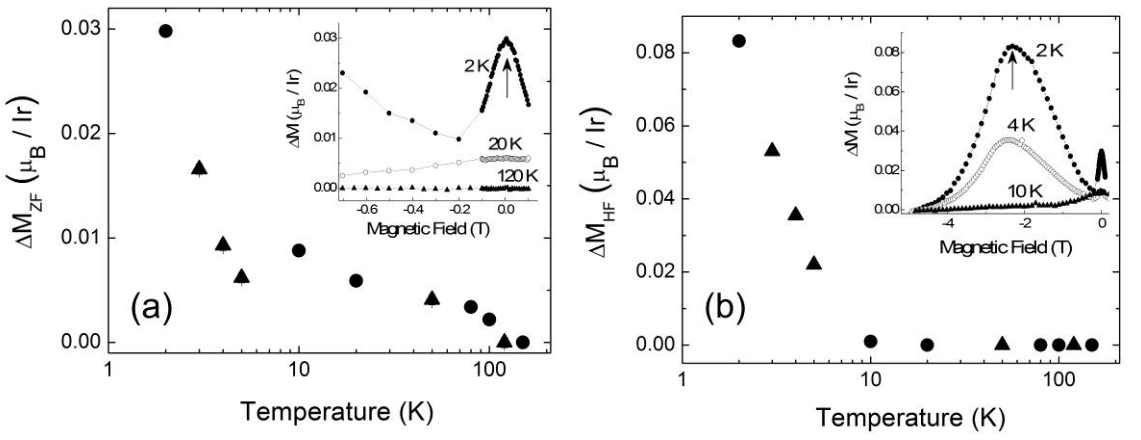

Figure 5.10 (a) Temperature variation of the maximum in $\Delta M = M_{down} - M_{up}$ at zero field. The inset shows detailed curves for ΔM in the vicinity of zero field at three temperatures. (b) Temperature variation of maximum in ΔM near -2 T.The inset shows typical curves for ΔM at three temperatures. Different symbols (solid circles, solid triangles) represent data taken on different experimental runs [2].

From Figure 5.10(b) we see that as the temperature decreases below 10 K, ΔM_{HF} increases rapidly from zero, and so we assume the onset of hysteresis at B_c is associated with the onset of long-range magnetic order at T_{LRO}. This type of hysteresis was observed

in Pr-227 below the spin freezing temperature for fields applied along the [*111*] direction only [19], however as full hysteresis loops have not been published on that system, it is unknown if a similar behavior with regard to field sweep direction exists in Pr-227 as well. Regardless, it was estimated, based on the size of the localized Pr^{3+} moments that the hysteresis corresponded to a partial stabilization of 3-in/1-out (3I3O) within the 2-in/2-out (2I2O) matrix below the spin freezing temperature. This picture is consistent with Monte Carlo simulations incorporating RKKY interactions on the pyrochlore lattice which suggest a transition from spin-ice to polarized Kagome or 3I1O state at high fields [23]. Measurements of the magnetization of the insulating spin ice compound $Ho_2Ti_2O_7$ at low temperatures have also shown transitions from 2I2O to 3I1O at high fields applied along the [111] direction, which are hysteretic in nature [24]. Comparison with our results strongly suggests a similar phenomenon is occurring in Nd-227.

5.3.2 Magnetocaloric Effect (MCE)

Depending on the detailed nature of the transition between ordered and disordered state, there should be a substantial change in the free energy of the system above and below the critical field value, which should be observable using measurements of the field dependent specific heat [25]. A preliminary measurement of the magnetocaloric effect (MCE) to find such a thermodynamic signature was performed on Nd-227 at 500 mK in a sample-in-vacuum ^{3}He cryostat. The sample was in a high vacuum environment, and isolated from the ^{3}He bath by 5mm of Stycast 1266 epoxy; a bare-chip Cernox 1030 thin film thermometer was attached to the sample with conductive silver paint, and 2-mil

brass wires approximately 5 mm in length acted as electrical connections and as weak thermal links to the bath. A second factory-calibrated Cernox 1030 thermometer was used to measure the temperature of the cryostat during the field sweep and to calibrate the bare chip thermometer attached to the sample. Both thermometers were then measured as the field was then swept from +6 T → -6 T and then from -6 T → +6 T at a constant rate of 0.045 mT/min.

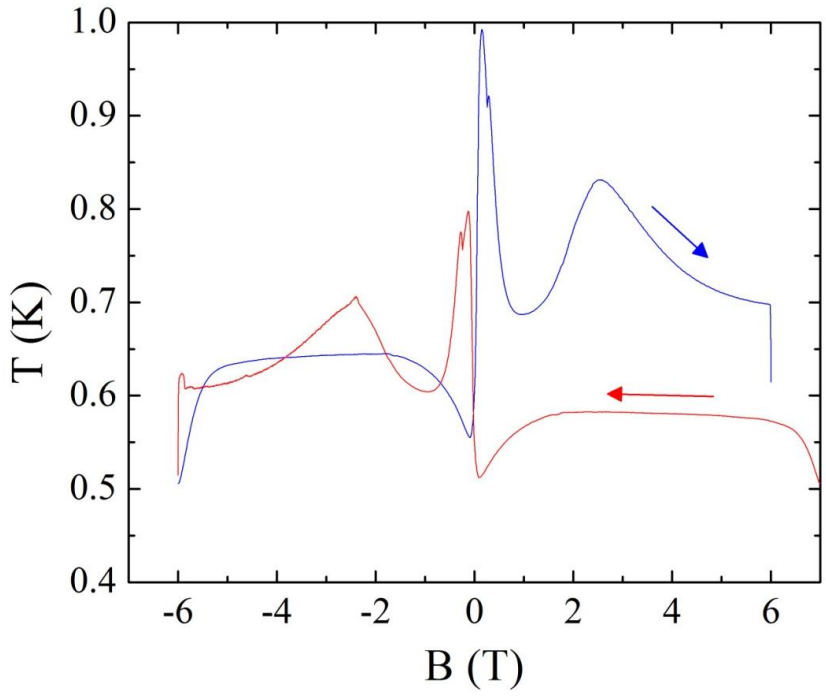

Figure 5.11 Temperature of the sample showing the MCE for field swept at a constant rate of 0.045 mT/min. The red curve and blue curves are for the negative (+6 T to -6 T), and positive (-6T to +6 T) sweep directions respectively [Disseler-2013].

Shown in Figure 5.11, the sample temperature increases greatly near ± B_c depending on sweep direction, indicating a release of heat by the sample. The field

history dependence of the MCE follows closely with that observed in magnetization, from which we conclude that the sample enters a state of lower magnetic-entropy at high fields, causing the release of heat near B_c. Any intrinsic effects near zero magnetic field are obscured by magnetocaloric effects related to magnetic impurities in the copper platform and/or thermometer, as these effects are systematically observed in the bath thermometer as well. We also note that a drift in the base temperature of the cryostat during the positive sweep direction caused the apparent offset between of the up and down sweep directions, however this does not qualitatively affect the results presented here.

5.3.3 Anomalous Hall effect

We now describe our Hall effect results. Due to imperfect alignment and probable current flow irregularities in the sintered samples, our signal had a large contribution from the resistance (Figure 5.12(a)). The Hall voltage was extracted by taking the antisymmetric part of the measured voltage and then examining the field history dependence.This was done for field sweeping from -6 to 6 T and also from 6 to – 6 T. At 10 K the magnetic field response is dominated by the Hall contribution because the resistance is essentially field independent, but at lower temperatures the magnetoresistance is large, and so the Hall (antisymmetric) component is only 4% of the total change by 2 K. Because the Hall signal is a relatively small fraction of the total signal, we independently measured the longitudinal magnetoresistance; no asymmetry is observed with respect to field, and any hysteresis observed between sweep directions

near B_c was near the limits of the experimental error. We note that the offset at zero field between the virgin zero field cooled and zero field after ramping to 6 T was observed in both Hall and longitudinal geometries.

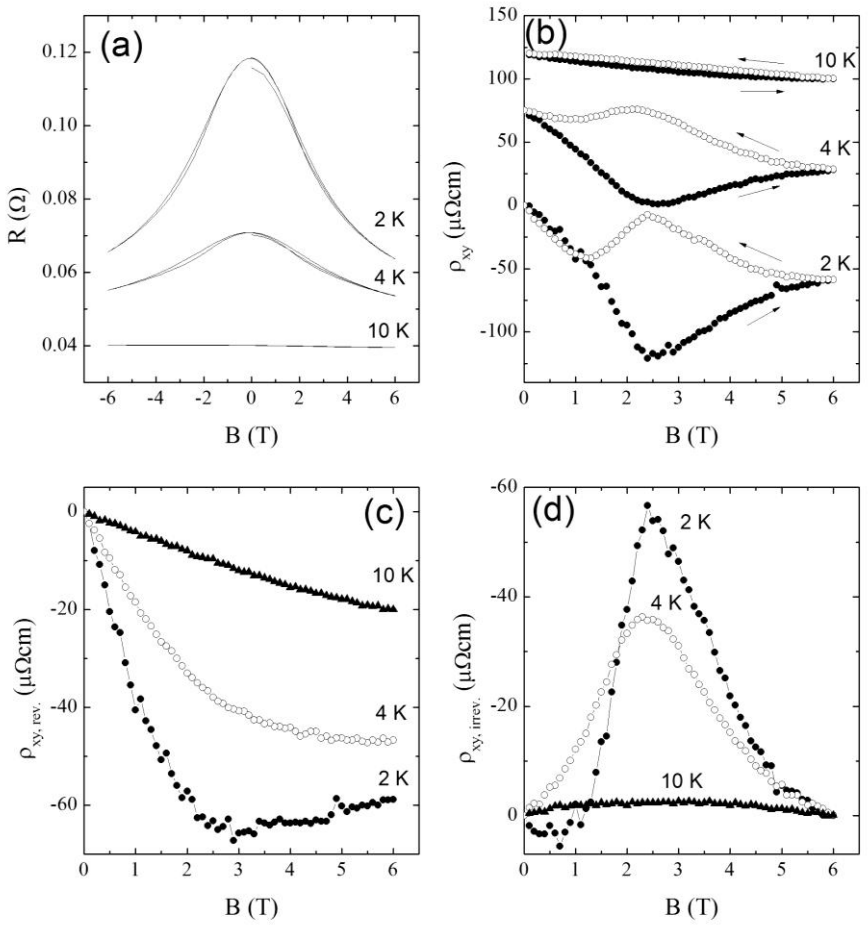

Figure 5.12. (a) Resistance versus magnetic field for a sample in the transverse geometry over the cycle 6 → -6 → +6 T at several temperatures. (b) Hall resistivity extracted from the antisymmetric part of the curves in Fig. 3a from 6 → - 6 T (open symbols, left-pointing arrows) and -6 → 6 T (closed symbols, right-pointing arrows). The curves at 4 and 10 K are offset by 0.11 and 0.22 Ω cm, respectively, for clarity; (c) reversible and (d) irreversible part of ρ_{xy} taken from the data in (b) as described in the text [2].

The field dependence of the Hall resistivity is shown in Figure 5.12(b) with each isotherm offset for clarity. While at temperatures higher than 10 K the signal is linear and nearly independent of field sweep direction, at lower temperatures we find a non-monotonic variation of the Hall resistivity with field, with strong field history dependence. In Figure 5.12(c) and (d) we show the reversible and irreversible components of the field dependence of ρ_{xy}; these are found by taking half of the sum (reversible) or difference (irreversible) of the forward and backward sweep directions shown in Figure 5.12(b) for each temperature. The magnetic field dependence of the reversible component is characteristic of an anomalous Hall effect, which is expected in a system with magnetic ordering and strong spin-orbit coupling, as discussed below. In this case, we can find the approximate carrier concentration by fitting the reversible part of the data at high fields ($B > 4$ T) where M has nearly saturated, allowing us extract a lower limit on R_0. Using the single band approximation, $R_0 = -1/ne$, and we find an upper limit of electron-like the carrier concentration of 2.5 x 10^{20} cm^{-3}, compared to 4 x 10^{21} cm^{-3} measured in small single crystals of Pr-227 [Balicas]. This confirms our expectation that Nd-227 exhibits properties intermediate between those of metallic Pr-227 and the insulating members of the A-227 family. The presence of a finite number of conduction electrons will lead to an long-range RKKY interaction between the localized Nd moments located at R_l and $R_{l'}$ given by Eq. 5.4 below, where j is the effective coupling consant, ε_F is the Fermi energy with a wavevector with $k_F = (3\pi^2 n)^{1/3}$, and $x = 2k_F(R_l - R_{l'})$ with $R_l - R_{l'}$ the distance between interacting magnetic moments [26]. Following the arguments of Ref. [8, 21], and assuming a spherical Fermi surface with $k_F = (3\pi^2 n)^{1/3}$ we

find the resultant RKKY interaction between neighboring Nd^{3+} ions to be ferromagnetic, as in the case of Pr-227.

$$J_{RKKY}(R_l - R_{l\prime}) = 9\pi\left(\frac{j^2}{\epsilon_F}\right)\left(\frac{xcos(x)-\sin(x)}{x^4}\right) \qquad (5.4)$$

These results are remarkably similar to that obtained in artificial spin-ice structures [27] for which the field dependence of the reversible component of the Hall resistance is that typically associated with an AHE in ferromagnetic metals [28], and the irreversible component develops a peak about a critical field B_c with decreasing temperature which is related to the onset of a nontrivial and spatially varying chirality of the magnetic moments around each of the local hexagons in the Kagome lattice. Magnetization extracted from magnetotransport in Ref [27] shows a sharp change in dM/dH about the critical field, which also depends on field sweep direction in a manner similar to what we have observed in Nd-227. The anomalous transport phenomenon in this system is the result of orientation of the magnetic moments which gives a specific handedness to each hexagonal ring which is not constant throughout the sample, and depends on the magnetic field. Because the artificial spin-ice lattices are formed from a 2D Kagome structure, these may be directly related to phenomena observed in the conducting pyrochlore compounds for fields applied along the [111] direction which lies normal to the Kagome plane, as shown in Figure 2.3.

The unusual hysteresis we have observed in Nd-227 bears a striking resemblance to several spin-ice systems; furthermore, based on the field scales and size of the apparent moments involved, it is unlikely that the effects at high field can be ascribed to the Ir sublattice. From this, I conclude that the hysteresis observed in transport, magnetization

and MCE is due solely to spin-transitions on the Nd sublattice. In the next section, I will elaborate on this idea, and discuss the possibilities for the configurations of both Nd and Ir sublattices based on the preceding results.

5.4 Discussion of the Configurations of the Local Moments

The previous sections have demonstrated that the low-temperature magnetic state in Nd-227 is quite unusual, as it appears that magnetism exists on both Nd and Ir sublattices but with very different character. Up to this point, there have been two scenarios which have been proposed for this state which will now be discussed. The first is that put forth by Tomiyasu *et al* in which AIAO order is proposed to exist on both Nd and Ir sublattices inferred from their neutron scattering measurements. The second, initially suggested by Sakata on the basis of transport measurements [12] is that the Nd sublattice may form in the 2I2O or spin-ice configuration that is found on the Pr-sublattice in Pr-227 [19]. However, based on the appearance of spontaneous oscillations in our μSR results, I conclude that the Ir sublattice must also be ordered in a manner that is not degenerate such that a commensurate static field is observed.

To compare the two scenarios, I have first calculated the magnetic field for several muon stopping sites in a manner similar to that done in Chapter 4 for Y-227 for all of the various configurations above. We have used the same crystallographic stopping sites determined for Y-227: Site 1 is a[0.16, 0.16, -.017] and Site 2 is a[0.55, 0.45, 0.55] with a being the lattice parameter extracted from our neutron scattering measurements at 4 K. The net field was calculated for different combinations of configurations where the Nd and Ir sublattices could be either nonmagnetic or in the AIAO state. The size of the

magnetic moment on the Nd^{3+} site was taken to be 2.37 μ_B on the basis of susceptibility and inelastic neutron scattering measurements taken by Tomiyasu *et al* [13] while the size of the Ir^{4+} was left at the maximum value of 1 μ_B. The code used to calculate the magnetic field is essentially the same as that used in Chapter 4 for Y-227 and found in the Appendix, but with an additional block to account for the second magnetic sublattice. A table of the resultant magnetic field and frequency for each combination can be found in Table 5.1 below.

Nd Configuration	Ir Configuration	Site	Field (T)	Frequency (MHz)
AIAO	NONE	1	0.79	108
NONE	AIAO	1	0.14	19
AIAO	AIAO	1	0.73	98.7
AIAO	NONE	2	3.74	506
NONE	AIAO	2	0.064	8.7
AIAO	AIAO	2	3.8	517

Table 5.1: simulation of magnetic field at two possible muon stopping sites.

The result of this calculation reveals that for the scenario proposed by Tomiyasu, in which the Nd moments are ordered in the AIAO fashion, the field at Site 1 is over 10 times larger than that extracted from muSR for, and over 50 times larger at Site 2. On the other hand, we find that the field obtained when only the Ir sublattice is considered is only a factor of 2 or so larger at Site 1 and nearly identical to that actually measured at

Site 2. This provides strong evidence against the existence of the AIAO ordred Nd sublattice, and suggests that the spontaneous local field observed in our μSR measurements is due to the ordered Ir sublattice only. Ideally, the same calculations for spin-ice structures should be performed; as this is a degenerate structure the field must be calculated for many different configurations which obey spin-ice rules and the net field averaged over all possibilities. This should not be overly difficult, and would be an excellent next step if this analysis is to be continued further.

However, one could argue that due to the increased conduction electron density, the muon stopping sites may be considerably different in Nd-227 than those considered above and taken from Y-227. To account for this, I have also performed an analysis using the Bayesian method as described in Chapter 4 and in Ref. [29]. The central field extracted from our 1.6 K measurements at PSI measurements is again used for the known field in this approach. To simulate the possible local fields, 10,000 random sites near oxygen ions were again used as described previously, with magnetic configuration chosen to be AIAO as suggested by Tomiyasu. This information was used to determine the probability that the extracted local field is created by an ordered Nd or Ir sublattice with local moments of size *m*. The resultant probability distributions for each sublattice are shown together in Figure 5.13. The probability distribution of Ir sublattice is shown as the red curve in the figure, as is quite similar to that obtained in Y-227 in Chapter 4 of this work, with the exception of an increased spectral weight near 0.6 μ_B. The corresponding distribution for the Nd sublattice is shown in blue in Figure 5.13. What we find is that there is a vanishing probability of finding a moment on the Nd-227 lattice above 1.25 μ_B which will generate the observed 660 G field. This means that it is

extremely unlikely for a lattice of Nd moments of size 2.3 μ_B/Nd in the AIAO state to produce our observed muon precession frequency. On the other hand, the moment probability distribution for Ir sublattice is well within the limits set by neutron scattering, as there is significant probability that our observed local field is the due to the summation of Ir moments which are smaller than 0.5 μ_B. This is further evidence that the LRO that we observe does not stem from the Nd-lattice, and instead occurs on the Ir-sublattice alone.

A complication to this analysis is the width of the local field distribution in Nd-227, which unlike Y-227 or Yb-227 has a FWHM that is comparable to the value of the central frequency. One interpretation of this is that there are many more possible stopping sites in N-227 due to the screening action of the conduction electrons, and effectively smears out the resulting field distribution. This analysis using Bayes theorem does show that there is a wider distribution of possible moment sizes of the Ir lattice in Nd-227 than in Y-227, which could be interpreted as a greater likelihood of a wider range of muon stopping site. In theory, a more sophisticated analysis using the entire distribution instead of just a single central field should provide more insight into this problem, however it is well beyond the current scope of this work. It may also be possible that the hyperfine interaction, which I ignored in Chapter 4, becomes important here as a result of significant overlap between the muon wave function and the spin density of the conduction electrons. These interactions are not easily calculated nor can their effect be easily approximated as it depends sensitively on the electron spin density and location of the muon.

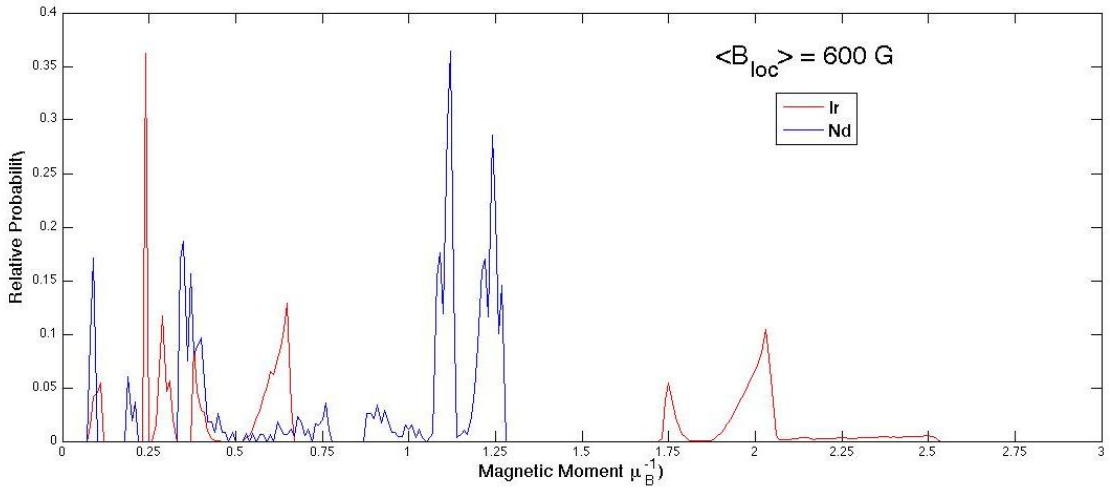

Figure 5.13 Probability distribution functions obtained from a Bayesian analysis of magnetic dipole simulations on the Nd-227 lattice. The results for the Ir sublattice are shown in red, while Nd is shown in blue.

While we have ruled out AIAO order on the Nd-sublattice we cannot say for certain if Nd orders in the 2I2O or spin-ice configurations based on the above calculations. As true spin-ice is degenerate such that the configuration does not repeat even from unit cell to unit cell, the above calculation would need to be performed for many different randomly chosen configurations which satisfy the spin-ice constraint and the results averaged together. The field distribution of the known spin-ice compound $Dy_2Ti_2O_7$ was modeled using Monte Carlo algorithms [30] in order to compare current models with previous μSR measurements [31]. The resulting distribution could be characterized as having an approximate width of over 1 T, and had a significant tail extending to large fields which corresponded to a more Lorentzian-like distribution. The large width of this distribution accounts for the rapid depolarization of the muon and explains why no coherent precession is observed in zero field [30]. This was supported by other studies in which DFT was used to calculate possible muon stopping sites,

however as these sites were not explicitly listed in that work it is difficult to perform an equivalent comparison [32]. While these results cannot prove the existence of the spin-ice state on the Nd-sublattice, our observation of the broad distribution of local fields is not incompatible with this model.

Evidence for the spin-ice state instead comes from our indirect comparison with the hysteretic effects observed in the magnetization, Hall effect, and magnetocaloric effect with other known spin-ice systems as discussed in section 5.3. These comparisons strongly imply that the magnetic ground state of Nd-227 in the weak metallic phase is of the 2I2O spin-ice type rather than AIAO as previously considered for more insulating Nd-227 variants. Recent theoretical work incorporating *f-d* exchange supports a 2I2O ground state for a wide range of coupling parameters, particularly if the average (Curie-Weiss) interaction between neighboring Nd^{3+} is ferromagnetic [33], as indicated by our estimates for the sign of the RKKY interaction in 5.3.3. This is consistent with Bramwel's original work on the pyrochlore lattice in which the spin-ice is only possible if the nearest neighbor interactions are ferromagnetic; by comparison, antiferromagnetic interactions tend to produce the AIAO state [34].

Theoretical studies have shown that the spin ice state found in Pr-227 on the Pr^{3+} sublattice may exhibit such a field dependent transition into a number of more ordered phases at high magnetic fields. These states include the Kagome-ice and 3I1O [35] and even AIAO [36], depending on the conduction electron density and strength of distant-neighbor interactions. These other state have considerably lower degrees of degeneracy and therefore have reduced entropy when compared to the spin-ice state at the same temperature; a field induced transition to any of these states should indeed be observable

by the resultant release of this entropy as we observe. To our knowledge it has not been demonstrated either theoretically or experimentally that any of these phenomena will occur if the system has a rare-earth sublattice which is in the AIAO ground state.

Our results have failed to show a MIT in this system, and instead point to a Kondo-like state as evidenced by the logarhimthic temperature dependent resistivity, and magnetoresistance $\Delta\rho=\rho(H)/\rho(0)-1$ that varies linearly with M^2 (inset, Figure 5.2). Both these are analogous to the Kondo screening observed in $Pr_2Ir_2O_7$, where both the RKKY interaction strength and Kondo temperature are approximately 20 K [8]. A comparison of this data with Eu-227 which does not contain a magnetic A-site and was made metallic through the application external pressure [37] showed that this material exhibits positive magnetoresistance proportional to H^2, similar to normal metals. This implies that the negative magnetoresistance observed in Nd-227 and Pr-227 is due to the magnetic A-site lattice, and it is this process, rather than a MI transition that causes the upturn in the resistivity below 8 K. Conversely, it has theoretically been shown that resistivity minimum and similar temperature dependence can be induced by a magnetic lattice in the spin-ice configuration which interacts with a bath of conduction electrons [38]. It was shown by Chern [39] this type of behavior was observed by the data taken by Sakata *et al.* for Nd-227 samples made metallic though applied external pressure [12]. This data closely resembles our results at ambient pressure, indicating that the Nd^{3+} sublattices are likely in the same state in both samples. As I have shown, the Nd sublattice may well be in the spin-ice configuration meaning that either the traditional Kondo interaction or spin-ice scattering are possible mechanisms for this behavior.

I now turn to discuss the onset of the unusual magnetic state at T_M near 110 K. The coincidence of the bifurcation, zero field hysteresis and increased muon depolarization rate at indicate that there is a sharp change in the magnetic state near T_M; however the lack of spontaneous muon precession at this temperature indicates there is no long-range order at this transition. In this temperature region, the system is clearly metallic, demonstrating that geometric frustration, if present, is not relieved by an MI transition in contrast to the ordering observed around this same temperature in the insulating Eu, Y, and Yb based materials. One possible explanation for this behavior is that the onset of hysteresis at zero field below T_M and near B_c below T_{LRO} correspond to distinct order parameters, such as order of the individual sublattices mediated by *d-d*, *f-f* or *f-d* interactions. We note that these two temperatures are similar to those found in the Yb-227, in which the Ir^{4+} moments order at T_{LRO} = 125 K, while the localized paramagnetic Yb^{3+} moments become polarized due to this local field and interact with an effective Curie-Weiss temperature of $\theta_{CW} \sim -7$ K, with possible transition to an unknown state below 2 K. Therefore with the addition of the RKKY interaction in Nd-227, we expect there should be significantly more impact beyond simple polarization on the underlying ground state of the Ir- sublattice and vice-versa.

However, because the two-step transition is also observed in compounds with non-magnetic *A*-sites, it is possible that this stems solely from the Ir sublattice. I argued in Chapter 4 that such a state could stem from short-range order which acts as a precursor to the long-range order which occurs at a lower temperature. This could occur via extrinsic pathways in which small clusters of ordered moments nucleate near defect centers such as grain boundaries and surfaces, or by intrinsic process driven by the

frustration of the lattice and competition between different ordering configurations. In either case, if we assume that short-range order is the cause of the magnetism at T_M then it appears that the increased conductivity or decrease in correlations in Nd-227 stabilizes this short-range ordered phase and prevented the long-range magnetic order from occurring until to a much lower temperature compared to Y-227 or Yb-227. Future studies are necessary to be able to distinguish between different mechanisms and to discern the nature of extrinsic versus intrinsic magnetism which may occur as a result of these interactions.

5.5 Charge doping Nd-227: $Nd_{2-x}Ca_xIr_2O_7$

One key question in the pyrochlore series is whether the proposed chiral spin liquid phase of Pr-227 evolves continuously into the Mott insulating ground state of the smaller bandwidth A-227 systems (e.g. Y-227, Eu-227, and Yb-227) or whether magnetic interactions are renormalized dramatically near the phase boundary to the insulating regime. We have shown through a variety of measurements that weakly metallic variants of the Nd-227 compound exhibit an intermediate or cross-over regime in which the Ir-sublattice appears to be ordered while the Nd-sublattice may exhibit spin-ice type or a similar degenerate state lacking long-range order. Because of these similarities one naively expects Nd-227 system to therefore lie in close proximity to the spin-liquid ground state of Pr-227. There are a few important differences between Nd-227 and Pr-227 which we can choose to perturb. One may choose to reduce the size of the lattice parameter through the application of hydrostatic pressure. However as shown by Tafti

[37] on Eu-227 and Sakata [12] on Nd-227, the reducing the lattice parameter in any of these compounds increases the metallic nature of the ground state counter to what one would expect. The effect of pressure on the ground state is thus not straight forward, and is not the most convenient way of interpolating between Nd-227 and Pr-227. Another possible perturbation would be to vary the density of mobile charge carriers in the system through appropriate doping, as these have been proposed to mediate many of the interesting phenomena observed in Pr-227 [36, 40].

Our Hall effect measurements above T_{LRO} indicate that the dominant carriers in Nd-227 are hole-like, therefore to increase the number of carriers we should look for dopants which will further induce holes into the conduction band, and hopefully induce minimal structural deformations which may induce other non-carrier related effects. Shown in Table 5.2, we find that the ionic radius of the Ca^{2+} ion is much closer to that of Nd^{3+} than Ir^{4+} so should substitute for the rare-earth element rather than occupy an interstitial or Ir-site. Replacing a small amount of Nd with Ca should introduce one hole into the system by introducing a finite number of Ir sites with an average valence state of Ir^{5+}. To date, only one such doping study has been performed on the pyrochlore iridate series in which divalent Ca^{2+} was substituted for the trivalent Y^{3+} in Y-227 effectively hole-doping the system to form $Y_{2-x}Ca_xIr_2O_7$ [41]. It was shown that Ca concentrations above x = 0.2 removed the magnetic bifurcation at 150 K, and increased the overall electrical conductivity with increasing x until a metallic state was formed when $x > 1.0$.

As Nd-227 is already weakly metallic, we focused first on introducing relatively small amount of calcium into the system to form $Nd_{2-x}Ca_xIr_2O_7$ with x = 0.1 and later x = 0.06. Samples were synthesized following the same protocol used in fabricating the

parent compound, with sample batches consisting of several grams each such that μSR measurements could be made on a single batch to avoid variations in the Ca concentration from batch to batch.

Ion	Radius (pm)
Nd^{3+}	112.3
Ca^{2+}	114
Y^{3+}	104
Ir^{4+}	76.5

Table 5.2: Ionc radii for several cations, assuming near octahedral coordination [42].

X-ray diffraction measurements at room temperature yield lattice parameters of 10.3611 Å and 10.35190 Å for $x = 0.06$ and 0.1 respectively, with an oxygen parameter $x = 0.3490(5)$ for both. The reported Ca concentration was determined by EDXS measurements on the final product, and again has an error of approximately 2%, such that the actual concentration is $x = 0.1 \pm 0.02$. As a first study, we performed transport, Hall effect, and μSR measurements on the $x = 0.1$ sample which will be discussed in detail below. We should note that the surfaces of these samples were prone to oxidation with noticeable differences in the measured conductivity when exposed to moist air in the lab for more than a day. These changes could be reversed by removing the surface later and reapplying lead wires to the virgin surfaces. This is likely due to the Ca absorbing water from the air which results in an insulating surface layer. Because of this, care was taken to reduce the exposure to unregulated atmospheric conditions, and samples were stored either under vacuum or in a dry-box with desiccant.

5.5.1 Transport Measurements

For resistivity and Hall effect measurements, samples of $Nd_{1.9}Ca_{0.1}Ir_2O_7$ were cut into bar shapes with typical dimensions of 2 x 0.5x 0.5 mm. A four-wire technique was employed as previously described, with samples measured between 3 K and 300 K using a cryogen-free Gifford-McMahon type refrigerator in Prof. Stephen Wilson's lab or to 300 mK using the Janis ^{3}He refrigerator described in Chapter 3, with either the LR 700 or LS 370 AC resistivity bridges employed in performing the measurements. The temperature dependent resistivity to 3 K is shown in Figure 5.13 along with the data taken from Figure 5.1(b) for the undoped Nd-227 presented previously for comparison. The room temperature resistivity in the x = 0.1 sample is 50% larger than that of the undoped compound, however this may be due to the variation of the porosity which affects the geometric factor in converting from resistance to resistivity, as both compounds display similar temperature dependences above 100 K. We also find that the resistivity of the doped compound does not exhibit the minimum seen near 100 K in the and the upturn below 10 K is substantially reduced. A close-up of the temperature region below 25 K, shown in the inset of Figure 5.13, reveals more clearly that the minimum of the resistivity is observed at approximately 8 K, or very close to T_{LRO} in the parent compound, however the increase in resistivity below 8 K is greatly reduced relative to the undoped sample.

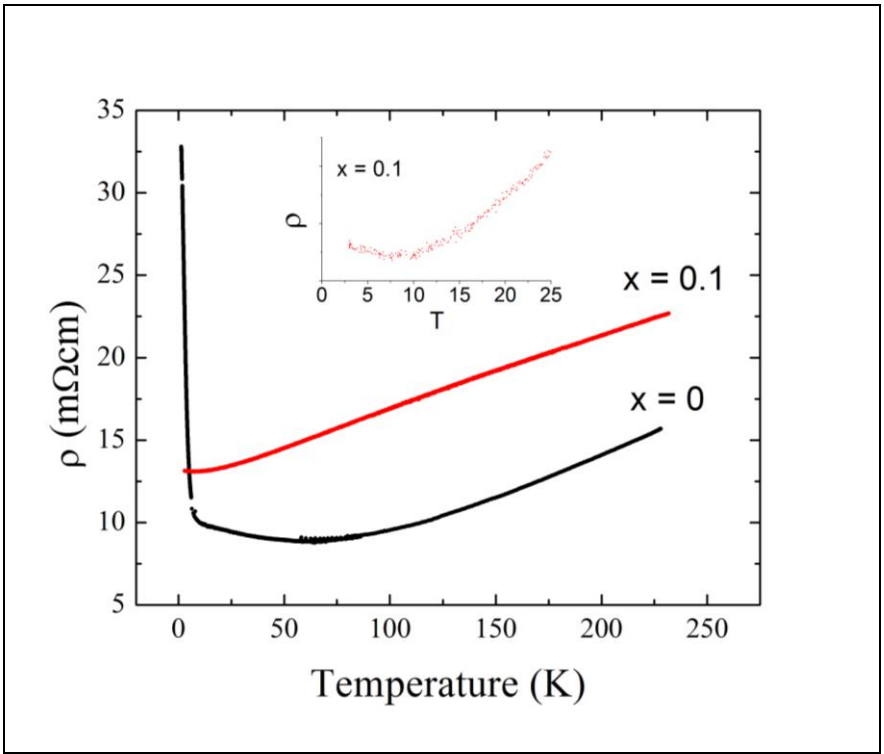

Figure 5.13 Temperature dependence of the resistivity for $x = 0$, and $x = 0.1$ from room temperature to ~2 K. The inset is a close up of the $x = 0.1$ curve below 25 K to highlight the minimum near 8 K.

The introduction of Ca temperature extends the temperature region over which the resistivity is found to have $d\rho/dT > 0$ meaning that the sample has clearly been made more metaillic. This suggests that we an increased carrier density or Fermi surface capable of supporting metallic behavior. It should not be surprising however, that due to the correlations present and importance of the oxygen levels in the conduction process that the resistivity does not obey the Fermi liquid like T^2 behavior.

Hall effect measurements were also performed on the $x = 0.1$ and $x = 0.06$ samples for fields up to 7 T following the full hysteresis loop 0 T → 7 T → -7 T → 7 T and for temperatures down to 2 K utilizing the Quantum design PPMS system. The Hall resistivity was determined by taking the anti-symmetric part of the resistive response for

both the positive sweep direction (Up) and negative sweep direction (Down) described previously, and is shown in Figure 5.14 for several selected temperatures. At temperatures above 10 K, the Hall resistivity is linear with field indicating there is no anomalous contribution to the signal. Below 10 K, we find deviation from the linearity in the Hall resistivity indicating contributions from the anomalous channel similar to that which occurs in the parent compound. From measurements at 2 K, we see that the Hall resistivity saturates at high fields, indicating a much smaller normal Hall coefficient when compared to the undoped material. Unfortunately, we do not have the resolution to determine precisely the slope of the resistivity with field needed to perform a similar analysis as that done in section 5.3.3. However, by performing a linear fit to this region we may estimate a lower limit for the density of charge carriers based on the maximum error in measured slope. Taking this value instead, we find a maximum carrier concentration of 1 x 10^{23} carriers/cm^3 or 13 carriers/Ir, which is enormously greater than the 0.01 electrons/Ir determined from our analysis in section 5.3.3. This value is far greater than the expected number of holes induced by Ca doping: assuming one hole-like carrier for each Ca ion, there should be approximately 0.04 holes/Ir. On the other hand, performing this analysis of the x = 0.06 compound we find 4x10^{21} holes/cm^3 or 0.27 holes/Ir, roughly an order of magnitude more than the 0.02 holes/Ir expected from our naïve addition of Ca-induced holes. This analysis shows that the dominant carriers have gone from electron-like to hole-like, in a very non-trivial fashion. Assuming the low concentrations to be well behaved, a cross-over between the electron and hole like behavior to occur at or below x = 0.02. Further studies involving small concentrations are

clearly necessary to elucidate the unusual carrier concentration dependence in this system.

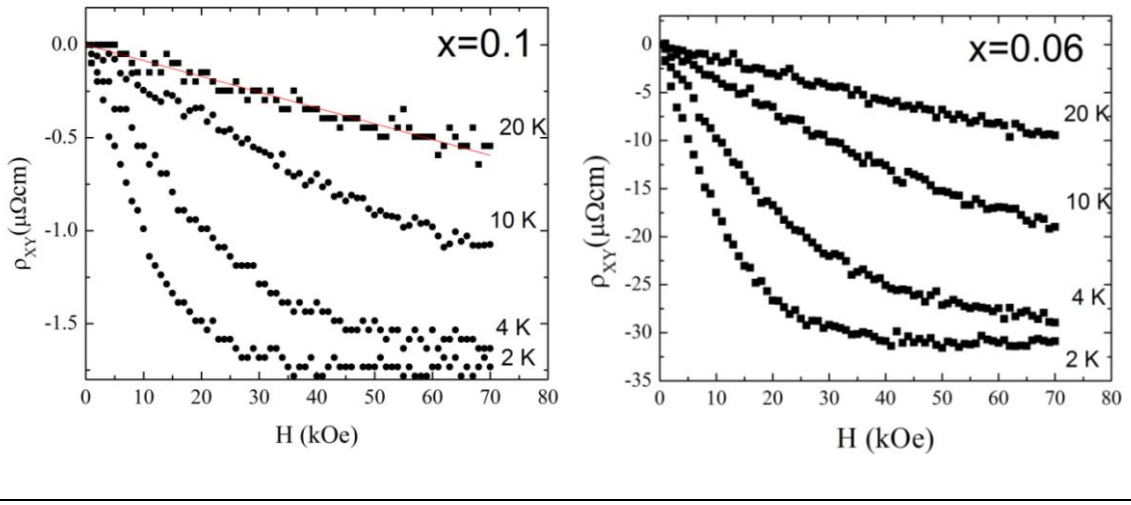

Figure 5.14 The field dependence of the Hall resistivity for Ca doped Nd-227 taken at multiple temperatures between 20 K and 2 K for (a) $x = 0.1$ and (b) $x = 0.06$

For comparison the data taken at 2 K for $x = 0$, 0.06 and 0.1 at 2 K have been plotted together in Figure 5.15. Interestingly we do not observe any hysteresis in either the $x = 0.06$ or 0.1, a striking result when compared to the dramatic hysteretic behavior observed in the $x = 0$ parent compound. We also do not observe any difference between the virgin zero-field cooled and the zero field data after sweeping the magnetic field to 7 T and back again to zero, also at odds with that observed in Nd-227 which was attributed to the formation of small ferromagnetic domains in the sample [15].

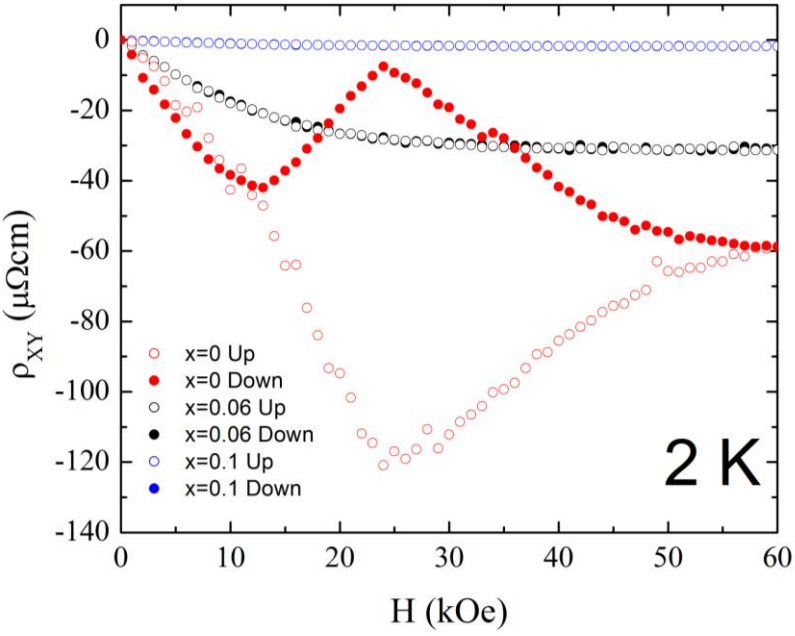

Figure 5.15 Field dependent Hall resistivity at 2 K for $Nd_{2-x}Ca_xIr_2O_7$ where x = 0, 0.06, and 0.1.

5.5.2 μSR

Muon spin relaxation measurements were performed for x = 0.10 and 0.06 samples at ISIS on the EMU spectrometer over the temperature range 1.6 K to 150 K, and for the x = 0.1 sample at PSI on the GPS and LTF facilities between 150 K and 20 mK. Samples were cut into disks roughly 1 mm thick and 6 mm in diameter and tiled in a mosaic fashion to maximize the filling fraction of the total beam spot size in order to reduce the background contribution from muons stopping in the sample holder and not in the sample.

Examining first at the data taken at ISIS, the depolarization data both samples were adequately fit by a single stretched exponential described by Eq. 5.1 for all

temperatures, with the initial asymmetry left as a fit parameter. In both samples the asymmetry was found to be constant to 4 K, below which roughly 5-10 % was lost due to the depolarization rate exceeding the limit of the detector. The relaxation rate λ and stretching exponent β extracted from this fit are shown in Figure 5.16. The depolarization rate shows a small increase in both concentrations near T_M, and maintains a constant value of $\lambda = 0.5\ \mu s^{-1}$ until 10 K, when the rate begins to increase dramatically; note that the enlarged error bars at low temperatures correspond to the region with reduced initial asymmetry. For both concentrations, the stretching exponent is near unity at high temperatures as expected for a simple paramagnet; shown in Figure 5.15(a) the $x = 0.06$ has an unusual non-monotonic behavior, as it drops slightly to 0.8 by 100 K, and then peaks near 10 K before rapidly dropping as the temperature is reduced. In Figure 5.16(b), we observe only a small bump in the β near 10 K. This parameter depends sensitively on the nature of the short time depolarization and is therefore susceptible to error due to the loss of initial asymmetry, thus while the value approaches 1/3, the value expected for a very disordered spin glass [18], this is not definitive proof a spin-glass state.

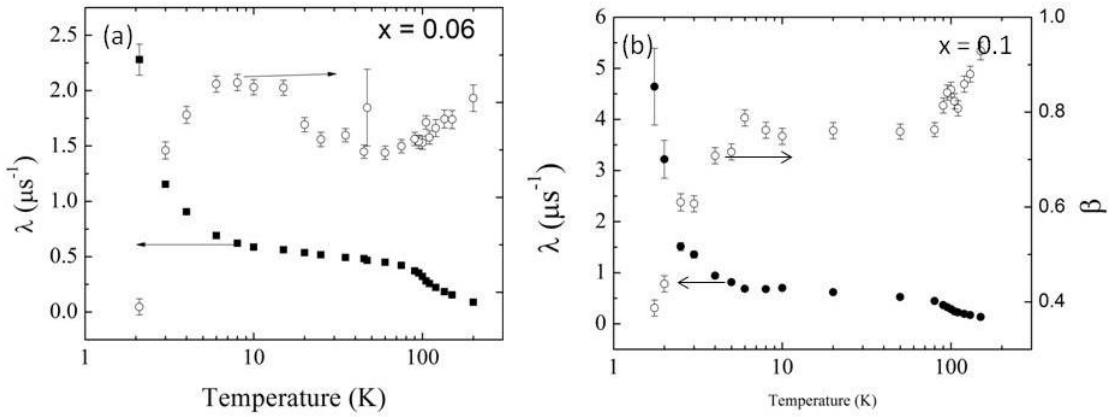

Figure 5.16 Temperature dependence of the λ and β for Ca doped Nd-227 taken on the EMU spectrometer at ISIS.

To better study the effects at short times, measurements were also performed on the $x = 0.1$ sample at PSI on GPS to 1.6 K and LTF to 20 mK. Example depolarization curves taken from GPS at 1.6 K for both $x = 0$ and $x = 0.1$ are shown in the inset of Figure 5.17. We observe no oscillation in the doped sample indicating there is no long-range order in any part of the sample, in contrast to the undoped case in which strongly damped oscillations are clearly visible. The data taken on GPS were fit with the same stretched exponential and yielded similar values to those extracted from ISIS measurements, however the asymmetry could be measured directly. Again, the depolarization rate does not saturate by the 1.6 K, the limit of the gas-flow cryostat in GPS. This indicates that the spin-fluctuations have not been fully quenched by this temperature but may be rapidly slowing down as the system enters the glassy state. The sample was then measured to 20 mK in LTF, again no spontaneous oscillations were observed even for an extended number of counts meant to improve the statistics necessary to observe coherent oscillations. This allows us to rule out the presence of any

long-range order in this sample at any reasonable temperature and instead favors the formation of a glassy disordered state.

The data was instead found to be best fit by the stretched exponential function described previously in Eq 5.1 and as used at higher temperatures. The depolarization rate is extracted from fitting data taken on both LTF and GPS to this function, and is shown in Figure 5.17, along with the data for the x = 0 sample reproduced here from Figure 5.5. We note that the gap in the data between T = 1.6 K and 0.8 K is due to the temperature limits of the gas flow and dilution cryostats; future measurements should be performed utilizing the new ^{3}He absorption cryostat at PSI to confirm the continuation of this curve, and to account for any offsets between detectors.

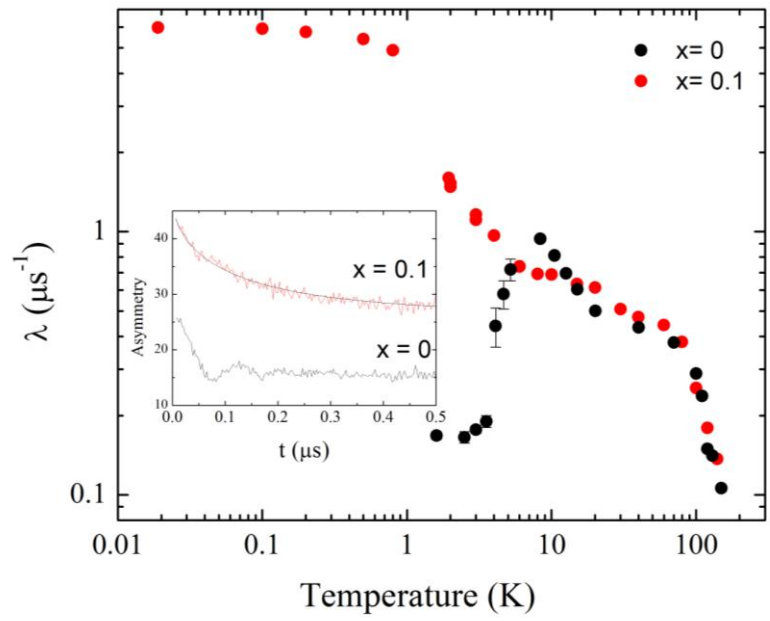

Figure 5.17 Comparison of the longitudinal relaxation rate determined from data taken at PSI for the undoped Nd-227 and Ca-doped with x = 0.1. INSET: the short time asymmetry for the two compounds at 1.6 K showing the damped oscillations in the parent compound and the lack thereof in the doped.

Shown in figure 5.17, the relaxation rate of both parent and doped sample exhibit similar temperature dependences to 10 K. Whereas the parent compound is found to magnetically order below this as shown in figure 5.6, no such ordering occurs in the Ca doped sample and the λ continues to increase, eventually saturating below 1 K with a maximum relaxation rate of 5 μs^{-1} at 20 mK and with a β of ~0.4. In a typical spin glass, the relaxation rate should approach a small value given by the distribution of static moments, as no dynamical modes should remain. As a probe of the relative static component, initial measurements of the longitudinal field dependence of λ were taken on EMU spectrometer at 1.6 K using fields up to 3 kG. The application of 3 kG suppresses the rate from 2 μs^{-1} to only 0.5 μs^{-1} which indicates that the relaxation is due to two separate components related to the quasi-static dynamical mechanism. If the relaxation were due to a static mode only, we would expect the muon to be completely decoupled from the static distribution with an application of a field greater than λ/γ ~ 150 G. However, as considerable relaxation occurs even in 3 kG, this implies then that considerable dynamical fluctuations are present in the system, which may be of quantum nature. This is roughly an order of magnitude larger than the persistent spin dynamics in Y-227 suggesting that these dynamics arise from a distinctly different mechanism.

The relaxation near T_M ~ 100 K does not appear to depend on the Ca concentration, which would indicate that the transition to the short-range ordered state argued previously is unaffected by the increase in carrier density. As this was expected to be on the order of the Ir-exchange interaction temperature, it is unclear why this remains unchanged when the filling fraction of the conduction bands are changed relative to the

undoped compound. Measurements of the bulk magnetization and susceptibility are imperative to understanding the nature of this transition.

5.5 Discussion of Charge Doping in Nd-227

By introducing divalent Ca as a doping element into Nd-227, we have shown that a tremendous number of hole-like carriers are added into the system. This is consistent with measurements on Y-227 was shown to become metallic for large Ca concentrations. Y-227 is in many ways much simpler, as the system begins as a Mott-like insulator with only the Ir moments contributing the magnetic order. Therefore, the effect of Ca in Y-227 is most similar to the canonical case of a doped Mott-insulator found in many other transition metal oxides, where in reducing the effective filling fraction of the $j = ½$ bands below half-filling we allow for increased mobility between Ir-sites, thus increasing the conductivity and reducing the propensity of the system to order magnetically [43]. In Nd-227 we find a more complicated system as, the system is already in a (weakly) metallic state in which the predominate carriers appears to be electron-like. As we have shown, the substitution of Ca introduces holes into the system in a very non-trivial way indicative of a complex band structure. Furthermore, this system is complicated in that Ca^{2+} is non-magnetic and substituting for a magnetic Nd^{3+} therefore we also add a small degree of disorder to the Nd sublattice in addition simply more carriers.

At high temperature the resistivity does not show any features near T_M indicating that the slight reduction or localization of the mobile charges does not occur as a result of the extrinsic carriers. As the onset of magnetism is closely related to the localization of the Ir electrons in the insulating compounds, we note that the metallic Ca-doped Nd-227

samples would exhibit signs of magnetism. This is clearly at odds with the results of our muon spin relaxation measurements, which indicates that a magnetic transition or slowing down of the fluctuations occurs at T_M. A possible explanation for this is the presence of magnetic domains near the interfaces of grains and surfaces which give rise to weak muon depolarization. This is supported by the microstructural similarity between doped and undoped samples as they fabricated in the same way and therefore have approximately equal grain sizes and other defect densities. I note that in initial magnetization measurements of a collection of single crystals of Nd-227 do not appear to show any features near T_M, however these samples have not been characterized by transport or other measurements. If further characterization can be performed, this would suggest that defects and grain boundaries may in fact play an important role in the development of the high-temperature magnetic state. Many additional measurements are required before this link may be more conclusively shown, therefore at this time we may only speculate as to the source of magnetism at this temperature in the doped and undoped compounds.

I now move to the low temperature state as probed by Hall effect and muon spin relaxation. While we have shown from Hall effect measurements that there are substantially more carriers in the doped system than in the undoped system, the resistivity of the two compounds remains similar; this is quite unusual as it means that the average collision time must decrease proportionally to balance the additional carriers. This could be the result of additional magnetic fluctuations or disorder induced by the Ca doping, however such an explanation is merely speculative at this time. These results may also be interpreted within the framework of a Kondo-lattice system, in which an array of *f*-

electron atoms (such as Nd) interacts with a bath of conduction electrons with a density of states ρ via a coupling energy *J*. These conduction electrons act to screen the local magnetic moments, forming a many-body singlet state below the Kondo temperature with a typical energy scale $T_K \sim J^2\rho$. On the other hand, these conduction electrons also mediate the exchange between the localized and otherwise weakly interacting rare-earth moments via the RKKY interaction with energy scale $T_{RKKY} \sim \exp(-1/2J\rho)$. Increasing the density of states increases both T_K and T_{RKKY}, however not necessarily equally [44]. Therefore, it is possible that by doping in additional carriers the Nd-magnetic moments are more effectively screened, thus reducing their interaction with and preventing the formation of the spin-ice state found in the undoped compound. Because the moments are constrained to a non-coplanar structure, it is possible that the magnetic moments give rise to a chiral field which produces an AHE at low temperatures, as suggested by Ref. [Flint], indicating that the doping has produced a state similar to Pr-227. An interesting test of this mechanism would be to substitute the Nd^{3+} site with a large 4+ element such as Te, to electron-dope the system at a comparable level.

Recent measurements by Matsuhira *et al* on insulating variants of Nd-227 have found a similar high field hysteresis in the Hall effect and magnetization to that which we observed in the weakly-metallic samples [15]. For spin-ice states to exist in both our samples and those measured by Matsuhira, the nearest neighbors Nd^{3+} moments must have a net FM interaction between them [34]. This would seem to argue against a conduction electron mediated interaction between Nd^{3+} ions, as the sign of the RKKY interaction between nearest neighbor moments oscillates dramatically as a function of the carrier concentration. This would indicate that the simplified parabolic and single-band

model which we have used to determine the carrier concentration and therefore Fermi wavevector is either egregiously inadequate or the net *f-f* interaction is not driven by conduction electrons at all. One could also speculate that the lack of such hysteretic behavior in the Ca-doped samples due rather to the non-magnetic impurities on the Nd-sublattice; however as the spin-ice state is already a degenerate state lacking true long-range order, it is difficult to interpret how such impurities would induce further disorder. In either case, Hall effect and magnetization measurements to much lower temperatures are necessary to look for any signs of other unusual behavior which may signal the existence of any such chiral spin state and to distinguish it from a simple spin-glass system. Specific heat measurements of the doped compounds should also be done to estimate of the effective electron mass which would provide a measure of the strength of the Kondo-type coupling between conduction electrons and the localized Nd moments.

5.6 Conclusions

In summary, we have studied high quality polycrystalline Nd-227 via a number of different magnetic probes. Our combined results reveal that this compound is in fact a complex precursor phase in the *A*-227 series at the boundary between the proposed metallic spin liquid phase in Pr-227 and the long-range magnetically ordered insulating phase. We have determined several different energy scales given by T_{LRO} and B_c related to the appearance of magnetic order, and T_M which is related to the appearance of a macroscopic moment without long-range order. Analysis of the spontaneous local field determined from muon spin measurements indicates that the Nd^{3+} sublattice cannot occupy the AIAO configuration, and suggests that the spontaneous precession instead

results from an ordered Ir^{4+} sublattice. The striking similarities of our results to those for other spin-ice systems suggests that the Nd sublattice in the weakly metallic regime of Nd-227 has a two-in/two out rather than all-in/all-out magnetic structure potentially. Introducing additional mobile charge carriers and defects through calcium substitution removes the formation of magnetic order and the high-field energy scale, and suggests that the Nd sublattice no longer occupies a well defined 2I2O spin-ice configuration. Measurements of the Hall effect and magnetization to much lower temperatures are necessary to determine if the chiral state found in Pr-227 is manifest in these compounds as well

Chapter 5 References

[1] S. M. Disseler, Chetan Dhital, T. C. Hogan, A. Amato, S. R. Giblin, Clarina de la Cruz, A. Daoud-Aladine, Stephen D. Wilson, and M. J. Graf, Phys. Rev. B **85**, 174441 (2012).

[2] S. M. Disseler, S. R. Giblin, Chetan Dhital, K. C. Lukas, Stephen D. Wilson, and M. J. Graf. Phys. Rev. B **87**, 060403(R) (2013).

[3] D. Pesin and L. Balents, Nature Physics **6**, 376 (2010).

[4] X. Wan, A. M. Turner,A. Vishwanath,and S. Y. Savrasov, Phys. Rev. B **83**, 205101 (2011).

[5] W. Witczak-Krempa and Y. Kim, Phys. Rev. B **85**, 045124 (2012).

[6] K. Matsuhira, M. Wakeshima, Y. Hinatsu, and S. Takagi, J. Phys. Soc. Jpn. 80 094701 (2011).

[7] S. M. Disseler, Chetan Dhital, A. Amato, S. R. Giblin, Clarina de la Cruz, Stephen D. Wilson, and M. J. Graf, Phys. Rev. B **86**, 014428 (2012).

[8] S. Nakatsuji, Y. Machida, Y. Maeno, T. Tayama, T. Sakakibara, J. van Duijn, L. Balicas, J. N. Millican, R. T. Macaluso, and J. Y. Chan, Phys. Rev. Lett. **96**, 087204 (2006).

[9] T F Qi1, O B Korneta, Xiangang Wan, L E DeLong, P Schlottmann and G Cao, J. Phys. Cond. Matter **24** 345601 (2012).

[10] D. Yanagishima and Y. Maeno, J. Phys. Soc. Jpn. **70**, 2880 (2001).

[11] K. Matsuhira, M. Wakeshima, R. Nakanishi, T. Yamada, A. Nakamura, W. Kawano, S. Takagi, and Y. Hinatsu, J. Phys. Soc. Jpn. **76**, 043706 (2007).

[12] M. Sakata, T. Kagayama, K. Shimizu, K. Matsuhira, S. Takagi, M. Wakeshima, and Y. Hinatsu, Phys. Rev. B **83**, 041102(R) (2011).

[13] K. Tomiyasu, K. Matsuhira, K. Iwasa, M. Watahiki, S. Takagi, M. Wakeshima, Y. Hinatsu, M. Yokoyama, K. Ohoyama, and K. Yamada, J. Phys. Soc. Jpn. **81** 034709 (2012).

[14] U. Walter, J. Phys. Chem Solids. **4,** 401 (1984).

[15] K. Matsuhira, M. Tokunaga, M. Wakesima, Y. Hinatsu, S. Takagi. J. Phys. Soc. Jpn. **82** 023706 (2013).

[16] M. C. Shapiro, S. C. Riggs, M. B. Stone, C. R. de la Cruz, S. Chi, A. A. Podlesnyak, and I. R. Fisher, Phys. Rev. B **85**, 214434 (2012).

[17] S. Zhao, J. M. Mackie,D. E. MacLaughlin,O. O. Bernal,J. J. Ishikawa,Y. Ohta,and S. Nakatsuji, Phys. Rev. B **83**, 180402(R) (2011).

[18] A. Yaouanc and P. Dalmas de Réotier *Muon Spin Rotation, Relaxation, and Resonance : Applications to Condensed Matter*, (Oxford University Press, Oxford, 2011).

[19] Y. Machida, S. Nakatsuji, S. Onoda, T. Tayama, T. Sakakibara, Nature **463** 210 (2010).

[20] D. E. MacLaughlin, Y. Ohta, Y. Machida, S. Nakatsuji, G. M. Luke, K. Ishida, R. H. Heffner, Lei Shu, and O. O. Bernal, Physica B **404**, 667 (2008).

[21] L. Balicas, S. Nakatsuji, Y. Machida, and S. Onoda, Phys. Rev. Lett. 106, 217204 (2011).

[22] P. J Baker, J. S. Moeller, F. L. Prattrm W. Hayes, S. J. Blundell, T. Lancaster, T. F. Qi, G. Cao. arXiv 1302.6905 (2013).

[23] A. Ikeda and H. Kawamura J. Phys. Soc. Jpn. **77**, 073707 (2008).

[24] C. Krey, S. Legl, S. R. Dunsiger, M. Meven, J. S. Gardner, J. M. Roper, and C. Pfleiderer, Phys. Rev. Lett. **108**, 257204 (2012).

[25] Y. Kohama, C. Marcenat, T. Klein, M. Jaime. ArXiv 1003.3184 (2010).

[26] M.A. Ruderman and C. Kittel, Phys. Rev. **96**, 99 (1954)

[27] W. R. Branford, S. Ladak, D. E. Read, K. Zeissler, L. F. Cohen, Science **335** 1597 (2012).

[28] N. Nagaosa, J. Sinova, S. Onoda, A. MacDonald, N. P. Ong, Rev. Mod. Phys. **82,** 1539 (2010).

[29] S. J. Blundell, A. J. Steele, t. Lancaster, J. D. Wright, F. L. Pratt. Physics Procedia **30** 113 (2012).

[30] G. Sala, C. Castelnovo1, R. Moessner, S. L. Sondhi, K. Kitagawa, M. Takigawa, R. Higashinaka, and Y. Maeno. Phys. Rev. Lett. **108**, 217203 (2012)

[31] R. Aldus, S.T. Bramwell, S. Calder, T. Fennell, S.R. Giblin, and D. Prabhakaran, Nature **461** 7266 (2009).

[32] S. R. Dunsiger , A. A. Aczel, C. Arguello, H. Dabkowska, A. Dabkowski, M.-H. Du, T. Goko, B. Javanparast, T. Lin7, F. L. Ning, H. M. L. Noad, D. J. Singh, T. J. Williams, Y. J. Uemura, M. J. P. Gingras, and G. M. Luke. Phys. Rev. Lett. **107**, 207207 (2011).

[33] G. Chen and M. Hermele, Phys. Rev. B **86,** 235129 (2012).

[34] S. T. Bramwell, M. J. Harris, J. Phys. Condens. Matter **10**, L215 (1998)

[35] M. Udagawa and R. Moessner, ArXiv 1212.0293v1 (2012).

[36] H. Ishizuka and Y. Motome, Phys. Rev. B **87,** 081105 (2013).

[37] F. F. Tafti, J. J. Ishikawa, A. McCollam, S. Nakatsuji, and S. R. Julian, Phys. Rev. B **85** 205104 (2012).

[38] M. Udagawa, H. Ishizuka, and Y. Motome, Phys. Rev. Lett **108**, 066406 (2012).

[39] G. Chern, S. Maiti, R. M. Fernandes, P. Wolfle ArXiv 1210.3289v1 (2012).

[40] R. Flint and T. Senthil. Phys. Rev. B **87** 125147 (2013).

[41] H. Fukazawa, Y. Maeno. J. Phys. Soc. Jpn. **71** 2578 (2002).

[42] http://www.webelements.com/

[43] P. Fazekas, *Lecture Notes on Electron Correlations and Magnetism*, (World Scientific Pub Co Inc, New York 1999)

[44] A. Hewson. *The Kondo Problem to Heavy Fermions*. (Cambridge University Press, Cambridge UK 1993).

Chapter 6: Discussion

The previous chapters have described in great detail experimental results for several members of the pyrochlore iridate family of compounds with some discussion of their implications regarding specific questions contained within each chapter. The goal of this chapter is to incorporate all of the previous results in a more general framework with a focus on answering the broader questions regarding the evolution of magnetism within the pyrochlore iridates series, and the new questions this work raises. I will begin by briefly summarizing the key conclusions of each chapter, then move on to discussing the evolution of the ground state magnetism in this series, including the newly discovered intermediate short-range magnetism; lastly I will discuss the implications of these results on some current theoretical models and how they may constrain the possible phase diagrams predicted by these studies.

6.1 Summary of Results

As a means of providing context for the remainder of this chapter, it is useful to first concisely summarize the findings presented in Chapters 4 and 5. As we have seen, measurements of the electrical transport and magnetization properties of Yb-227 and Y-227 in Chapter 4 indicated that these materials are Mott-like, with a semi-metal to insulator cross over observed at 130 K and 150 K for Yb-227 and Y-227 respectively. From our μSR measurements on these compounds we find well-defined spontaneous oscillations of the muon asymmetry below 130 K in Yb-227, indicative of commensurate long-range magnetic order. Similar oscillations are observed in Y-227 below 150 K; however, the onset of hysteretic magnetization at T = 190 K indicates a transition to an intermediate magnetic state lacking long-range order. The proximity of the maximum local fields in Y-227 and Yb-227, together with similarities of the critical exponents extracted from our analysis, show that these two iridates have nearly identical magnetic ground states consisting of an all-in/all-out ordered Ir-sublattce. Furthermore it is clear that the presence of magnetic *A*-site species does not play any significant role in altering the ground-state properties of the Ir-sublattice. Extending our μSR measurements to 20 mK on Yb-227 have suggested that the Yb-sublattice is strongly polarized by the resulting ordered Ir moments, and in fact may order or form a more exotic quantum state below roughly 1 K.

Unlike Y-227 and Yb-227 which were strong insulators, $Nd_2Ir_2O_7$ (Nd-227) is weakly metallic with Kondo-like behavior below 10 K including logarithmically increasing resistivity with decreasing temperature and strong negative magnetoresistance varying linearly with the square of the magnetization. Susceptibility and μSR

measurements indicate two distinct temperature scales which correspond with the onset of short-range order or glass-like behavior at T_M = 105 K and long range order below T_{LRO} = 8 K. The local field profile extracted from our μSR measurements is quite different from the insulating Yb-227 or Y-227, and indicates substantial disorder in addition to a greatly reduced net local field.

Detailed measurements of the Hall effect and magnetization in Nd-227 reveal two independent hysteretic effects centered near B = 0 and B_c = 2.6 T which are found to occur below T_M and T_{LRO} respectively. Measurements of the magnetocaloric effect on this compound show a large increase in the sample temperature as the field is swept through B_c which indicates that the high field state is of much lower entropy than that found in zero-field. Based on a comparisons with other relevant systems, these results suggest that the Nd-sublattice occupies a similar degenerate (2I2O) state like $Pr_2Ir_2O_7$ (Pr-227), while the Ir-sublattice orders in a similar fashion to that of the insulating compounds. Substituting calcium into the system induces both additional hole-like carriers as well as disrupts the magnetic sublattices. Zero field μSR results reveal the long range order found in the parent compound is fully removed by the substitution of only 5 % Ca for Nd, indicating the precariousness of the ordered state.

6.2 Evolution of the Magnetically Ordered State

I begin the discussion with the observation of spontaneous muon precession in Y-227, Yb-227 and Nd-227. Combined with the previous results by Zhao *et al.* [1] this indicates that long-range order is ubiquitous in all insulating compounds and extends into

the weakly metallic region of the phase diagram described by Matsuhira [2]. Furthermore, based solely on the extracted values of the local fields from μSR measurements we have shown that changes in the crystalline structure which occur as the radius of the rare earth is increased across the series do not alter the effective interactions between Ir-moments enough to change the ground state magnetic structure, at least in the insulating compounds. The same can be said of the effects of the large localized rare earth moments, since the behavior of the local field near the transition temperature in Yb-227 was found to be identical to Y-227 and Eu-227. Unfortunately we cannot determine the unique configuration of the magnetic moments from our μSR measurements alone in the manner that can be extracted from neutron scattering, for example. However, by examining the results from all of our available techniques we may systematically eliminate many possible ground states, which I will now discuss. To begin with we take as possible states those listed by Wan *et al.* [3] which were discussed in Chapter 4, and include the non-coplanar all-in/all-out and two-in/two-out or spin ice states, ferromagnetic alignment along either the [100] or [111] directions, and indirect Dzyaloschinski-Moriya or IDM state. Based on our magnetization hysteresis measurements, we have ruled out the presence of any ferromagnetic state as the resulting remnant moments are far too small to be created by such a state, and instead are likely due to either surface magnetism or canting of the moments in an AFM state. Simulations of the magnetic fields in Y-227 have rule out the IDM state as these produce fields which are far smaller at the most likely muon stopping sites to be applicable, and in addition this should produce $Q \neq 0$ reflections which should be observable in neutron scattering if the Ir moment is greater than 0.2 μ_B/Ir. Therefore, this leaves the degenerate two-in/two-out

and antiferromagnetically ordered all-in/all-out. The degeneracy of the two-in/two-out structure should prevents the formation of a local field with a fixed wave-vector meaning no coherent muon oscillations should be observed. As we clearly have a single well defined spontaneous frequency of oscillation we may definitively rule out the spin-ice configuration as a possible state on the Ir-sublattice as well. Therefore, at least on the Ir-sublattice, we find that the magnetic configuration is all-in/all-out structure. While this logic can be applied to all of the insulating compounds, in the case of Nd-227 we cannot simply assume that the order is on the Ir-sublattice alone. The local field is quite different from that observed in Y-227 and Yb-227, indicating that the Nd moments may play a substantial role in the ground state magnetic structure. However, as was described in great detail in Chapter 5, our neutron scattering measurements have shown that there is no long-range order which leads to either new Bragg peaks or enhancement of nuclear peaks, and the use of Bayes theorem to study the moment distribution in this compound has completely precluded the existence of the all-in/all-out order on the Nd sublattice. Therefore, it appears that in all pyrochlore iridates which order magnetically, the all-in/all-out state of the Ir^{4+} moment is the preferred configuration for all A-227 compounds which magnetically order.

Parallel studies via resonant diffraction (RXD) measurements were recently performed on Eu-227 by Sagayama et al. which more directly probe the magnetic transition on the *Ir* sites [4]. By using diffraction measurements only at the L_3 edge, they have confirmed that the insulating compound Eu-227 is magnetically ordered below the bifurcation. More importantly, these results have found that out of the manifold of possible states which have a $Q = (0\ 0\ 0)$ ordered wavevector, only one doesn't produce a

structural distortion which should be observed by RXD, which is the all-in/all-out configuration. This confirms our initial result of such a state in Y-227, as well as the remainder of the insulating compounds. However, again the situation is less well defined in the case of metallic Pr-227 and Nd-227, where the magnetism of the Nd and Pr sublattices clearly plays a more important role in the overall magnetic ground state. This primarily stems from our lack of understanding regarding the evolution of the metallic 'chiral' state from the magnetically ordered insulating state as the rare earth radius is reduced.

As a means of providing insight into this problem, we have plotted the maximum precession frequency extracted from ZF-μSR measurements taken in References [1, 5-8] and plotted them as a function of the A-site radii. It should be noted that while Pr-227 does exhibit strong depolarization, no spontaneous precession is observed, thus the frequency is shown here as zero. Recent studies recent studies of metallic $Bi_2Ir_2O_7$, with an ionic radius ~117 pm, support an unquenched Ir -moment in the metallic state as weak quasi-static magnetism is observed at low temperatures, which can only stem from the Ir-sublattice as Bi^{3+} is nonmagnetic [9]. Extracting the approximate width of the local field from these measurements it was estimated that the local moment in Bi-227 is over two orders of magnitude smaller that found in Y-227. This would naturally suggest that the Ir-sublattice retains a magnetic moment in Pr-227 as well; however the signal is likely overwhelmed by the much larger background of the disordered Pr-moments. This figure indicates that the local field changes continuously across the series, rather than a sharp drop from magnetically ordered (A = Eu) to disordered (A = Pr). If so the long-range ordered moment is not suddenly quenched or reoriented in the metallic state, but is rather

gradually reduced as the A-site radius is increased. This comparison further supports our original supposition that Nd-227 is a unique cross-over compound, with an ordered Ir-sublattce and disordered (or frozen) Nd-sublattice. Future measurements on the remainder of the series, particularly Sm-227 which has an A-site radius which lies between Eu and Nd are important to further understand this apparent trend.

Unfortunately there remains a rather dramatic change in the magnetic state as we go from Nd-227 to Pr-227, and there are no isovalent elements which have radii which lie between Nd and Pr. Therefore we cannot stoichiometrically probe the evolution of the local field from Nd-227 to Pr-227. In chapter 5 I discussed our attempts to probe this difference via the introduction of additional mobile charges into Nd-227. In doing so we found that the long-range order in Nd-227 was completely removed, and a disordered ground state made up of both quasi-static and dynamical modes found to 20 mK. This behavior is similar to that observed in Bi-227 in which also showed no signs of magnetic order [Baker] and remains metallic with a hole-like carriers determined from the low-field Hall measurements [10]. Calculations of the electronic band structure in Bi-227 indicate that both hole-like and electron-like bands cross the Fermi-level which sits at a very sharp peak in the density of states. In Bi-227 this peak results from the hybridization of the Bi 6*p*-levels, which according to Qi *et al* results in partial screening of the correlation interaction and leads to an increased itinerancy of the Ir magnetic moments [10]. Doping away from the original Fermi level in Nd-227 may result in similar phenomena, in which we have increased the itinerancy of the moments which would reduce the average size of the magnetic moments and the ordering temperature [11].

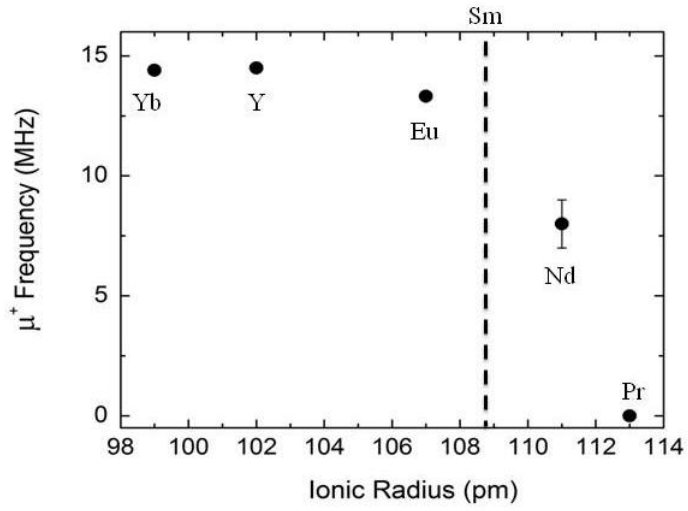

Figure 6.1 The maximum ZF muon spin precession frequency extracted from References [1, 5-8]. The dashed line is provided solely as a guide for the eye.

While it is clear that the variation of the *A*-site radius alone is enough to induce changes in the magnetic and electrical ground state of the system, one of the primary questions which remain in this series is the mechanism by such substitution causes this to occur. Our results clearly show that it is not the magnetic or orbital configuration of the *A*-ions which drive this process; rather the more likely culprit are subtle distortions of the crystalline structure which result from varying the radius of the *A*-species. There are several important structural parameters which could have an effect on the local *Ir* environment which are found to vary as a function of the *A*-radius: the lattice constant *a*, the compression of the oxygen octahedra (from the O-48f positions) *x,* and the distance from each *Ir* to the nearest neighbor *A*-sites. There is considerable discourse on how changes in each of these give rise to the observed behavior in this system [12-14]; while

our results certainly do not resolve this conflict, they do provide additional information which favors one over the other.

We first examine the relation of the ground state to the size cubic lattice parameter *a*. First shown by Maeno and Yanagishima [15], and later confirmed in this work, we note that the lattice parameter tracks linearly with the radius of the A-ion, which as we have seen greatly increases the electrical conductivity at low temperatures. Applying external hydrostatic pressure to any of the compounds should reduce the size of the lattice, making it more insulating. However, what is actually observed is that in measurements of both Nd-227 [16] and Eu-227 [17], the application of external pressure pushes these systems from insulating to metallic ground states. Therefore it has been shown that the external pressure works similarly to increasing the size of the rare earth radii, and while appealing for its simplicity, the lattice parameter simply cannot be the determining factor.

Unlike many of the other iridates of interest, which are layered perovskite materials in where the CEF at the iridium site is determined totally by the local oxygen octahedra, in the pyrochlore structure each Ir^{4+} is also surrounded by a hexagonal ring of A^{3+} ions which clearly break the local cubic symmetry of the octahedra. Therefore, one may assume that due to the extended nature of the Ir-5d orbitals these non-cubic charge configurations could have a rather strong affect on the actual spacing of the t_{2g} levels. Using resonant inelastic x-ray scattering (RIXS) measurements on Eu-227 and Y-227, Hozoi et al recently indicated a significant CEF acting within the t_{2g} manifold, which acts to quench the orbital angular momentum [14]. By comparison of the measured energy levels with DFT calculations, they suggested that hexagon arrangement of A^{3+} plays a

more important than small trigonal distortions considered previously. One would expect then significant differences between Eu-227 and Y-227 as the CEF due to the *A* ions should increase with decreasing Ir-A distance which is proportional to the lattice parameter. Currently the resolution of the x-rays is limited to around 300 meV based on the FWHM of the beam energy, meaning that the small changes (expected to be around 10 meV from DFT calculations) cannot be readily observed by this technique. Because of this, RIXS is only able to probe the energy differences between the (mostly) j = 3/2 and (mostly) j = ½ states or transitions to the unfilled e_g states, and cannot reveal any information about the splitting between the individual j = ½ levels as a result of correlations. Therefore, we cannot completely rule out the effect of the A-site charges in mediating the observed behavior.

We last discuss the role of the trigonal distortions to the CEF environment produced by the oxygen octahedra surrounding each Ir. In the limit of large trigonal distortions, temporarily neglecting the SOI, the t_{2g} triplet states are split into upper e_g' doublet and a lower a_{1g} singlet (both doubly degenerate) [Kim 2010]; while on the other hand, the SOI will split the t_{2g} into a lower lying j = 3/2 quartet and a j = 1/2 doublet. Beginning from the SOI state, we find that increasing the trigonal distortions will cause the actual ground state wavefunction to be an admixture of the j = 3/2 and j = 1/2 levels. This will inevitably increase the effective bandwidth of the system, and may induce metallic behavior for sufficiently large distortions. This effect has been studied in great detail in the layered perovskites Sr_2IrO_4 (Sr-214) and $Sr_3Ir_2O_7$ (Sr-327) utilizing various x-ray scattering and absorption techniques. These materials are strongly insulating at low temperatures, with a tunneling gap measured via scanning tunneling microscopy to be as

much as 600 meV in Sr-214 [18] and 150 meV in Sr-327 [19]. In Sr-214, the trigonal distortion is estimated to be on the order of 75 meV, which is much smaller than the SOI-induced gap of approximately 0.4 eV. RIXS and x-ray absorption have indicated that applying large external pressure to the system leads to an increased $j = 3/2$ character of the ground state wavefunction, increasing the conductivity at low temperatures. Therefore it is assumed that this pressure strongly distorts the cubic environment, increasing the trigonal field upwards of 200 meV [20].

Yang and Kim used a tight-binding approach including the trigonal distortions to model the effective band structure of the $j = 1/2$ states only [12]. They found a gapped $j =$ ½ band can be closed to form a metallic (or semi-metallic) state through increased distortions, which act to change the relative hopping magnitudes between different pathways between *Ir* sites. There was no mention on the effect of magnetic order, or on the size of the Ir moment in this work, however. Early x-ray diffraction measurements by Tiara *et al* have in fact shown that *x* parameter depends on the *A*-site radii with larger *A*-ions having larger vales of *x;* however oxygen has a small x-ray cross section so detailed parameters have significantly more error than other atomic coordinates. Using neutron scattering, which is much more sensitive to the positions of oxygen atoms, our measurements have confirmed that this parameter does in fact change by several percent between Y-227 and Nd-227, with Nd-227 being the more distorted of the two. Such analysis has yet to be performed by other groups who also recently fabricated a complete series of compounds [2], therefore it is unknown if this phenomenon is ubiquitous in this series or depends on details of the synthesis.

It is unknown if this level of distortion is enough to cause significant mixing of the $j = 3/2$ level, however the apparent reduction of the magnetic moment and increased conduction would suggest that this is the case. A more convincing argument would be to examine the evolution of this parameter as function of applied pressue in either single crystals of Nd-227 or Eu-227 of which transport studies have been performed.

6.3 Short-Range Ordered State

One of the most unexpected results was the presence of an unusual magnetic state in both Y-227 and Nd-227 over temperature range $T_M > T > T_{LRO}$. There are several possible scenarios which could lead to this type of behavior which were mentioned in the previous chapters, and will be discussed in greater detail now. The first possibility is that the long-range order does in fact appear at T_M , that is $T_M = T_{LRO}$, however because of thermal or quantum diffusion the muons are sampling many different magnetic sites and thus do not observe a static ordered field. This process was recently theorized to explain several phenomena including the persistent dynamic relaxation in the pyrochlore titanates $Dy_2Ti_2O_7$ [21], however recent measurements of the non-magnetic $Y_2Ti_2O_7$ [22] appear to question this result. More importantly, this does not explain our magnetization measurements which indicate that this transition occurs on a macroscopic level. Therefore, the intermediate state is not a result of diffusive or structural changes induced by the muons but is in fact an intrinsic effect.

Ruling out diffusive processes, there are two magnetic phenomena which may explain behavior observed in this region that were mentioned in the preceding chapters.

The first possibility mentioned was the entrance into a spin-glass state, while the latter was the formation of short-range order. There is some evidence to both support and cast doubt as to the presence of each of these possibilities which I will upon, beginning with the spin-glass state.

A common feature of canonical spin-glass materials is the bifurcation of the susceptibility as we have observed, which is due to the distribution of ferromagnetic interactions between some magnetic moments which may be biased into yielding a small net moment when cooled in a finite magnetic field. The closely related series of pyrochlore molybdates, particularly $Y_2Mo_2O_7$ [23] has in fact proven to be a canonical spin-glass via extensive magnetization, ac-susceptibility and muon spin measurements, even though there does not appear to be site or bond disorder in the crystal, similar to the pyrochlore iridates. Detailed measurements by several groups [24,25] using extended x-ray absorption fine structure (EXAFS) and an analysis of the pair-distribution function (PDF) taken from neutron scattering at large moment transfers, have found that the spin-glass behavior is likely mediated by anisotropic bond-disorder of the Y-O and M-O bonds which affect the super-exchange interactions between nearest neighbor Mo ions. Sanders and Chalker showed that small spatial variations of the average exchange energy can lead to long-range interactions capable of generating such glassy states, particularly on the pyrochlore lattice [26]. Currently, we cannot rule out such localized distortions in the iridates as they do not cause global structural distortions. However an important point of this mechanism shown by Sanders and Chalker is that the size of the disorder should be small compared to the average exchange and the freezing temperature should scale with the disorder. This implies that for $Y_2Mo_2O_7$ which has a freezing temperature

T_f = 22 K the approximate scale of the disorder in the exchange interaction is roughly 20 K compared to a Curie tempearture of roughly 200 K. On the other hand, in $Y_2Ir_2O_7$ such disorder would an order of magnitude larger, nearly 180 K. While the former could be said to be in the limit of small disorder, this can simply not be the case for $Y_2Ir_2O_7$. Therefore although appealing, the intermediate temperature state is not likely driven by such small displacements of the local atoms within the unit cell. Experimentally, we do not observe other tell-tale signs of canonical spin-glass behavior such as a diverging depolarization rate at the freezing temperature in μSR, for example. Therefore, it is unlikely that this intermediate state is a true spin-glass.

The other possibility mentioned in the previous chapters, is the onset of short-range order (SRO) preceding the entrance into a long-range ordered state with decreasing temperature. As this is a rather subtle concept it is worth describing in more detail here. The SRO phase is defined by a state with a small but finite correlation length which does not diverge as the temperature is reduced, as is necessary to be considered a true thermodynamic phase transition [27, for example]. It is typically found in the region $T_N < T < J$, with T_N the transition (here Neel) temperature and J being the dominant exchange or order-mediating interaction [28, 29]. This type of behavior is often found as the result of frustrated geometries, and has been observed in numerous triangular lattice compounds such as $NiGa_2S_4$ [30] and BaVS3 [31]. In both studies, μSR measurements revealed a slightly increased longitudinal relaxation rate coinciding with a decrease in the stretching exponent, indicating the onset of multiple relaxation channels prior to the entrance into a long-range ordered state at much lower temperatures. This state has been observed in some pyrochlores as well, for example $Gd_2Ti_2O_7$ enters a short-range ordered state below

30 K, with long-range order developing below 1 K based on heat capacity, magnetization and susceptibility measurements [32]. Unfortunately, the best way to prove the existance of the SRO state is by extracting the correlation length from neutron scattering which cannot be done in for samples. For the muon to exhibit coherent spontaneous precession the correlation length should extend over several unit cells, implying a correlation length of no less than 20-30 Å. However in many systems, including those mentioned above, the correlation lengths in the SRO phase can be on the order of 5 Å which would not be observed in our muon relaxation studies. Comparing the accumulated results of Chapters 4 and 5 with those reported in the above mentioned systems, it is therefore much more likely that the pyrochlore iridates enter a region of short-range order above the long-range order transition temperature rather than a canonical spin-glass. As we observe this behavior in both Y-227 and Nd-227 we further claim that the short-range order in this region must therefore be stem from the Ir-sublattice rather than the A-site sublattice. I also note the trend that this SRO state appears to be stabilized with increasing A-site radius, as it is non-existent in the smallest compound (Yb-227), stable for ~30 K in the middle of series (Y-227) and appears to exist for over 100 K by Nd-227. Based on the discussion in the previous section, this state may therefore be related to the distortion of the oxygen octahedra with increasing A-site radius as well.

6.4 Implications for Topological States and Other Models

The potential for new type of topological states, such as the so-called Weyl semi-metal and axion insulator state in the pyrochlore iridates has driven much of the recent theoretical development in these materials, however up to this point there has been very

little evidence for their existence. As noted by Balents and others, one of the necessities for the development of the Weyl semi-metal, for example, is the spontaneous breaking of either inversion or time-reversal symmetries, but not both. Because of the cubic symmetry and frustrated nature of the pyrochlore structure, very few of the possible magnetic configurations preserve this combination of symmetry therefore it is important to discern the proper magnetic ground state of the system. Fortunately the all-in/all-out configuration does in fact meet these criteria, and as we have shown, is the dominant structure in the Ir sublattice for a wide range of *U/t*. While our measurements cannot infer the presence of any exotic topological states, our measurements support at least one of the criteria necessary its existence. To date, the only attempt at directly observing the Weyl state has been found in optical conductivity measurements of Rh-doped $Nd_2(Ir_{1-x}Rh_x)_2O_7$ in which a continuous reduction in the charge gap with increased doping was observed. For critical concentration near $x \sim 0.02$ the gap closes near a single point, which was taken as the formation of the Weyl state [33]. However, while Rh is in the same family as Ir, it is much more commonly found in the Rh^{3+}oxidation state rather than the Rh^{4+} needed to isovalently substitute for Ir^{4+}. Therefore, instead of reducing the average SOI in the conduction band, it is likely that the primary effect observed in optical conductivity is due to hole doping. One would then expect that the substitution of divalent Ca^{2+} for Nd^{3+} should yield similar effects, and in fact asI have shown in Chapter 5, our preliminary measurements of the temperature dependent resistivity of $Nd_{1.9}Ca_{0.1}Ir_2O_7$ follows quite closely with that observed for similar levels of Rh doping shown in Ref [33].

Based on these results we should also be able to place some constraints on the parameter space used to calculate potential phase diagrams in this system. One of the most directly comparable of these is the U - t phase diagram calculated by Witczak-Kremp and Kim [13] shown below in Figure 6.2. Here they show that as either U or the direct hopping amplitude is varied the system may realize normal insulating and metallic state as well as the Weyl semi-metal and topological insulating phases. Two arrows have been added onto their diagram to indicate example paths for the evolution of the ground state as the A-site radius is increased based on our results; that is, the base of each arrow represents the Yb-227, while the tip of the arrow Pr-227. Based on our results, we know that the insulating compounds are solidly in the AIAO insulating region, while previous studies have identified Pr-227 as being in the metallic region. In the previous section, it was argued that the action of the increased A-site is to vary the trigonal distortions which should vary the hopping parameters; this should amount to a horizontal cut across the phase diagram, as illustrated by the red arrow. On the other hand, depending the mixing of the j = 3/2 and 1/2 levels, the correlation energy may also be affected by these distortions, and therefore we cannot rule out the system following a more vertical path as illustrated by the blue arrow in the figure.

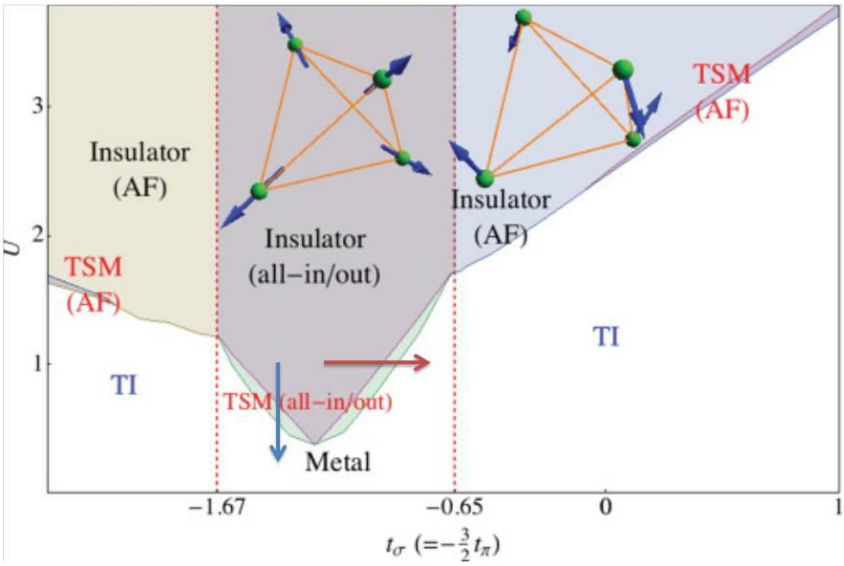

Figure 6.2 U-t phase diagram calculated by Kremp for the pyrochlore series

Our supposition that the AIAO configuration is maintained across the series is consistent with both paths taken here. Neutron scattering and estimated local field calculations have ruled out the presence of either of the other two AFM configurations shown in Figure 6.2. Taking either possible route, our results also do not rule out the presence of the Weyl (or topological semi-metal, TSM) state for an intermediate compound such as Nd-227.

This behavior is consistent with that proposed by Chen and Hermele in which they examined the influence of the *f-d* exchange interaction on the $A_2Ir_2O_7$ system. They showed that both AIAO and 2I2O configurations are possible on either sublattice, depending on the strength and anisotropy of the exchange parameters [34]. Our results

show that the range of parameters must be such that the Ir sublattice is AIAO, with the Nd sublattice likely favoring a 2I2O type of ground state if this exchange interaction is to be the dominate type. However, based on these calculations one expects these would be significantly altered through appropriate tuning the conduction electron density. On the basis of comparisons between our measurements and those on more insulating samples of Nd-227 it appears that the scale and size of the correlations do not change over many orders of conduction electron density. One possibility is that the carriers sampled by the Hall effect are not those primarily participating in the exchange interactions as a result of a complex band structure with multiple hole and electron pockets. Another possibility is that the *f-f* interaction is not mediated by conduction electrons, but rather more local exchange interactions which are not as affected by carrier concentrations the conduction electron do not mediate the exchange interactions. Additional studies of Ca-doping near the cross over from electron to hole-like carriers would be useful in understanding the details of the interaction mechanism.

Chapter 6 References

[1] S. Zhao, J. M. Mackie,D. E. MacLaughlin,O. O. Bernal,J. J. Ishikawa,Y. Ohta,and S. Nakatsuji, Phys. Rev. B **83**, 180402(R) (2011).

[2] K. Matsuhira, M. Wakeshima, Y. Hinatsu, and S. Takagi, J. Phys. Soc. Jpn. 80 094701 (2011).

[3] X. Wan, A. M. Turner,A. Vishwanath,and S. Y. Savrasov, Phys. Rev. B **83**, 205101 (2011).

[4] H. Sagayama, D. Uematsu, T. Arima, K. Sugimoto, J. J. Ishikawa, E. O'Farrell, and S. Nakatsuji. Phys. Rev. B **87** 100403(R) (2013).

[5] S. M. Disseler, Chetan Dhital, A. Amato, S. R. Giblin, Clarina de la Cruz, Stephen D. Wilson, and M. J. Graf, Phys. Rev. B **86**, 014428 (2012).

[6] S. M. Disseler, Chetan Dhital, T. C. Hogan, A. Amato, S. R. Giblin, Clarina de la Cruz, A. Daoud-Aladine, Stephen D. Wilson, and M. J. Graf, Phys. Rev. B **85**, 174441 (2012).

[7] D. E. MacLaughlin, Y. Ohta, Y. Machida, S. Nakatsuji, G. M. Luke, K. Ishida, R. H. Heffner, Lei Shu, and O. O. Bernal, Physica B **404**, 667 (2008).

[8] S. M. Disseler, S. R. Giblin, Chetan Dhital, K. C. Lukas, Stephen D. Wilson, and M. J. Graf. Phys. Rev. B **87**, 060403(R) (2013).

[9] P. J Baker, J. S. Moeller, F. L. Prattrm W. Hayes, S. J. Blundell, T. Lancaster, T. F. Qi, G. Cao. arXiv 1302.6905 (2013).

[10] T F Qi1, O B Korneta, Xiangang Wan, L E DeLong, P Schlottmann and G Cao, J. Phys. Cond. Matter **24** 345601 (2012).

[11] T. Moriya, Progr. Theoret. Phys. **16**, 23 (1956).

[12] Bohm-Jung Yang and Yong Baek Kim. Phys. Rev. B **82** 085111 (2010)

[13] William Witczak-Krempa and Yong Baek Kim. Phys. Rev. B **85** 045124 (2012)

[14] Liviu Hozoi, H. Gretarsson, J. P. Clancy, B.-G. Jeon, B. Lee, K. H. Kim, V. Yushankhai, Peter Fulde, Young-June Kim, and Jeroen van den Brink, ArXiv 1212.4009 (2012).

[15] D. Yanagishima and Y. Maeno, J. Phys. Soc. Jpn. **70**, 2880 (2001).

[16] M. Sakata, T. Kagayama, K. Shimizu, K. Matsuhira, S. Takagi, M. Wakeshima, and Y. Hinatsu, Phys. Rev. B **83**, 041102(R) (2011).

[17] F. F. Tafti, J. J. Ishikawa, A. McCollam, S. Nakatsuji, and S. R. Julian. Phys. Rev. B **85** 205104 (2012).

[18] John Nichols, Noah Bray-Ali, Gang Cao and Kwok-Wai Ng. ArXiv 1302.5431 (2013)

[19] Y.Okada, D. Walkup, H. Lin, C. Dhital, Tay-Rong Chang, S. Khadka, W. Zhou, Horng-Tay Jeng, A. B., Z. Wang, S. Wilson, V. Madhavan, ArXiv 1303.6027 (2013).

[20] D. Haskel, G. Fabbris, Mikhail Zhernenkov, P. P. Kong, C. Q. Jin, G. Cao, and M. van Veenendaal. Phys. Rev. Lett. **109** 027204 (2012).

[21] P. Quémerais, P. McClarty, and R. Moessner. Phys. Rev. Lett. **109**, 127601 (2012)

[22] J.A. Rodriguez, A. Yaouanc, B. Barbara, E. Pomjakushina, P. Quémerais, Z. Salman. arXiv:1303.3401 (2013).

[23] S. R. Dunsiger, Ph.D. thesis, University of British Columbia, 2000.

[24] Oren Ofer, Amit Keren, Jason S. Gardner, Yang Ren, and W. A. MacFarlane. Phys. Rev B **82** 092403 (2010)

[25] J. E. Greedan, Delphine Gout, A. D. Lozano-Gorrin, Shahab Derahkshan, Th. Proffen,
H.-J. Kim, E. Božin, and S. J. L. Billinge. Phys. Rev. B **79** 014427 (2009).

[26] T. E. Sanders and J. T. Chalker. Phys. Rev. Lett. **98** 157201 (2007)

[27] L. D. Landau and E. M. Lifhitz. *Statistical Phyiscs I* (Butterworth-Heinemann 1980).

[28] M. Takahashi, Phys. Rev. B 40, 2494 (1989)

[29] D. J. Yoshioka, Phys. Soc. Jpn. 58, 3733 (1989).

[30] A. Yaouanc, P. Dalmas de Réotier, Y. Chapuis, C. Marin, G. Lapertot, A. Cervellino, and A. Amato. Phys. Rev. B **77** 092403 (2008).

[31] W. Higemoto, A. Koda, G. Maruta, K. Nishiyama, H. Nakamura, S. Giri, M. Shiga. Jour. Phys. Soc. Jap. **10** 2361 (2002).

[32] N. P. Raju, M. dion, M J. P. Gingras, T. E. Mason, J. E. Greedan. Phys. Rev. B **59** 14489 (1998).

[33] K. Ueda, J. Fujioka, Y. Takahashi, T. Suzuki, S. Ishiwata, Y. Taguchi, and Y. Tokura. Phys. Rev. Lett. **109**, 136402 (2012).

[34] Gang Chen and Michael Hermele. Phys. Rev. B **86** 235129 (2012)

Chapter 7: Conclusions and Future Work

7.1 Conclusions

The results of Chapters 4 through 6 represent a substantial gain in our knowledge of the magnetism and electronic properties of the pyrochlore iridate series. This work has shown unequivocally that long-range magnetic order exists on the Ir sublattice in all insulating and weakly-metallic members of this family regardless of the magnetic properties of the *A*-sublattice. Because of this work, we now know that the magnetic structure of this Ir moments is uniform across the series with the all-in/all-out configuration a development recently confirmed with resonant x-ray measurements. Our investigations of $Nd_2Ir_2O_7$ have shown for the first time that long-range magnetic order exists in a metallic pyrochlore iridate, and assert this compound is a cross-over in the series between the Mott-like insulators and the metallic chiral $Pr_2Ir_2O_7$.

Although only briefly discussed in Chapter 3, a major accomplishment of this project was the fabrication of high quality polycrystalline samples of these compounds which had formerly only been produced a handful of groups around the world. Indeed, the entirety of this work would not have been possible if it were not for the dedication and hard work of those in Stephen Wilson's lab to produce and characterize these samples of exceptional quality. Their work with neutron scattering discussed in Chapters 4 and 5 allowed for not only improved refinement of the crystal structure, specifically the

location of the oxygen ions, but also conclusively proved no structural distortions nor magnetic order at a $Q \neq 0$ wavevector occur in any of these materials.

Unlike other pyrochlore series, such as the titanates, which can be studied in beautiful detail via neutron scattering, the neutron absorbing properties of Ir make this approach nearly impossible. Therefore, the primary contribution of this thesis to the greater community is its role as a survey of the magnetism across the rare-earth series using μSR as sensitive local probe. Indeed, the results contained in this work provide the first conclusive evidence that long-range magnetic order is ubiquitous in all insulating and semi-metallic members of this series. Furthermore, through a detailed analysis of his μSR data in conjunction magnetization and neutron scattering, I have shown conclusively for the first time that the Ir sublattice has the AIAO configuration, a result only previously inferred from other measurements. Our measurements of $Yb_2Ir_2O_7$ and $Nd_2Ir_2O_7$ also represent the first study in this series to examine compounds with a magnetic *A*-sites lattice using local probes; as discussed in Chapter 6 these have already indicated that the *A*-sublattice behaves nearly independently of the Ir-moments and may in fact be host to other interesting magnetic phenomena.

Another contribution of this work is the advancement in our knowledge of one of the most fascinating compound of the series, $Nd_2Ir_2O_7$. While this material is interesting as a potential host of the Weyl state, here I have focused more on its role as an intermediary between the insulating and ordered compounds and the the so-called chiral metallic ground state found in $Pr_2Ir_2O_7$. What was found was that at low temperatures the Ir-sublattice orders in the same all-in/all-out configuration as the insulators, however the Nd-sublattice is in the degenerate spin-ice state similar to $Pr_2Ir_2O_7$ on the basis of our

measurements of the magnetization, Hall Effect and magnetocaloric effect. By introducing a small amount of additional hole-like carriers into this system via Ca-substitution the magnetic order on both sublattice has been removed, however without additional measurements it is unclear if this is due to simply additional screening of the Nd moments or increased interactions which drive the system into a state more akin to that observed in $Pr_2Ir_2O_7$. These results represent a new way of probing this family of materials and although are only in the very initial stages, hold tremendous promise as a way of learning more about the evolution of the fundamental interactions which drive the fascinating phenomena in this series.

7.2 Future Work

As pointed out many times, there is a tremendous amount of work to be done in this system, and many different avenues which should be the focus of future projects. In general, these include a thorough investigation of the intermediate magnetic state which apparently lacks long-range order, the role of microstructure, surfaces, and defects on the observed magnetic properties, and lastly to examine the magnetic order or lack there of in the *A*-sublattices of these compounds. I will now outline some of these, and the current progress towards them, if any.

7.2.1 Single Crystals

One of the most immediate needs for a more precise study of the evolution of the magnetism is sufficient size single crystals of many of the compounds studied in this

work to perform transport, magnetization, muon spin measurements and maybe most importantly neutron scattering studies. These single crystals are also necessary to test out key theoretical predictions such as the appearance of a large quantum Hall effect which should be observed in the Weyl state, for example. Current progress in this area by Stephen Wilson's group has produced batches of single crystals of Nd-227 with average dimension of 100 micrometers per side with an octahedral shape that must polished flat in order to perform many useful measurements. Current attempts at measuring transport properties of these samples using Focus Ion beam to deposit leads has proven to be difficult, and measurements of a collection of aligned crystals resulted in a paramagnetic signal was hard to isolate from the background due to the small net sample weight. A few of the largest crystals were taken to the Advanced Light Source at Argonne National Lab and studied via resonant x-ray scattering, however no signs of magnetism were observed to 3 K, the current limit at those facilities. Improvements to the current flux-growth process an possible use of optical float-zone furnaces are necessary to improve the dimensions of these materials in order to allow more definite measurements in the future.

7.2.2 Low Temperature State of Yb-227

Detailed in Chapter 4, the low temperature state of $Yb_2Ir_2O_7$ presents a new challenge to this field, and represents a potentially new way of approaching the quatum spin ice states propsed in $Yb_2Ti_2O_7$. Even if single crystals cannot be fabricated, future studies of the magnetization and specific heat below the peak observed in the spontaneous precession frequency in μSR are necessary to determine the ground sate of

the Yb-sublattice, specifically to look for potentially interesting new forms quantum dynamics or magnetism.

7.2.3 Characterization of Sm-227, etc.

It will be important to further characterize other samples in this series using the techniques presented in this work to determine which structural changes actually drive the transition from insulating to metallic ground state. Particularly useful will be the samples such as Sm-227 which between Eu-227 and Nd-227 near the metal-insulator boundary. It would also be of considerable interest to perform these measurements on samples synthesized via the slightly different routes used by other groups as a way of determining the role of microstructrue, surfaces, and inherent differences in the type and number of local defects. Together, this should provide for a detailed study of the evolution of the size and configuration of the Ir moment, as well as look for new possibly interesting states on the *A*-sublattice.

7.2.4 Doping Studies

Lastly, the work presented in Chapter 5 represents the very beginning of an important study which examines the effects of charge-doping in the particularly sensitive $Nd_2Ir_2O_7$. In addition to continued characterization of current samples through magnetization and susceptibility, samples of many more concentrations should be fabricated which will allow for the study of the detailed *f-d* interactions and the role of

electron correlations, as well as a greater knowledge of the complex band structure in these materials.

Appendix A1: MatLab Code

A1.1 Electrostatic Potential Calculation Code

```
%% This code will calculate the electrostatic potential over a unit cell using Ewald's
method as described in Chapter 4. Several subroutines are used which can be found in the
sections after this; these are used to define the positions of the various ions in the unit
cell.

clear all; close all; clc;
tic

% Set up Grid
LC = 10.1699;   %lattice constant, angstroms
g= .2;          %grid spacing, angstroms
N = nearest(LC/g)+1;

Cells = 1; x = 0.334;

Ir_lattice =LC* A227_16c_MultiCell_SiteCalc(Cells);
A_lattice = LC*A227_16d_MultiCell_SiteCalc(Cells);
O1_lattice = LC*A227_48f_MultiCell_SiteCalc(Cells,x);
O2_lattice = LC*A227_8b_MultiCell_SiteCalc(Cells);


%Set Ion Properties, Q: ion charge, R = Ion radius (approximate, needed for removing
singularities,

Q_Ir = 4; Q_A = 3;  Q_O = -2;

R_Ir = 2;  R_A = 2;  R_O = 4;

Ir_lattice(:,4) = Q_Ir;
A_lattice(:,4) = Q_A;
O1_lattice(:,4) = Q_O;
O2_lattice(:,4) = Q_O;

Ir_lattice(:,5) = R_Ir;
A_lattice(:,5) = R_A;
O1_lattice(:,5) = R_O;
O2_lattice(:,5) = R_O;
```

```
% Complete working lattice with all of the positions, charges and radii:
Atoms = [Ir_lattice; A_lattice; O1_lattice; O2_lattice];

% The following block will construct an array of reciprocal lattice vectors needed for
Ewalds method. This will create up to N^3 vectors.

        B = 2*pi*(1/LC*sqrt(3))*[-1,1,1;1,-1,1;1,1,-1];
        detB = det(B);

        NCells = 4;
        u = [0,0,0];

        ncount=1;
        for i1 = 1:NCells
          for j1 = 1:NCells
            for k1 = 1:NCells

              u(ncount,:) = [i1-(NCells-1)/2,j1-(NCells-1)/2,k1-(NCells-1)/2];
              ncount = ncount+1;

            end
          end
        end


%The next block will initialize other parameters needed for Ewald method, including the
added hard-core potential parameter R0 and smoothing factor epsilon as described in
Chapter 4. The electric potential will be stored in the three-dimensional array V.

epsilon = 10; %Gaussian width
R0 = 2; %Hard-core repulsion parameter


%Initialize potential matrix and constants
        V = zeros(N,N,N);

        eps2 = epsilon^2;
        c1 = 4*(pi/detB);
        c2 = pi/(eps2*detB);
        c5 = 0.25*eps2;

%The following block will compute the potential, it is broken up into 2 parts, the real
space and reciprocal space parts. Additional comments are added throughout to clarify
the purpose of each step
```

```
for i2 = 1:N
   for j2 = 1:N
      for k2 = 1:N

        Vpoint = 0;

         %Vpoint: scalar representing potential at the point (Vi2,j2,k2) so that the entire
        V-matrix doesn't have to be moved in every step.

         r = [g*(i2-1),g*(j2-1),g*(k2-1)];   %real space coordinate for the point [i2, j2, k2]

        for l = 1:length(Atoms(:,5))
          dr = r - Atoms(l,1:3);   %vector from the lth atom from the coordinate i2,j2,k2

                normdr = norm(dr);

        % calculate the direct space part. This will add up contributions %from all of the
        atoms in the 'Atoms' array including the hard-core repulsion


        Vpoint = Vpoint + Atoms(l,4)*(1-erf(epsilon*normdr))/normdr + (1/LC)*exp(-
        normdr/R0);

        % calculate reciprocal space part. Note that only the atoms within a single unit
        cell are needed to compute this part, so we will save time and make sure the sum
        only runs over those.

         if norm(Atoms(l,1:3)) < LC

                for m = 1:length(u(:,1)) %sum over reciprocal lattice vectors
                     if norm(u) == 0      %don't include the q=0 term
                     else
                         c3 = (norm(B*u(m,:)'))^2;

                Vpoint = Vpoint + c1/c3*Atoms(l,4)*exp(-1i*dr*B*u(m,:)')*exp(-c5*c3);
                     end
                 end

        end

end
                V(i2,j2,k2) = Vpoint; %Add the point to the array V
end
```

```
 end
save('Vpartial.mat', 'V','i2'); after each step in Z save the entire matrix in case program crashes.

end

V = real(V) - c2;

save('V_final');
```

A1.2 Example Subprogram defining atom locations

A227_16c_MultiCell_SiteCalc(N)

%This program will calculate the vector loacations for Ir(16c) sites over several unit cells, with distances normalized to a unit cell of size unity. All locations are based on the 16c sites for Fd3m spacegroup, taken from: International Tables for Crystallography (2006). Vol. A, Space group 227, pp. 696. Note that the locations of any other ions can be found using this routine by replacing the sites in the array *R0* with the correct locations for the Wycoff site of interest.

```
function [out1] = A227_16c_MultiCell_SiteCalc(N)

R = zeros(16,3);

%16c-sites. REPLACE THIS TO GET OTHER ION LOCATIONS
R0 = [0 0 0; .75 .25 .5; .25 .5 .75; .5 .75 .25];

% translation vectors for 227 space group to get rest of the sites within a single unit cell
t = [ 0 0 0; 0 .5 .5; .5 0 .5; .5 .5 0];

for i = 1:1:4
   for j = 1:1:length(t(:,1))

      R(4*(i-1)+j,:) = R0(i,:)+t(j,:);
   end
end
R = mod(R,1);
n1 = length(R(:,1));
R1 = R;

%% The following block will find the location of the ions over a block of unit cells with
2N +1 unit cells per side

if N > 0;
n_count =1;
for i = -N:1:N
   for j= -N:1:N
      for k = -N:1:N
         for m = 1:n1
         R(n_count,:) = R1(m,:) + [i,j,k];
         n_count = n_count+1;
         end
```

```
        end
    end
end
end
n = length(R(:,1));
out1 = R;
end
```

A1.3 Unit Cell Dipole Calculation

```
%The goal of this program is to calculate the magnetic field everywhere in the unit cell given a configuration of Ir moments. Example configurations are shown here, however any one which meets the correct formatting may be used.

%Define Constants
mu_0 = 4*pi*10^-7;
gamma_mu = 135.5;
a = 10.1667*(10^-10);

Ir_moment = 1;

Ngrid = 100;
Bgrid = zeros(Ngrid+1, Ngrid+1, Ngrid+1);


% This section will generate an array with the location and the local orientation of all of the Ir moments in a single unit cell.

R = zeros(16,6);

%16c-sites
R0 = [0 0 0; .75 .25 .5; .25 .5 .75; .5 .75 .25];

%Possible moment configurations
m2I2O = 1/sqrt(3)*[1 1 1; 1 1 -1; -1 1 -1; -1 1 1];
mAIAO = 1/sqrt(3)*[1 1 1; -1 -1 1; -1 1 -1; 1 -1 -1];
mFM = 1/sqrt(3)*[1 1 1;1 1 1;1 1 1;1 1 1 ];

%  translation vectors
t = [ 0 0 0; 0 .5 .5; .5 0 .5; .5 .5 0];
t = [t zeros(4,3)];

R0 = [R0 mFM];


for i = 1:1:4
   for j = 1:1:length(t(:,1))

      R(4*(i-1)+j,:) = R0(i,:)+t(j,:);
   end
end

Rcell = mod(R(:,1:3),1);
```

```
n1 = length(R(:,1));
R1 = [Rcell, R(:, 4:6)];

% The user can decide how many unit cells worth of moments should be included in the calculation. This will form 2N + 1 Cells per side, such that the magnetic field will be calculated only for the center unit cell.

N = 2;
n_count =1;
for i = -N:1:N
   for j= -N:1:N
      for k = -N:1:N
         for m = 1:n1
         R(n_count,:) = R1(m,:) + [i j k 0 0 0];
         n_count = n_count+1;
         end
      end
   end
end

n = length(R(:,1));



%The following block will calculate the magnetic field due to the sum of all of the above dipole moments over a grid with Ngrid number of points.

for igrid = 0:Ngrid-1
 for jgrid = 0:Ngrid-1
 for kgrid = 0:Ngrid-1

       R_mu = 1/Ngrid*[igrid, jgrid, kgrid];


B = zeros(3,1);
for m = 1:n

   D = zeros(3);

   r = a*(R_mu-R(m,1:3));
      for i =1:3
         for j =1:3

            D(i,j) = mu_0/(4*pi)*(1/norm(r)^3)*(3*r(i)*r(j)/(norm(r))^2 - KronD(i,j));
```

```
        end
      end
   B = B + Ir_moment*D*R(m,4:6)'*(9.274E-24);

   save('Bgrdpartial','B','igrid');
end

      B_Ir = B; % magnitude, in tesla
      Bgrid(igrid+1,jgrid+1,kgrid+1) = norm(B_Ir);

    end
 end
end

save('field_simulation.m','Bgrid')
```

A1.4 Bayes Theorem Analysis

```
%Load the simulation of the magnetic field at a collection of muon test sites. This should contain a one dimensional array called 'B_mu'

Load field_simulation.mat;

%Define an array of magnetic moments to simulate the effective field. dMu will be the width of each bin in the final probability histogram.

dMu = 0.01;
Mu = .01:dMu:5;
n = length(Mu);

Bmatrix = zeros(length(B_mu),n);

%Next section will multiply the normalized magnetic field given by 'B_mu' by the size of the moments to be used, creating an 2D array called B_matrix. Each column reprsentss the magnetic fields calculated for moment given by one of thea vlues in the array Mu.

for i = 1:n

Bmatrix(:,i) = B_mu'*Mu(i);

end

%The next section takes the magnetic fields calculated above, and turns each column into a histrogram using the details supplied below. Each column is then normalized to form the probability distribution P(B|m) where m is the size of the moment given by the column number according to the array Mu.

Bbin = 0.001;
B = 0:xbin:4;
Blength = length(x);

HistMatrix = zeros(xlength, n+1);
HistMatrix(:,1) = B;

for i = 1:n

   HistMatrix(:,i+1) = histc(Bmatrix(:,i),B)/(sum(histc(Bmatrix(:,i),B)));

end
```

%This last section is the actual Bayes theorem part of the program. The goal was to determine *P(m|B)* or the probability of finding a moment of size *m* given a field of size *B*. The user must supply this value, called *Bmeasured* below, which is extracted from experiments. The final result is the normalized probability distribution *g*(Mu) which is then plotted as a function of the moment *Mu* in the last line.

```
Bmeasured = .0660;

ind = find(HistMatrix(:,1) == Bmeasured);

f = HistMatrix(ind,2:n+1)./Mu;
g = (f)/sum(histc(f,Mu)*dMu);

plot(Mu,g)
```

A2: Selected Publications

Publication List

Magnetization and Hall effect studies on the pyrochlore iridate Nd2Ir2O7. S. M. Disseler, S. R. Giblin, Chetan Dhital, K. C. Lukas, Stephen D. Wilson, and M.J. Graf. Phys. Rev. B **87**, 060403(R) (2013).

Superconductivity of Bi Confined in an Opal Host. R. C. Johnson, M. D. Nieskoski, S. M. Disseler, T.E. Huber, M. J. Graf, J. Low Temp Phys **170** 205 (2013)

Magnetic Order in the Pyrochlore Iridates A2Ir2O7 (A = Y, Yb). S. M. Disseler, Chetan Dhital, A. Amato, S. R. Giblin, Clarina de la Cruz, Stephen D. Wilson, M. J. Graf. Phys. Rev. B **86**, 014428 (2012).

Spin ordering and electronic texture in the bilayer iridate Sr3Ir2O7. Chetan Dhital, Sovit Khadka, Z. Yamani, Clarina de la Cruz, T. C. Hogan, S. M. Disseler, Mani Pokharel, K. C. Lukas, Wei Tian, C. P. Opeil, Ziqiang Wang, Stephen D. Wilson. Phys. Rev. B **86**, 100401 (2012).

Magnetic order and the electronic ground state in the pyrochlore iridate Nd2Ir2O7. S. M. Disseler, Chetan Dhital, T. C. Hogan, A. Amato, S. R. Giblin, Clarina de la Cruz, A. Daoud-Aladine, Stephen D. Wilson, M. J. Graf. Phys. Rev. B **85**, 174441 (2012).

Yb4LiGe4 – A Yb mixed valent Zintl phase with strong electronic correlations. S. C. Peter; S. M. Disseler; J. Svensson; P. Carretta; M. J. Graf. Jol of Alloys and Comp 515 (2011).

Competing interactions and magnetic frustration in Yb4LiGe4. S. M. Disseler, J. N. Svensson, S. C. Peter, C. P. Byers, C. Baines, A. Amato, S. R. Giblin, P. Carretta, and M. J. Graf, Phys. Rev. B 84, 174429 (2011).